DEVELOPMENT OF MICROFLUIDIC PACKAGES ON MULTILAYER ORGANIC SUBSTRATE FOR COOLING AND TUNING RF CIRCUITS

A Ph.D. Dissertation
Presented to
The Academic Faculty

by

Outmane Lemtiri Chlieh

In Partial Fulfillment
of the Requirements for the Degree
Doctor of Philosophy
in
Electrical and Computer Engineering

School of Electrical and Computer Engineering
Georgia Institute of Technology
December 2015

DEVELOPMENT OF MICROFLUIDIC PACKAGES ON MULTILAYER ORGANIC SUBSTRATE FOR COOLING AND TUNING RF CIRCUITS

Approved by:

Dr. John Papapolymerou, Advisor
Professor, School of ECE
Georgia Institute of Technology

Dr. Hua Wang
Assistant Professor, School of ECE
Georgia Institute of Technology

Dr. John Cressler
Professor, School of ECE
Georgia Institute of Technology

Dr. Christos Alexopoulos
Professor, School of ISyE
Georgia Institute of Technology

Dr. Steve Kenney
Professor, School of ECE
Georgia Institute of Technology

Date Approved: October 28th, 2015

“A person who never made a

mistake never tried anything new.”

-Albert Einstein

“Truth is ever to be found in simplicity,

and not in the multiplicity and confusion of things.”

-Isaac Newton

To my wife (Soundouss), brother (Salah), sister (Basma) and parents (Fatima and Jaouad) for their unconditional love and support.

ACKNOWLEDGMENTS

First of all, I would like to thank God Almighty for opening the doors for me to achieve this great accomplishment. I thank God for answering all my prayers every time I needed him especially in moments of doubt and stress.

My sincere and deepest thanks go to my advisor Dr. John Papapolymerou (or Dr. P as many like to call him) who offered me a GRA position in 2011 to work with his research group "Microwave Circuit Technology Group" (MiRCTECH). This position empowered me with invaluable experience throughout the few years I spent with the group with all the hands-on experiments I did, the time I spent in the cleanroom for fabrication, the design and simulation tools I used, and the international conferences I attended… I always said that I liked Dr. P's macro-management style, where his students get the chance to work on the research tasks assigned with a wide margin of freedom, creativity and new emerging ideas. That said, his inputs and remarks regarding the progress of the projects have always been incisive and helpful to provide solutions to some of the problems faced.

I cannot miss this opportunity to express my deepest condolences to Dr. Bob Rice's family from the Georgia Tech Research Institute (GTRI) who passed away a few months only after I joined Dr. P's group to work on the collaborative project between MiRCTECH and GTRI. I am saddened even more because I just knew about this recently, I thought at the time that the project had stopped for other reasons. Dr. Bob Rice was my first contact in the US, I remember calling him from the office of Bertrand Boussert, the recruitment manager head of academic programs in Georgia Tech Lorraine in France, where we were talking about the GRA position and the research topic I would be working on. It was a great pleasure working with him for the first few months, may his soul rest in peace. I will not forget to thank Bertrand for picking me

up from the entire GTL School and convincing me to take this GRA opportunity and that I was the best fit to the position among all other candidates. By this occasion, I would like to send my sincere thanks to all my professors from ENSEEIHT (Ecole Nationale Supérieure d'Electrotechnique, d'Electronique, d'Informatique, d'Hydraulique et des Télécommunications) in Toulouse France who contributed to my solid education in electronics, I would like to cite Prof. Danielle Andreu for her support regarding my admission application to Georgia Tech and Prof. Hervé Aubert for his outstanding teaching skills.

I would like also to thank all the other members of my PhD defense committee Dr. John Cressler, Dr. Steve Kenney, Dr. Hua Wang and Dr. Christos Alexopoulos for accepting to serve in my defense committee and for providing their feedback and guidance.

I would like to extend my thanks to the sponsors who provided funding throughout different phases of my PhD, namely: GTRI for funding the first year of my research, I²R Nanowave Inc. for sponsoring some of the collaborative projects, and finally the National Science Foundation (NSF) for funding the main part of my research. Special thanks go to Edward Gebara, the director of engineering at I²R Nanowave, with whom I collaborated in few projects and with whom I had some intense and stimulating religious, political and technical discussions. My sincere thanks go to a great friend Dr. Carlos Donado Morcillo, ex-MiRCTECH PhD student and ex-I²R Nanowave employee who had been very helpful when I first joined the research group. He was very supportive and helped me get familiar with the design tools and the different pieces of equipment in the lab. I admire his meticulous personality and his great attention to details while addressing various technical problems. We had great

discussions about virtually everything: soccer, politics, social issues, research and many other topics. Thanks for the great moments we shared together.

It was a great honor working with everyone in MiRCTECH, so I would like to thank them for all the time we spent together. Previous members include Dr. Arnaud Amadjikpe, Dr. Aida Vera, Dr. Benjamin Lacroix, Dr. Carlos Donado, Dr. Chad Patterson, Gaetan Dufour, George Alexopoulos, Sensen Li and Dr. Wasif Khan. Dr. Benjamin Lacroix was the first person to welcome me the first day I stepped into the Technology Square Research Building (TSRB), as a senior member, he was a great mentor and provided help and technical support to everyone in the group whenever needed. I would like to thank George Alexopoulos and Sensen Li for being such nice and sociable friends, we spent a great time inside and outside the lab. How can I not mention Dr. Wasif Khan? Wasif was a great friend, an excellent researcher and a reliable person. I thank him for always being there for me for assistance, stimulating new ideas, helping with fabrication, training me on the different tools in the cleanroom and doing the prayers together whenever possible. I would also like to thank the current MiRCTECH members: Christopher Barisich, Fan Cai and Spyridon Pavlidis and wish them all the best for the rest of their research. I would like to thank Christopher Barisich on how we collaborated together and helped each other at various stages of our PhDs, on how we trained each other on the old and new load pull system, and on the endless discussions that we sometimes have. Special thanks go to Spyridon Pavlidis, whom I called “my brother” in my proposal exam presentation, I wish to tell him that I really mean that. We started our PhD program almost at the same time, we assembled the load pull system in our second year, we gave on one occasion a lecture to Dr.P’s undergraduate class, we took courses together in the Sheller Business School to get the certificate of management of technology, we went to many conferences together, we

continuously support and help each other, and we always talk and laugh about everything. I wish also to thank him for helping me get properly trained on the cleanroom equipment and answering my late phone calls when I had doubts using a particular equipment. Thank you and I wish we could stay very good friends for all the time to come.

I would like also to thank the other research groups with which we usually collaborate and work together on common projects mainly the SiGe group led by Dr. John Cressler and the GEMS group led by Dr. Hua Wang. My thanks go to the following students I was in contact with from both groups: Chris Coen, Jong Seok Park, Peter Song, Saeed Zeinolabedinzadeh, Song Hu and Taiyun Chi. During my four years of research, many research engineers and post-docs were part of the group, so my thanks go to Dr. Debasis Dawn, Dr. Cagri Ulusoy and Dr. Moon-Kyu for providing technical assistance for the students. I will not miss this opportunity to thank the administrative people in TSRB who helped us process our orders on time and guided us through various administrative paperwork: Carolyn Daley-Foster, Daphne Bronner, Lisa Salter, Maria Matheson, Scott Sladek and Toya Jordan. The cleanroom staff is also to be acknowledged for the effort they put in to enable us to do our work on time. I specifically want to thank Chris White for training me on the thermal press and Richard Shafer for being so nice patient for the various laser lab trainings. Thanks also go to Dr. Brent Wagner and Dr. Wusheng Tong from GTRI for the infrared thermal camera training.

At the end, I would like to thank all my Moroccan friends Taha Hayat, Hamada Jouahri, Khalifa Afourer, Driss Ghayouti, Soufiane Halily, Youssef Igoudyane, Amine Bouhzam, Ahmed Sefiani, Ali Benchekroune, Youssef Chahibi, Souhail Sadik, Omar Fergani and all the international friends that I met in Atlanta Shafi & Adria Motiwalla,

Daniel & Lena Ellingburg, Roula Harfoush, Sanchit Mittal, Kanika Sharma, Kyel Ok, Jaikp Mallory and Kareem Bedri.

All my gratitude goes to my parents Fatima Remmal and Jaouad Lemtiri Chlieh who have been supportive all the way and without whom I would have never have dreamt of achieving anything special in my life. All the sacrifices they did for me for my education and upbringing made a better person and opened so many doors for me. Also, I wish to tell my brother Salah and sister Basma that I love them so much (and their two little babies Lidya and Salma) and thank them for their continuous love and support. Last but not least, I would like to thank my in-laws and my beloved wife Soundouss Ejjiyar who, through her encouragement, her unconditional love and her full support, made my PhD journey much easier. Since we got married at the end of 2012, I became more productive and organized. We have been lucky to get chosen in the green card lottery in 2013, and despite all the stress and anxiety of the whole process, we have been able to get our green cards recently, so I thank God for this tremendous opportunity that He blessed us with. Thank you Soundouss for all the moments of joy and stress, ups and downs that we have been through together and for all the days that are ahead of us.

All these people I mentioned above have shaped in a way or another who I am as a person and contributed to this great achievement in my life. I would like to express my gratitude and appreciation to all of them and wish them all the best in their personal lives and professional careers.

TABLE OF CONTENTS

LIST OF TABLES

LIST OF FIGURES

NOMENCLATURE FOR CHAPTER 4

A	channel area illustrated in Fig. 4.4, m^2
A'	LCP area, m^2
A_s	source area illustrated in Fig. 4.3, m^2
$A_p = A$	plate area illustrated in Fig. 4.3, m^2
a	source radius illustrated in Fig. 4.3, m
b	plate radius illustrated in Fig. 4.3, m
Bi	Biot number
BLT	bond line thickness, m
C_p	fluid specific heat, $J/(kg.K)$
D_h	hydraulic diameter, m
g	standard gravity, = $9.807\ m/s^2$
Gr	Grashof number
h	forced convective heat transfer coefficient, $W/(m^2.K)$
h'	natural convective heat transfer coefficient, $W/(m^2.K)$
k	plate thermal conductivity, $W/(m.K)$
k'	fluid thermal conductivity, $W/(m.K)$
k_{TIM}	thermal grease thermal conductivity, $W/(m.K)$
L	channel length illustrated in Fig. 4.4, m
L_C	surface characteristic length, m
L_h	hydraulic entry length, m
L_t	thermal entry length, m
L_x, L_y	LCP length, width illustrated in Fig. 4.2, m
m	parameter defined in Eq. (4.30)

N	parameter defined in Eq. (4.31)
Nu	Nusselt number
Nu_{fd}	Nusselt number for fully developed flow
$Nu_{x^*\to 0}$	Nusselt number for low dimensionless axial positions
P_s	heat source dissipated power, *W*
P_{max}	heat source maximum dissipated power, *W*
P_{rad}	radiated power, *W*
Pr	Prandtl number
Q	fluid flow rate, m^3/s
R_c	constriction thermal resistance, °*C/W*
R_{ca}	case-to-ambient thermal resistance, °*C/W*
$R_{contact}$	contact thermal resistance, °*C/W*
R_f	external thermal resistance, °*C/W*
R_{fc}	forced convection thermal resistance, °*C/W*
R_{hs}	heat sink thermal resistance, °*C/W*
R_{ja}	junction-to-ambient thermal resistance, °*C/W*
R_{jc}	junction-to-case thermal resistance, °*C/W*
R_m	material thermal resistance, °*C/W*
R_{multi}	multilayer thermal resistance, °*C/W*
R_{nc}	natural convection thermal resistance, °*C/W*
Ra	Rayleigh number
Re	Reynolds number
S_x, S_y	heat source length, width illustrated in Fig. 4.2, *m*
T	temperature, °*C*

T_0	reference temperature, $°C$
T_{amb}	ambient temperature, = *25 °C*
T_C	case temperature, $°C$
T_f	film temperature, $°C$
T_{HS}	heat sink temperature, $°C$
T_J	junction temperature, $°C$
T_s	surface steady-state temperature, $°C$
t	plate thickness illustrated in Fig. 4.3, *m*
t'	channel thickness illustrated in Fig. 4.4, *m*
W	channel width illustrated in Fig. 4.4, *m*
x	axial position, *m*
x^*	dimensionless axial position

Greek Symbols

α	channel width to thickness ratio
β	coefficient of thermal expansion, *1/K*
ϵ	dimensionless contact radius
ε	channel thickness to width ratio, or, emissivity defined in Eq. (4.37)
λ_n	eigenvalue
ν	fluid kinematic viscosity, m^2/s
ρ	fluid density, kg/m^3
σ	Stefan-Boltzmann constant, = *5.670373e-8* $W/(m^2.K^4)$
τ	dimensionless plate thickness
Φ_n	dimensionless parameter defined in Eq. (4.14)

SUMMARY

The objective of this PhD research is to design and implement novel microfluidic radio-frequency (RF) structures on multilayer organic substrates for cooling and tuning purposes. The different designs were implemented to target applications up to C-band (4 GHz – 8 GHz) frequencies. The system-on-package (SoP) solution adopted throughout this work is well adapted for such designs where there is a need to integrate the functionality of different sub-components into a single hybrid fully packaged system. System integration into a single package for RF applications requires the use of RF substrates which offer excellent electrical and mechanical properties, that is why, the characteristics of organic substrates such as liquid crystal polymer (LCP) are highlighted and contrasted to the other "traditional" and commonly-used RF substrates.

The first part of the thesis is dedicated to the study of a specific liquid cooling scheme using integrated microchannels on organics placed beneath different types of heat sources. A 1 W gallium nitride (GaN) die was cooled using this method and an analysis is presented regarding the cases where the coolant (a 50:50 mixture of water and ethylene glycol) is static or dynamic inside the microchannel. The static case being ruled-out from potential efficient solutions, dynamic distilled (DI) water was used to cool high power passive (high power resistors) and active (5 W GaAs die) devices. Thermal modeling of such microchannels is also detailed for various channel thicknesses and heat source sizes for both flow configurations. Moreover, guidelines are given on how to design cooling microchannels for efficient heat removal.

The second part of the thesis deals with microfluidically reconfigurable microstrip RF circuits, mainly bandpass filters and power amplifiers (PAs). The microfluidic tuning technique is based on the change in the effective dielectric constant

that the RF signal “sees” when traveling above two microchannels with different fluids. This technique was used to shift the frequency response of an L-band microstrip bandpass filter by replacing DI water with acetone inside a 60 mil micro-machined cavity. This technique was also used to design reconfigurable matching networks which constitute the main part of the proposed tunable GaN-based PA for S- and C-band applications. In a first effort to exclusively focus on tunability, the GaN die was placed on top of a thick copper carrier to deal with any thermal effects.

After fully characterizing the effects of tuning and cooling separately, the third part of the thesis expands the previous results by combining both cooling and tuning in a single RF design. To prove the concept, cooling and tuning microchannels were integrated into a single package to cool a GaN-based PA and tune its frequency response from 2.4 GHz to 5.8 GHz and vice versa. Analysis and synthesis techniques of microstrip line characteristics on top of a multilayer substrate are also presented along with a step-by-step guideline on how to design microfluidically tunable matching networks using the aforementioned tuning technique.

CHAPTER 1

INTRODUCTION

Wireless communication systems have been steadily improving throughout the past few years in terms of performance, reliability and size thanks to the progress achieved in the microwave technology and in the radio frequency (RF) discipline in general [1]. Because the RF spectrum is very large (3 MHz – 300 GHz), and so are its applications, the spectrum has been split into multiple bands to support different types of applications. The lower end of the spectrum up to 8 GHz is particularly interesting and many RF applications lie within this range. For instance, some of the applications in the L-band (1 GHz – 2 GHz) are the global positioning system (GPS), GSM cellular communications and aircraft surveillance. In the S-band (2 GHz – 4 GHz), applications include wireless local area network (WLAN) technologies like WiFi, Bluetooth and airport surveillance radars. The C-band (4 GHz – 8 GHz) contains frequency ranges that are used for many satellite communications, some WiFi applications and some weather radar systems.

RF microstrip filters/resonators are widely used in the wireless data transmission chain. Reconfigurable microstrip filters are important in multiple band applications because they allow reducing the system complexity. Many tuning techniques for these types of filters have been demonstrated in the past but none involved the use of microfluidics with organic substrates. The tuning concept can also be extended to other RF systems such as RF power amplifiers (PAs) which are essential microwave components that are present in virtually any wireless transmission device. Gallium arsenide (GaAs) have been widely used for making such PAs, however, many applications today, mainly radar detection and satellite communications, require more efficient PAs that can deliver higher power outputs at higher frequencies. This is why

gallium nitride (GaN) PAs are now becoming very popular thanks to their higher breakdown voltage, power density, electron mobility and temperature of operation [2]. The last property is very important, and although GaN is very promising in that regard, adequate heat sinking mechanisms are still required to dissipate the excess heat generated. Several cooling solutions already exist but the use of microfluidics on organic substrates has not yet been explored.

Organic substrates, such as liquid crystal polymer (LCP), have become very attractive for RF packaging because of their lightweight, low cost, low loss and excellent mechanical properties. LCP also offers multilayer integration capability alongside excellent electrical properties which have made it an excellent candidate for system-on-package RF designs [3]. For these various reasons, LCP has been chosen in this work as the preferred substrate for developing microfluidcally reconfigurable RF systems covering the L, S and C bands and for developing a novel microfluidic cooling technique.

The objective of this research is to use microfluidics to: 1) design and develop reconfigurable RF systems on LCP and 2) come up with a novel cooling solution for active and passive heat sources mounted on LCP. To demonstrate the tunability concept, a microfluidically tunable L-band microstrip bandpass filter has been implemented on LCP. Microfluidically tunable GaN-based PAs working in the S and C bands were realized using reconfigurable matching networks implemented on LCP. For the cooling part, active and passive heat sources were mounted on LCP and cooled using distilled (DI) water circulating inside integrated microchannels. An analytical thermal model was proposed and compared to measurements. Tuning and cooling were combined together to cool a fully organic packaged PA while tuning its frequency of operation.

1.1 RF System-on-Package Solution for Microfluidics Integration

Packaging technologies have evolved with time to solve the growing challenges of electronic systems in terms of size miniaturization, multi-functionality, integration and cost reduction. The realization of integrated microchannels for cooling and/or tuning RF systems requires a multilayer packaging solution that can support surface mount components, integrated circuits (ICs), interconnects and metallization lines on the top layer while the channels are micromachined on the bottom layer. The advanced packaging techniques that exist today can mainly be divided into three categories: system-on-chip (SoC), system-in-package (SiP) and system-on-package (SoP).

Progress made in SoC technology for highly dense ICs has been mainly driven by Moore's law that predicts the doubling of transistors density approximately every two years. The main advantages offered by this integration approach are high processing speed and low power consumption [4-5]. Because this technology allows the use of only one substrate supporting the whole system, this technology cannot be used to create our integrated microchannels. SoC is also a highly complex and expensive technology. SiP technology allows stacking-up multiple ICs vertically or horizontally in a single enclosed module. It is useful whenever different functions cannot be integrated in a single SoC or when different or incompatible technologies need to be integrated together in a single package [6]. The internal interconnects for inter-chip connections can be realized by wire-bonding, flip chip bonding or using through-silicon vias (TSVs). Creating integrated microchannels with this type of

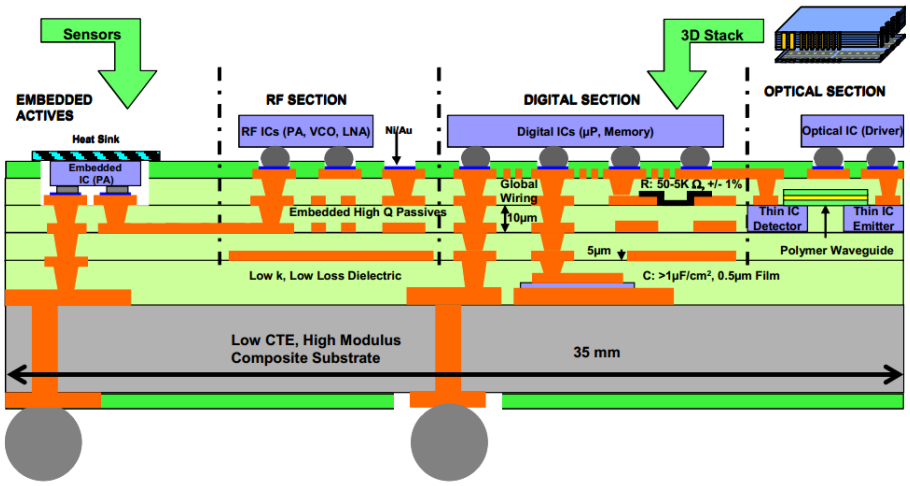

Fig. 1.1 A single SoP package integrating multiple technologies [7].

packages can theoretically be done, but in practice the applications are so numerous that the process quickly becomes expensive and inefficient because of the high customization aspect.

SoP is a more advanced packaging solution that can integrate several technologies with multiple functions into a highly dense and cost effective package [7]. SoP also allows multilayer integration by the means of inter-layer bonding and vertical interconnects. Fig. 1.1 illustrates the high number of functionalities and technologies that can be integrated in a single SoP system. As a final note, SoP technology seems to have all the characteristics needed to build the integrated microchanels we want to realize in this work. The only thing left at this point is to choose the adequate high frequency substrate that will be the base of our SoP microfluidic system. The following section discusses some of the possibilities.

1.2 Substrates for Multilayer RF Packaging

Substrates which are candidates to be used for modern RF packaging should at least exhibit the following characteristics: 1) low loss, 2) stable dielectric constant over the frequency band of interest and 3) multilayer integration capabilities. The substrates available today that meet more or less these requirements are ceramic and organic materials. Ceramics include aluminum oxide (alumina), aluminum nitride (AlN),

silicon carbide (SiC), high temperature co-fired ceramics (HTCC) and low temperature co-fired ceramics (LTCC). Examples of organic substrates include nearly pure polytetrafluoroethylene (PTFE), ceramic-filled PTFE, FR-4 and LCP. Because we are interested, in this work, in creating integrated microchannels inside the substrate, the multilayer characteristic is indeed very important.

Among the ceramics discussed above, co-fired ceramics are the ones capable of meeting the multilayer requirement. HTCC are types of ceramics that are derived from alumina, and prior to the development of LTCC, the multilayer structures were obtained by laminating several alumina plates and firing them with metals altogether at a temperature of 1600 °C [8]. The downside of using HTCC though is the high temperature of co-firing which restricts the types of metallization; that is why the only metals that can be used are the ones that can withstand temperatures higher than 1600 °C like tungsten and manganese [9]. It turns out to be that these metals have a low electrical conductivity compared to other good conductors like copper, silver or gold; these good conductors cannot be used for HTCC though because they melt at temperatures lower than 1100 °C [9]. The fact that low conductivity metals introduce more loss at higher frequencies makes HTCC not a very practical solution.

To address this issue, LTCC has been developed in the late 90s in order to make multilayer RF packages work at much higher frequencies. In contrast with HTCC, the process has changed in a way that the co-firing temperature is typically done at 850 °C [8]. This has consequently allowed the use of high conductivity materials for co-firing and, since then, has made it possible for many multilayer RF devices to be packaged using this technology for applications that require much higher frequencies [10-12]. All that being said, LTCC still has many limitations [13]: 1) only processed in small tiles, 2) expensive and complex process, 3) higher lead times, 4) non-polished substrates

(poor surface roughness) and 5) shrinkage in size after co-firing. For these various reasons that LTCC is not the option chosen in this work.

FR-4 and PTFE (Teflon from DuPont) are both printed circuit board (PCB) type of substrates. FR-4 has been the standard for years for PCB manufacturing. In spite of its proven reliability, low cost and multilayer capabilities, FR-4 has a relatively high dissipation factor /loss tangent ($\tan\delta \sim 0.02$), has a high moisture absorption (0.5 %), has a high linear coefficient of thermal expansion (CTE) (50 ppm/° C) and its dielectric constant ($\varepsilon_r = 4.5$) is sometimes not tightly controlled over the whole laminate (different composition ratios in some sections of the PCB) and varies quite significantly with frequency [14]. PTFE can be a possible alternative to FR-4 in order to improve the electrical properties at higher frequencies thanks to its low loss characteristics. However, everything comes at a cost, PTFE has a very high CTE (230 ppm/°C) which makes its processing very difficult and costly in the case of multiple thick layers integration, add to that the fact that PTFE usually requires non-standard PCB processing for circuit fabrication [14]. In addition, PTFE has a poor adhesion property which makes the lamination process more difficult. Hybrid multilayer PCBs (FR-4 and PTFE) can be used but come with a trade-off between the electrical properties and the system complexity. Ceramic-filled PTFE materials (RO3000 series and some RT/duroid series from Rogers) are particularly interesting because they are more forgiving in the circuit fabrication process and the typical overall CTE value is much lower than pure PTFE. The Z-axis CTE is also very low (~ 16 - 50 ppm/°C) which makes these materials good candidates for lamination and vertical integration without significant thickness variation [15]. These low cost materials are commercially available in large panels with a varied choice for thickness values but they suffer from a slightly degraded electrical

TABLE 1.1
COMPARATIVE TABLE BETWEEN FR-4, PTFE, AND CERAMIC-FILLED PTFE

	CTE (ppm/°C)	tanδ @ 10 GHz	Moisture Absorption (%)	Standard PCB Processing	Dimensional Stability	Multilayer Fabrication	Electrical Performance
FR-4	50	0.018	0.5	Excellent	Very good	Robust	Poor
PTFE	230	0.0018	0.02	Poor	Poor	Difficult	Excellent
Ceramic-filled PTFE	40	0.0013-0.0023	0.1	Good	Good	Moderate	Very good

**Based on data in [14].*

performance compared to pure PTFE [14]. Table 1.1 is a comparative table between FR-4, PTFE and ceramic-filled PTFE.

For many years, polydimethylsiloxane (PDMS) has been the "classical" choice for microchannel fabrication for biological and medical applications [16]. That is because PDMS offers many advantages [17]: it is a low cost material and optically transparent, it can easily be bonded to itself and to other materials and it can be doped/reinforced to alter its dielectric properties. It is also easy to mold, even when mixed with the cross-linking agent, the PDMS remains liquid at room temperature for many hours. The dielectric constant of PDMS can sometimes be changed by adding a specific percentage of ceramic powder [18], this property can be useful in order to synthesize PDMS materials with different dielectric constants. However, PDMS has some downsides: it has a higher dissipation factor [19] (tanδ = 0.05 @ 5 GHz) and it is a material that ages with time, therefore the mechanical properties of this material might change after a few years. Moreover, it is almost impossible to deposit metals and dielectrics on PDMS, a way to overcome this problem, but at the cost of an extra processing step, is to deposit metals on glass slides which can later be bonded to PDMS using plasma treatment. PDMS can also be very sensitive when exposed to some chemicals [20].

In recent years, alternative organic substrates such as LCP (ULTRALAM 3850 from Rogers) have been developed to meet the ever growing needs of RF packaging and to remedy some of the shortcomings that the other substrates suffer from, thanks to its excellent electrical and mechanical properties [21]. LCP is a flexible organic material that offers many advantages for RF applications: 1) low loss ($\tan\delta = 0.0025$ @ 10 GHz), 2) low cost, 3) commercial availability, 4) standard PCB processing, 5) large panel processing, 6) low temperature processing (285 °C), 7) extremely low moisture absorption (near-hermetic) (0.04 %), 8) low in-plane CTE (17 ppm/°C), 9) excellent dimensional stability, 10) high stability of the dielectric constant ($\varepsilon_r = 2.9$ @10 GHz) over temperature and frequency, 12) excellent adhesion to other materials, 12) multilayer integration and 13) flammability resistance. Given all these excellent properties, RF packaging on LCP has started to get momentum starting from the early 2000s and has since then attracted many RF packaging researchers' interest [22-26]. After all, LCP gathers all the positive aspects of other packaging substrates while retaining virtually none of their drawbacks. This is why LCP is chosen in this work for creating novel microfluidic RF packages for cooling and tuning purposes. The only real shortcoming of LCP is its low thermal conductivity (0.2 $W.m^{-1}.K^{-1}$) [21], but, apart from ceramics, LCP is not very far behind other organic substrates. That is why, a significant part of this research is dedicated to microfluidic cooling on LCP to address this issue. RO3003 is also used as the preferred support for the microchannels because of its low Z-axis CTE, its dielectric constant which is very close to that of LCP ($\varepsilon_r = 3$) and its availability in various thicknesses [27]. In the following section, we discuss some of the existing cooling techniques.

1.3 Thermal Management and Cooling Techniques

Thermal management is a very important aspect to consider in electronics because it helps improve the reliability of the system, extend its lifetime and prevent sudden failures caused by the overheating of some elements. Thermal management has become even more important with modern circuitry becoming much denser (e.g. microprocessors, CPUs and GPUs) resulting in higher power dissipation densities. Several cooling techniques can be used to dissipate the heat generated by the electronic components [28]. The four main categories that exist are heat sinks, air cooling, thermal vias and liquid cooling (Fig. 1.2). The most basic form of heat sinks are heat spreaders which are thin metal plates that come in contact with the hot device to "spread-out" the heat to a much larger surface area. Heat sinks can also take the form of thick metal plates/carriers or other high thermal conductivity materials that come in contact with the hot heat source. The most popular form of heat sinks are finned heat sinks which come mainly in two forms: pin-fin or plate-fin. The heat sink is often exposed to air, therefore most of the heat is getting dissipated through conduction and air convection. Depending on the heat sink used and the power densities involved, in many cases, the heat sink alone may not be sufficient to dissipate the heat as the cooling rate becomes lower than the heat generation rate. In this case, forced air cooling (through fans) is often combined with heat sinks to provide better dissipation rates, the typical convective heat transfer coefficient in this case is in the range of 10 - 1000 $W.m^{-2}.K^{-1}$ [29]. Liquid cooling can provide a far better performance, as an example, the convective heat transfer coefficient for water in a forced convection scenario is typically in the range of 50 - 10000 $W.m^{-2}.K^{-1}$ [29].

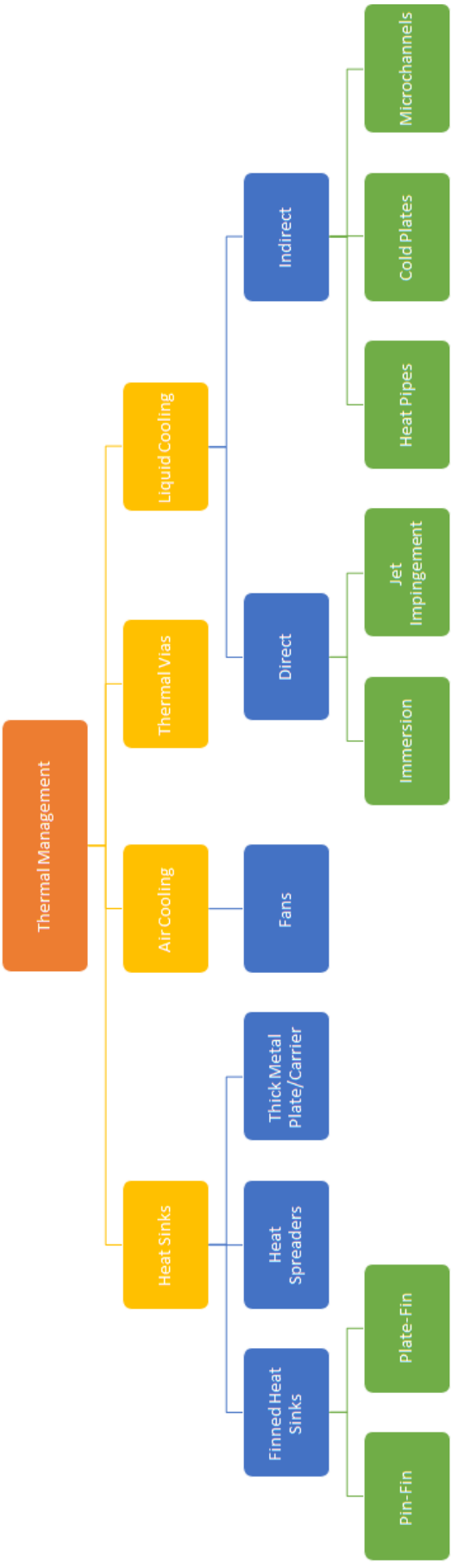

Fig. 1.2 Commonly used thermal management techniques.

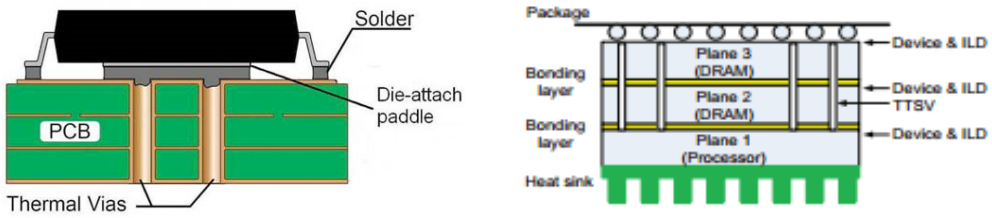

(a) (b)

Fig. 1.3 a) PCB-type vias [32] b) TTSVs [33].

To enhance the heat transfer from the heat source to the heat spreader in the first place, the use of thermal vias is a common practice. Beside their thermal transfer functionality, they can also serve as electrical interconnects between stacked layers. The thermal vias can be placed at the PCB level [30] and/or even at the silicon (Si) chip level [31] where they take the name of thermal through-silicon vias (TTSVs). Fig. 1.3 is an illustration of thermal vias on PCB and on silicon (TTSVs). Although the main purpose of using TSVs has originally been the creation of high performance interconnects for 3D IC stacking, TSVs turned out to be an effective means to reduce the temperature of 3D ICs. Many research papers have been focusing on studying and modeling the thermal effect of TTSVs.

In [33], Hu Xu et al. came up with two thermal models for TTSVs for a 3-D DRAM-μP and compared them with FEM simulations. However, there have been recently some doubts about the efficiency of TTSVs, in [34] the authors claim that the temperature reduction can be achieved by the means of metal bumps underneath the TTSVs rather than the TTSVs themselves.

For RF applications that require the integration of high power devices like RF power amplifiers or high power resistors, the heating effect due to the dissipated power becomes an important factor. For RF packaging, high thermal conductivity substrates such as AlN [35-36], which has been recently used to package a 6.5 W GaN PA [37], can be considered heat spreaders but they often need to be mounted on a more efficient (air-cooled) heat sink if the power densities involved are very high. Formulas and

models have been developed to predict the junction temperature of high power devices, for instance, an accurate closed-form analytical solution has been developed in [38] to calculate the junction temperature of power amplifier field effect transistors (FETs) or monolithic microwave integrated circuits (MMICs). As discussed earlier, air cooling can be combined with heat sinks to help address this issue, but because the power requirements for power electronics and RF high power devices have been constantly increasing, liquid cooling techniques seem to be more attractive solutions thanks to their excellent heat dissipation rates. In some scenarios, using liquid cooling turns out to be a necessity, this is especially true for substrates with poor thermal conductivity values like the case of LCP and all organic materials in general. Liquid cooling techniques can be divided into direct and indirect subcategories. Direct liquid cooling involves direct contact between the coolant and the heat source while indirect liquid cooling suggests that there is no contact between the two. The most commonly used techniques are immersion cooling [39] and jet impingement [40-41] for direct liquid cooling and heat pipes [42-43], liquid cooled cold plates [44] and microchannels [45-46] for indirect liquid cooling. These liquid cooling techniques are illustrated in Fig. 1.4.

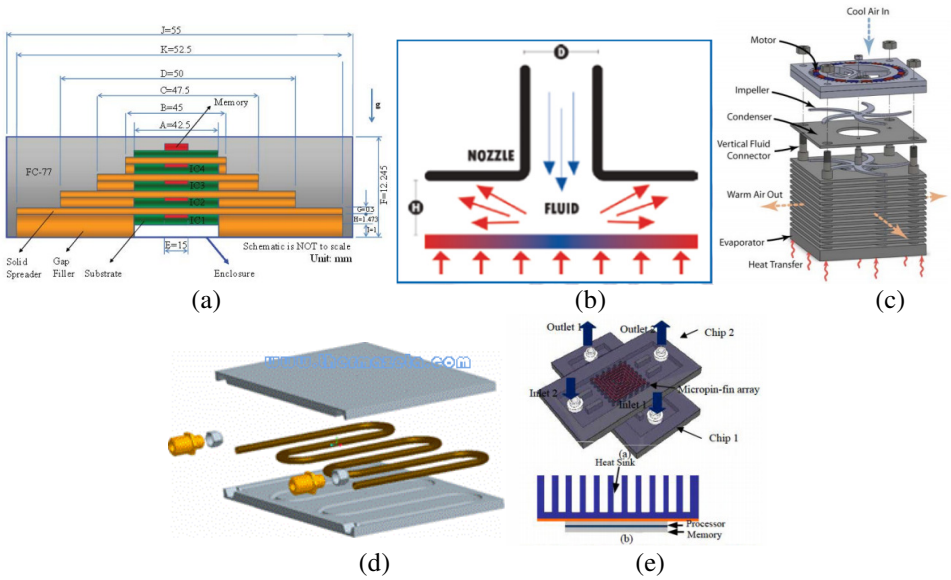

Fig. 1.4 Liquid cooling techniques: a) immersion cooling [39] b) jet impingement [47] c) heat pipes [42] d) liquid cooled cold plates [48] e) microchannels [45].

Microfluidic cooling with integrated microchannels is an attractive solution for multilayer organic substrates because it provides thermal and mechanical design flexibility with reduced design size and a superior convective heat transfer coefficient. This technique has been used for 3D-IC cooling on silicon type of substrates [49] and has also been implemented in LTCC technology [50]. Microchannel fabrication techniques in polydimethylsiloxane (PDMS) [51] and polyimide (PI) [52] have also been investigated. In the next section we discuss the state of the art for reconfigurable filters and PAs.

1.4 Tunable RF Filters and Power Amplifiers

Bandpass filters are important components of RF front ends used in wireless communication and radar systems. Implementing such filters in microstrip technology offers many advantages: 1) lower complexity, 2) reduced size and 3) low manufacturing cost. Filter designs at low frequencies, such as L and S bands, have the drawback of having a bigger size due to larger wavelength values. Techniques have been developed to deal with the size reduction [53]. In reconfigurable bandpass filters, the center frequency and/or the bandwidth is tuned. Reverse-biased varactor diodes have been used to tune the center frequency and the bandwidth of bandpass filters [54]. It has also been recently implemented on LCP [55]. RF micro-electromechanical systems (MEMS) techniques have been used to design tunable filters in L and S bands [56-57]. New tuning techniques have also emerged such as the use of microfluidics to tune: a) the absorption frequency of metamaterials [58]; b) microfluidic network to change the substrate dielectric constant by means of DI water [59]. Fig. 1.5 shows examples of tunable bandpass filters. Because tunable filters using microfuidics on organics have not been fully explored, this work details the design and the implementation of a tunable

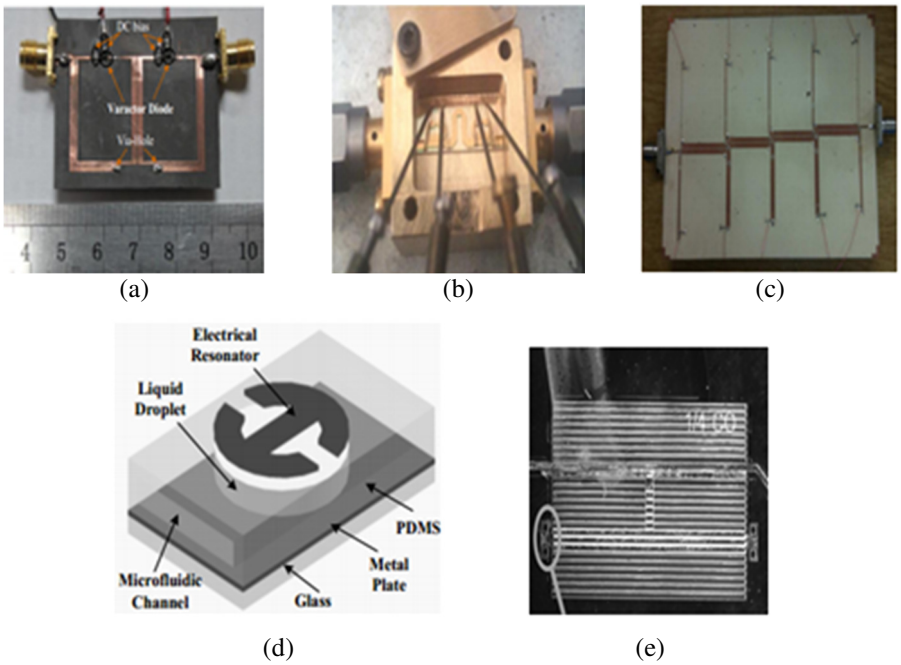

Fig. 1.5 Reconfigurable bandpass filters. Electronically: a) varactors [54] b) RF MEMS varactors [57] c) PIN diode [55]. Microfluidically: d) switchable metamaterials [58] e) microfluidic network [59].

L-band bandpass filter on an LCP layer sitting on top of a microfluidic channel. The center frequency was tuned by changing the fluid inside the channel.

RF PAs are essential components in any transmitter or transceiver module. The power requirements for such PAs have been consistently increasing, that is why GaN-based PAs have caught much attention recently [60]. Hybrid GaN devices have also been integrated on LCP for an X-band transmitter (Tx) module [61]. Tunable PAs are becoming increasingly important for multiple band applications because they allow decreasing the number of required PAs in the system and thus reducing the complexity. Several techniques have been investigated in the past to design reconfigurable PAs: 1) the use of high-Q band stop filters at the output of the PA for second harmonics removal at low frequencies [62], 2) the use of voltage-controlled BST varactors [63] and 3) the use of reconfigurable MEMS-based matching networks [64]. Fig. 1.6 shows examples for tunable RF PAs. Microfluidics have not been used before to design tunable PAs, that is work describes a novel way to combine the advantages of organic substrates and

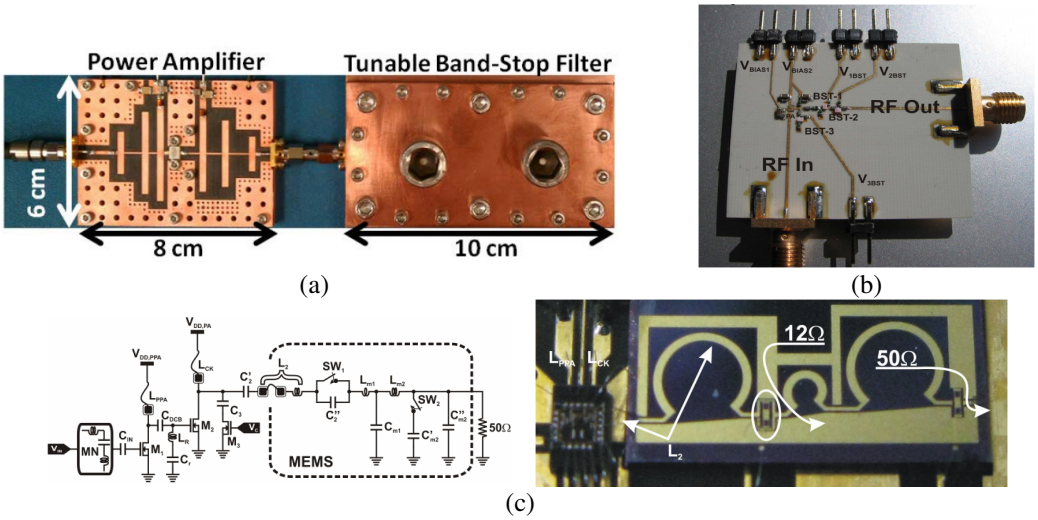

Fig. 1.6 Reconfigurable PAs using: a) tunable high Q band-stop filters [62] b) voltage controlled BST varactors [63] c) MEMS [64].

the high power capabilities of GaN devices by designing a reconfigurable GaN-based PA that can work optimally at two different frequencies based on the fluid injected inside the matching networks' micromachined channels.

PART I

INTEGRATED MICROFLUIDIC COOLING ON MULTILAYER ORGANIC SUBSTRATE

"I believe there are no questions that science

can't answer about a physical universe."

-Stephen Hawking

Heat management is an important aspect of any system on package especially when a significant amount of heat is being generated from the different mounted components on the board. Because organic substrates are bad thermal conductors in general (e.g. the thermal conductivity of LCP is 0.2 $W.m^{-1}.K^{-1}$), microfluidic cooling on such substrates becomes an attractive solution because: 1) it offers a higher heat dissipation rate compared to other cooling solutions, 2) microchannels can be selectively placed beneath the different hot spots and can be easily integrated with the rest of the organic structure, 3) it offers thermal and mechanical flexibility, 4) it maintains a small size and footprint, and 5) it is a cost-effective solution. The heat sources which have been tested on these microfluidic organic packages are active GaN/GaAs RF HEMT dies and passive surface mount thin film resistors with different power ratings. A thermal model has also been developed for the analysis of such microchannels on multilayer organic substrates.

CHAPTER 2

STATIC COOLING OF A GAN DEVICE ON MULTILAYER ORGANIC SUBSTRATE

Recently, the integration of III-V devices on LCP has been demonstrated, but at lower power levels and with air-cooling [61]. A microfluidic channel on an LCP-silicon stack-up has also been investigated [65], as well as silicon based microchannels [49]. In this section, a microfluidic channel has been integrated on LCP to cool an X-band 1 W GaN device using a static (non-moving) mixture of ethylene glycol and water.

2.1 Theoretical Formulations

Two material-stack configurations (Fig. 2.1) are chosen to assess the thermal properties of the proposed solution. A perfect heat sink (copper) at ambient temperature is assumed at the bottom of both structures. Because the fluid is static, the concept of thermal resistance is well adapted for both configurations, since calculations using thermal resistances of the structures are only valid when there is a combination of solids and non-moving fluids. The thermal resistance of each layer is then given by Table 2.1.

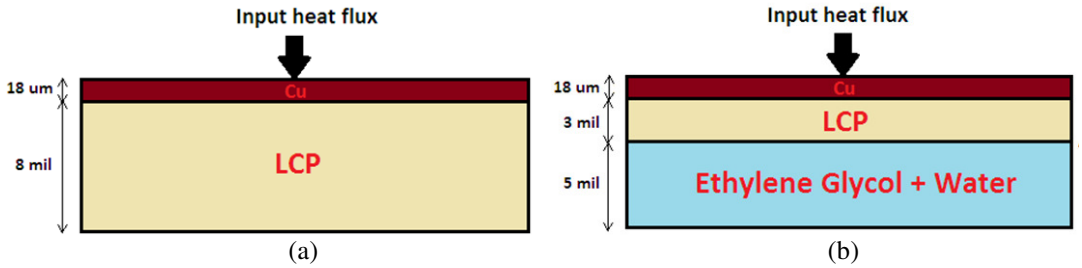

Fig. 2.1 a) Configuration 1: Copper + LCP
b) Configuration 2: Copper+LCP+Fluid

TABLE 2.1
THEORETICAL THERMAL RESISTANCES OF THE DIFFERENT LAYERS

	k ($Wm^{-1}K^{-1}$)	t (µm)	R_{th} (KW^{-1})
Cu	401	18	0.0561
LCP 1	0.2	203.2	1270
LCP 2	0.2	76.2	476.25
EG + H20 (%50:%50)	0.398	127	398.87

The equations below were used, where A is the die active area (1 mm x 0.8 mm):

$$R_{th} = \frac{Thickness}{Thermal\ conductivity\ \times\ Active\ Surface\ area} = \frac{t}{k \times A} \tag{2.1}$$

$$R_{th\_config1} = R_{th\_Cu} + R_{th\_LCP1} = 1270.1\ KW^{-1} \tag{2.2}$$

$$R_{th\_config2} = R_{th\_Cu} + R_{th\_LCP2} + R_{th_{EG+H_2O}} = 875.2\ KW^{-1} \tag{2.3}$$

The mixture of water and ethylene glycol (%50:%50) has a thermal conductivity (0.398 $W.m^{-1}.K^{-1}$) [66] comparable to that of LCP (0.2 $W.m^{-1}.K^{-1}$) [21] at 20 °C. Therefore, the total thermal resistances from the two configurations are of the same order. The cooling effect is then not demonstrated through the intrinsic thermal properties of the coolant itself but from the motion of the fluid. A slight improvement is noticed however for configuration 2 due to the lower value of the thermal resistance compared to configuration 1.

2.2 3D Thermal Simulations

The improvement in configuration 2 is demonstrated through simulations in COMSOL where a 3D electro-thermal model of the real structure is created with 1) LCP only, 2) copper only, 3) LCP and a static fluid and 4) LCP and a dynamic fluid. The chip (1 mm x 0.8 mm) is modeled as a heat source dissipating 2W of power. The length and width of the chip are very small compared to those of the 3 mil thick LCP substrate (2 inch x 4 inch). The cavity beneath the LCP, where the fluid is injected, is 5 mil thick. Fig. 2.2 depicts the simulated steady state which is reached after 10 minutes in the package with the static fluid.

A second simulation has also been performed, the power generated from the chip has been swept from 2 W to 10 W in 2 W increments. This sweep has been applied to each of the four models mentioned above. The simulation results in Fig. 2.3 show

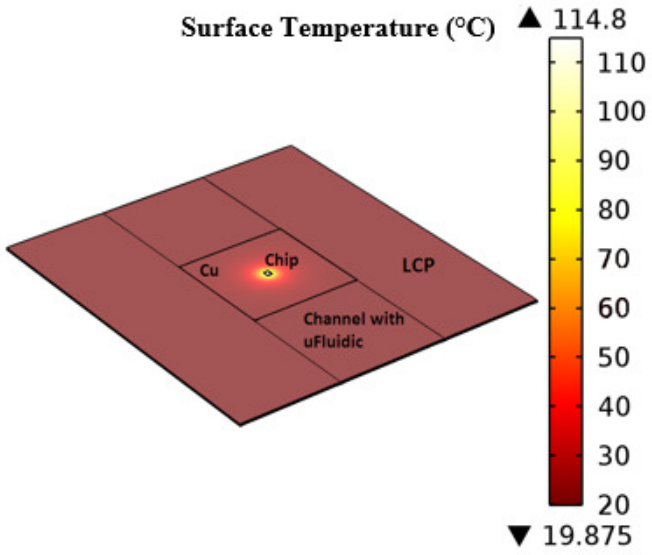

Fig. 2.2 COMSOL simulation of a GaN chip lying on top of LCP substrate with a microfluidic channel heat sink.

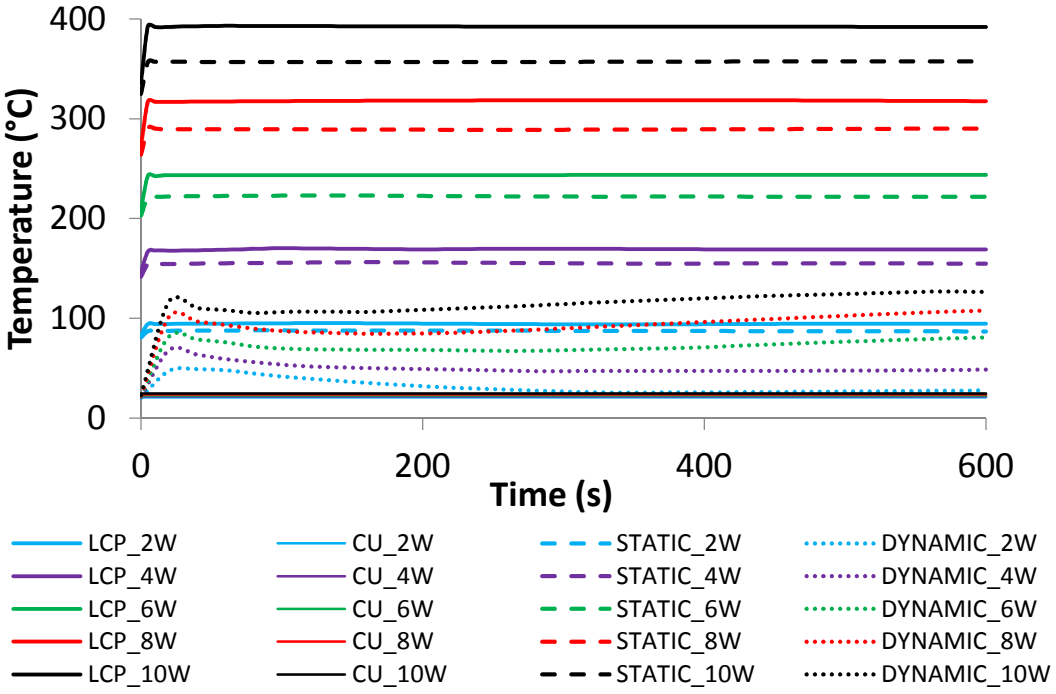

Fig. 2.3 Power sweep of generated heat from 2W to 10 W for LCP, copper, static fluid and dynamic fluid.

that efficient cooling is obtained mainly by the motion of the coolant in the cavity. The difference in the resultant package temperature becomes significantly critical as the dissipated DC power is increased. Though at low powers the improvement in performance between the static fluid and LCP-only packages is minimal, it can be seen

that the temperature difference between the two rises proportionally with DC power, thereby offering a greater benefit in the high-power applications.

2.3 Package Fabrication

The fabrication process starts with a 2 inch x 4 inch double-clad LCP sheet with a thickness of 8 mil. The copper is then etched from the bottom side of the LCP where a cavity of 5 mil is ablated. The cavity dimensions are 2.2 inch x 0.7 inch. 1.2 mm vias are also drilled and serve as access points for the coolant. A 1 mil bond ply is put beneath the LCP and is used to laminate the LCP to a 140 um copper sheet to seal the cavity. Copper was chosen as it presents a solid and stable support and acts as a heat sink removing a part of the heat carried out by the coolant. The top copper is etched to open up the vias and pattern metal sheets on top of which will sit the PA chips for characterization. A detailed fabrication flow diagram is shown in Fig. 2.4.

The PAs (4 x 65 um GaN dies biased for Class AB operation) under test are mounted on the metal sheet using silver epoxy and cured at a temperature of 140 °C for around 40 minutes. The fluid used in the experiment is a mixture of ethylene glycol and water with equal proportions. The water (k_{H2O} = 0.6 $Wm^{-1}K^{-1}$) acts as the effective coolant but the Ethylene Glycol ($k_{E.Glycol}$ = 0.27 $Wm^{-1}K^{-1}$) increases the boiling point

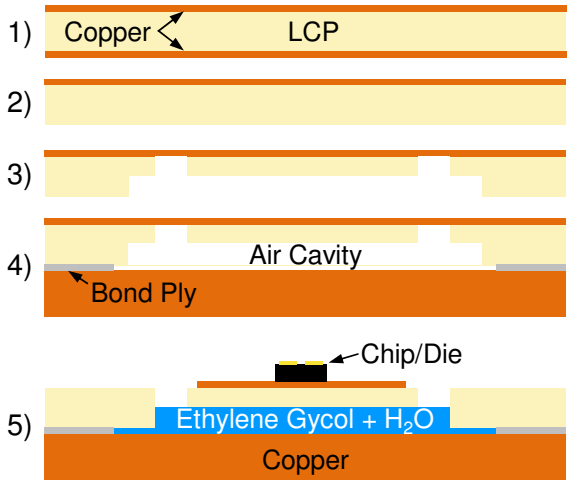

Fig. 2.4 Package fabrication flow. 1) Double clad LCP 2) Copper etching from bottom side 3) Cavity ablating and via drilling 4) Lamination 5) Final micro-machined structure.

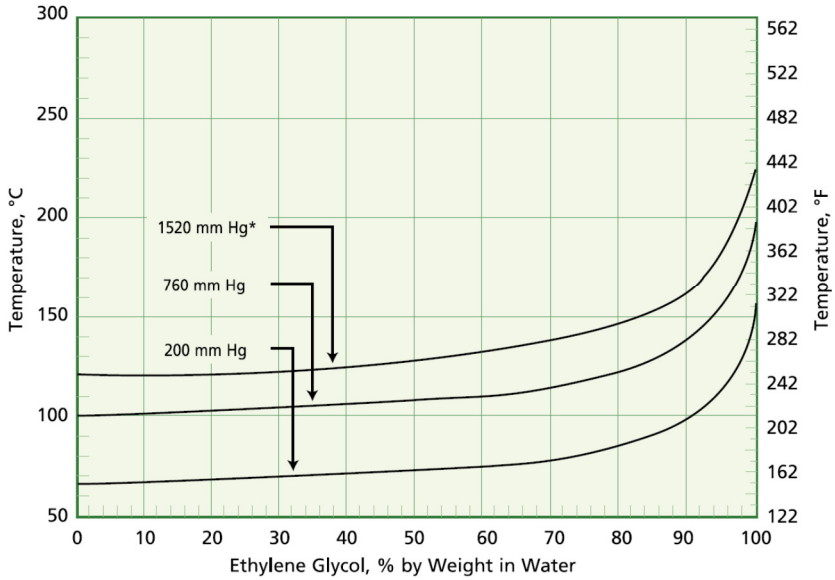

Fig. 2.5 Boiling point vs Percentage of Ethylene Glycol in water [66].

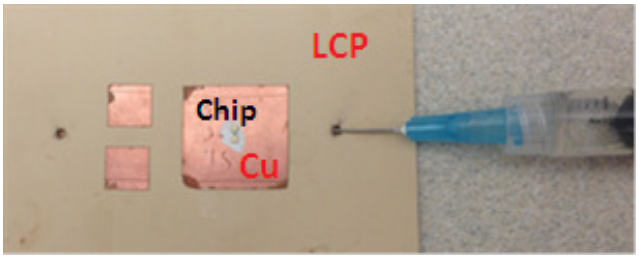

Fig. 2.6 Ethylene Glycol+Water injection into the micro-cavity.

of the mixture from 100 °C to 107 °C (Fig. 2.5). Fluid injection is performed using a syringe to fill up the whole cavity. Because we study the static case, pumping mechanisms are not needed. Finally we seal the fluid access points by putting a tape to trap the liquid inside the micro-cavity. Fig. 2.6 shows the injection of the fluid.

2.4 Measurement Results

To evaluate the suitability of the microfluidic package, two performance parameters were considered: DC-IV characteristics and transient response. We would like to compare first the DC-IV curves of the die sitting on a microfluidic channel with those of the die sitting on a metal chuck. The tests were carried out by directly probing the die. Maury Microwave's Automated Tuner System (ATS) was used to measure the I-V characteristics, conduct load-pull measurements as well as the consequent power sweeps.

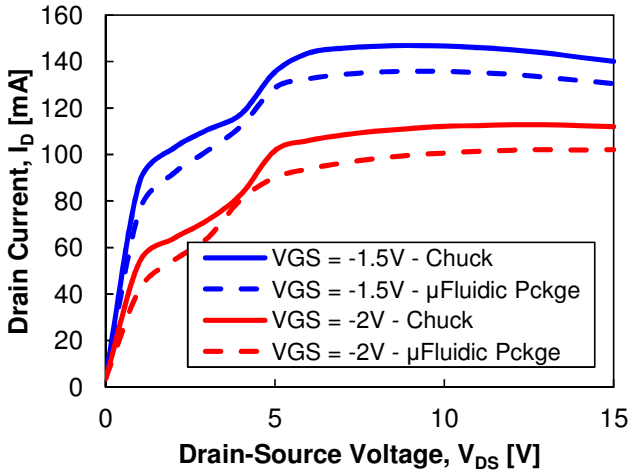

Fig. 2.7 A comparison of the GaN HEMT's I-V output characteristic.

The output characteristic (V_{DS} vs. I_D) of the device either on the metal chuck or the package is shown in Fig. 2.7. It can be clearly seen that for a given bias point, I_D is larger in the case where the device is tested on the chuck. This illustrates that heat is more readily removed from the device, thus avoiding current decay.

Source- and load-pull measurements were conducted to identify the optimum impedances for maximum gain. These corresponded to Z_{source} = 13.18 + j50.06 Ω and Z_{load} = 51.02 + j43.6 Ω. A transient response was measured for a constant input power (P_{in} = 7 dBm), frequency (f = 10.5 GHz) and source/load impedances (optimal),

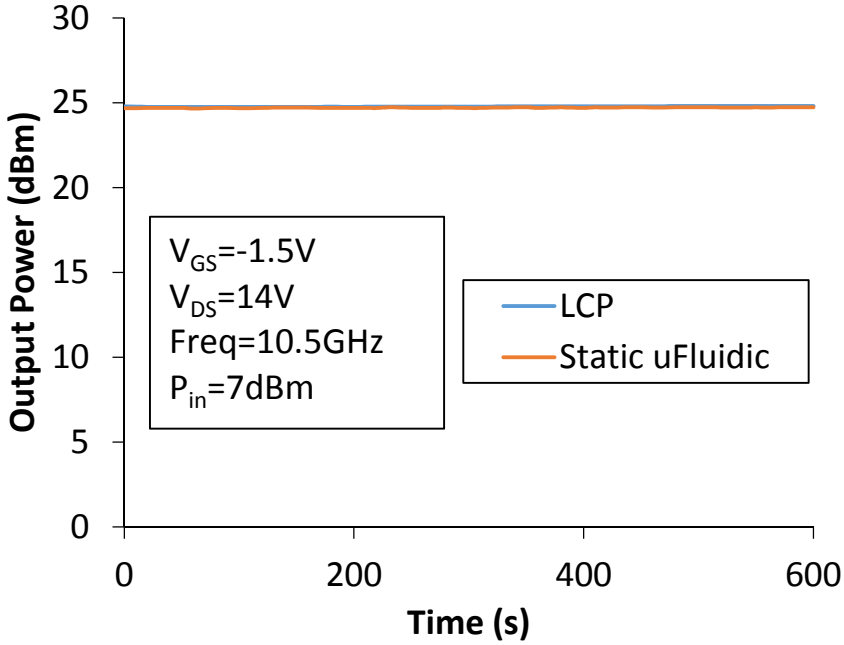

Fig. 2.8 Transient response of the die, comparing performance on LCP only and static microfluidic.

sampling output power every 10 seconds over a period of 10 min. The biasing conditions are V_{DS} = 14V and V_{GS} = -1.5 V. This input power level corresponds to a PAE of 15% and the biasing conditions indicate a consumption of 1.68 W of DC power. The effective DC power dissipated through heat is then 1.68 W x 85% = 1.428 W. Under these conditions, it was observed (Fig. 2.8) that the die sitting on LCP or static microfluidics does not result in markedly different performance levels, once again supporting the simulations performed.

2.5 Summary

A microfluidic channel has been integrated into a flexible, low-cost and organic package. The channel was filled with a mixture of ethylene glycol and water. Thermal simulations, which compare the use of LCP only, a static fluid or a dynamic fluid, have been carried out. Finally, a GaN-based X-band PA has been demonstrated on this micromachined package with static fluid and showed no significant difference in performance with comparison to tests done on LCP only, thus clearly demonstrating the need for dynamic microfluidics in future packages in order to mitigate thermal effects in high-power applications with such materials.

CHAPTER 3

DYNAMIC COOLING OF HIGH POWER PASSIVE AND ACTIVE DEVICES ON MULTILAYER ORGANIC SUBSTRATE

It has been demonstrated in the previous chapter that a dynamic (moving) fluid is required in these types of microfluidic structures to provide efficient cooling especially for high power applications. Therefore, this chapter describes the implementation of a multilayer organic microfluidic structure with: 1) dynamic DI water, and 2) high power heat sources. Because of the motion of the fluid inside the microchannel, it is not possible anymore to use the simple thermal resistances calculations used in the last chapter. Therefore, a more complete and complex model is required to predict the total thermal resistance of the system. The details of the modeling part is discussed in the next chapter.

3.1 General Model for a Packaged Heat Source

Before discussing the dynamic cooling case, it is very important to understand the heat source specifications and its power limitations in order to extract the thermal properties of the heat sink to be used. For that, a simplified version of a packaged heat source is shown in Fig. 3.1. This general model includes:

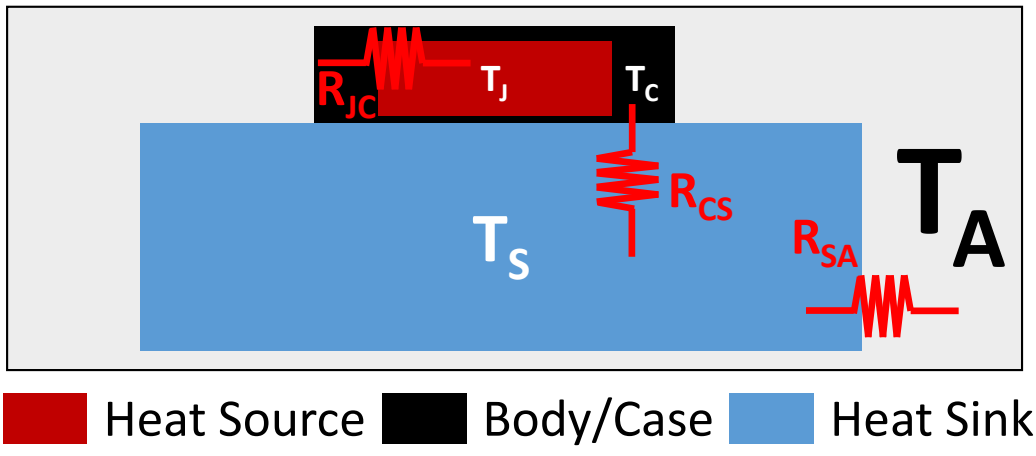

Fig. 3.1 Simplified model of a packaged heat source on top of a heat sink with a representation of various interface thermal resistances.

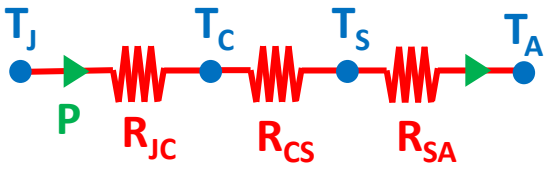

Fig. 3.2 Packaged heat source lumped thermal model.

- A heat source: can be a resistor, a PA, or any source of heat. We assume a temperature T_J (junction temperature).
- Case (or body): used to package the heat source and can be made of different materials and sizes. We assume a temperature T_C for the case.
- A heat sink: can be a large metal chuck, thermal vias, heat pipes, microfluidic channel or any heat sink. We assume a temperature T_S for the heat sink.
- Ambient temperature: the initial condition for the temperature of the system at t=0 is set to T_A.

The thermal resistances in Fig. 3.1 can be rearranged in what is known as the lumped thermal model as shown in Fig. 3.2, where the dissipated power P and the temperature nodes T_i can be assimilated to an electrical current and to electrical voltages respectively. The different thermal resistances are derived as follows:

Junction-to-Case thermal resistance:	$R_{JC} = \frac{T_J - T_C}{P}$	(3.1)
Case-to-Sink thermal resistance:	$R_{CS} = \frac{T_C - T_S}{P}$	(3.2)
Sink-to-Ambient thermal resistance:	$R_{SA} = \frac{T_S - T_A}{P}$	(3.3)
Case-to-Ambient thermal resistance:	$R_{CA} = R_{CS} + R_{SA} = \frac{T_C - T_A}{P}$	(3.4)
Junction-to-Ambient thermal resistance:	$R_{CA} = R_{JC} + R_{CS} + R_{SA} = \frac{T_J - T_A}{P}$	(3.5)

The junction temperature T_J and the case temperature T_C can be derived from (3.1) and (3.4) respectively and can be rewritten as:

$$T_J = T_C + R_{JC}P \tag{3.6}$$

$$T_C = T_A + R_{CA}P \tag{3.7}$$

Depending on the technological and dimensional characteristics of the heat source, a temperature $T_{J_{max}}$ is always specified as the maximum junction temperature of the heat source. So the idea behind any cooling scheme is to maintain the following inequality at all times:

$$T_J \leq T_{J_{max}} \tag{3.8}$$

By using (3.6), the inequality in (3.8) can be rewritten as:

$$T_C \leq T_{C_M}(P) \tag{3.9}$$

or:

$$P \leq P_M(T_C) \tag{3.10}$$

where:

$$T_{C_M}(P) = T_{J_{max}} - R_{JC}P \tag{3.11}$$

$$P_M(T_C) = min\left(\frac{T_{J_{max}} - T_C}{R_{JC}}, P_{max_{DS}}\right) \tag{3.12}$$

where $P_{max_{DS}}$ is the maximum power rating specified by the datasheet at a certain temperature $T_{C_{max}}$ (also denoted as $P_{max_{DS}}@T_{C_{max}}$) which is given by:

$$T_{C_{max}} = T_{C_M}\left(P_{max_{DS}}\right) = T_{J_{max}} - R_{JC}P_{max_{DS}} \tag{3.13}$$

$T_{C_{max}}$ is the maximum case temperature for a heat source dissipating $P_{max_{DS}}$ of power, the power starts to immediately to derate for case temperatures above $T_{C_{max}}$ with a slope of $1/R_{JC}$. $T_{C_M}(P)$ represents the maximum case temperature for a given dissipated power while $P_M(T_C)$ represents the maximum dissipated power for a given case temperature. The heat source power derating curve (Fig. 3.3) can be derived from (3.10) and (3.12) by visualizing P as a function of T_C. It can be seen from Fig. 3.3 and (3.13) that R_{JC} can be expressed as:

$$R_{JC} = \frac{T_{J_{max}} - T_{C_{max}}}{P_{max_{DS}}} \tag{3.14}$$

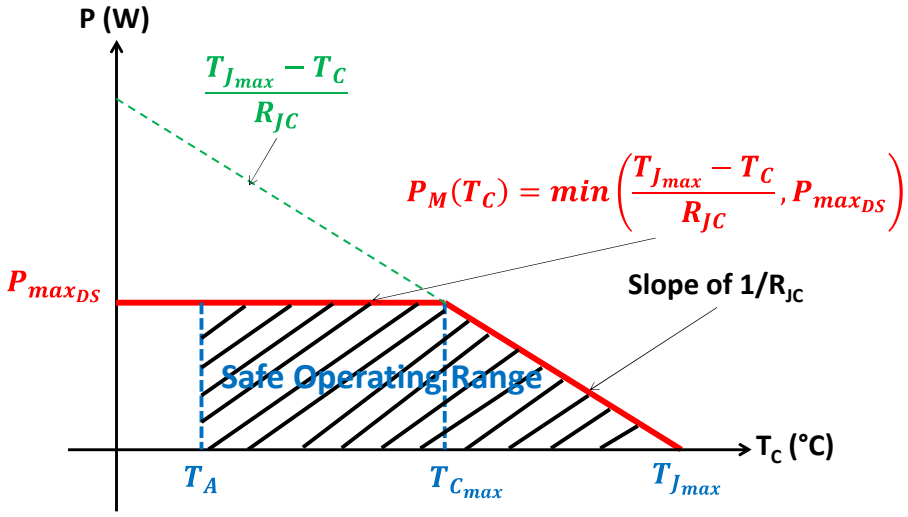

Fig. 3.3 Heat source power derating curve (dissipated power safe operating range).

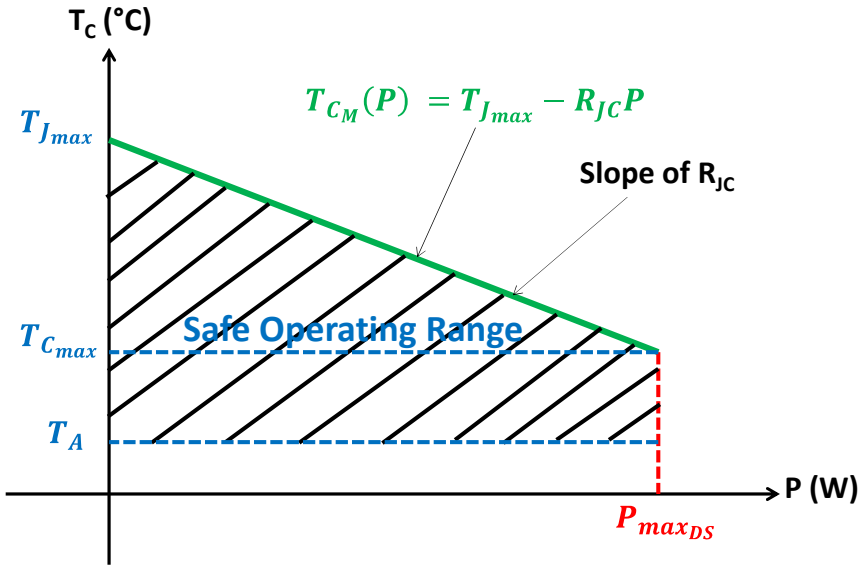

Fig. 3.4 Case temperature safe operating range.

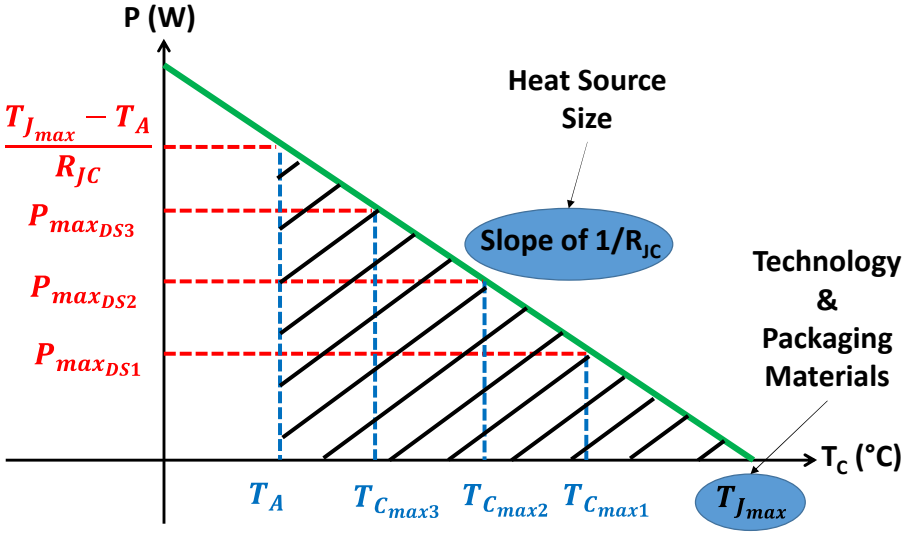

Fig. 3.5 Infinite values of ($P_{max_{DS}}$, $T_{C_{max}}$) pairs in the solid black region.

The heat source safe operating range can also be visualized by plotting T_C as a function of P (Fig. 3.4). From Fig. 3.3, it can be noted that the value of the pair ($P_{max_{DS}}$, $T_{C_{max}}$) is not unique as any combination along the dashed green line would also be valid (Fig. 3.5). The theoretical extreme boundaries of such pairs are ($\frac{T_{Jmax}-T_A}{R_{JC}}$, T_A) and (0, $T_{J_{max}}$), but in practice it is usually the case that $0 < P_{max_{DS}} < \frac{T_{Jmax}-T_A}{R_{JC}}$ and $T_A < T_C < T_{J_{max}}$. It can be proven that, given a pair ($P_{max_{DS1}}$, $T_{C_{max1}}$) for a certain heat source, the new pair ($P_{max_{DS2}}$, $T_{C_{max2}}$) can be calculated using the following equations:

For a fixed $T_{C_{max2}}$: $$P_{max_{DS2}} = \frac{T_{J_{max}} - T_{C_{max2}}}{T_{J_{max}} - T_{C_{max1}}} P_{max_{DS1}} \tag{3.15}$$

For a fixed $P_{max_{DS2}}$: $$T_{C_{max2}} = T_{J_{max}} - \frac{T_{J_{max}} - T_{C_{max1}}}{P_{max_{DS1}}} P_{max_{DS2}} \tag{3.16}$$

In Fig. 3.5, $T_{J_{max}}$ is determined based on the heat source technology and the packaging materials used. For example, the typical value of $T_{J_{max}}$ for GaAs and AlN is 150 °C while $T_{J_{max}}$ reaches 225 °C for GaN. The physical dimensions of the heat sources affect the value of R_{JC}, in general R_{JC} is a decreasing function of the heat source surface area. Based on this analysis, $T_{J_{max}}$ and R_{JC} are the only hard values fixed by the physical implementation, the values of $P_{max_{DS}}$ and $T_{C_{max}}$ can vary as depicted in Fig. 3.5. It is extremely important to specify the maximum power rating $P_{max_{DS}}$ at a certain temperature $T_{C_{max}}$, for example, given the same heat sink characteristics, a power resistor on an AlN substrate ($T_{J_{max}} = 150\ °C$) rated at 50 W @ 100 °C ($R_{JC} = 1\ °C/W$) can be easily cooled compared to a resistor rated at 50 W @ 70°C ($R_{JC} = 1.6\ °C/W$). That is why, it may be confusing for many people to distinguish between the two scenarios, it can often be very misleading to only say that the heat source is a 50 W resistor without specifying the maximum case temperature. Another example is to note that two power resistors based on the same technology (e.g. $T_{J_{max}} = 150\ °C$) rated at

50 W @ 25 °C and 20 W @ 100 °C respectively are actually the same (by using (3.15) and (3.16)).

To extract the constraints that the heat sink should satisfy for a certain heat source, (3.8) can be rewritten as:

$$R_{CA} \leq R_M(P, T_A) \tag{3.17}$$

where:

$$R_M(P, T_A) = \frac{T_{J_{max}} - T_A}{P} - R_{JC} \tag{3.18}$$

A sufficient condition on R_{CA} can be obtained to satisfy (3.17) by writing:

$$R_{CA} \leq R_{CA_{max}}(T_A) \tag{3.19}$$

where:

$$R_{CA_{max}}(T_A) = R_M\left(P_{max_{DS}}, T_A\right) = \frac{T_{C_{max}} - T_A}{P_{max_{DS}}} \tag{3.20}$$

It has to be noted that the case-to-ambient thermal resistance R_{CA} is equivalent to the heat sink thermal resistance. Therefore, $R_{CA_{max}}(T_A)$ represents the maximum heat sink thermal resistance at a certain ambient temperature T_A in order to maintain the junction temperature of the heat source below $T_{J_{max}}$ (or to satisfy (3.8)). Fig. 3.6 is a plot of R_{CA} as a function of the dissipated power P.

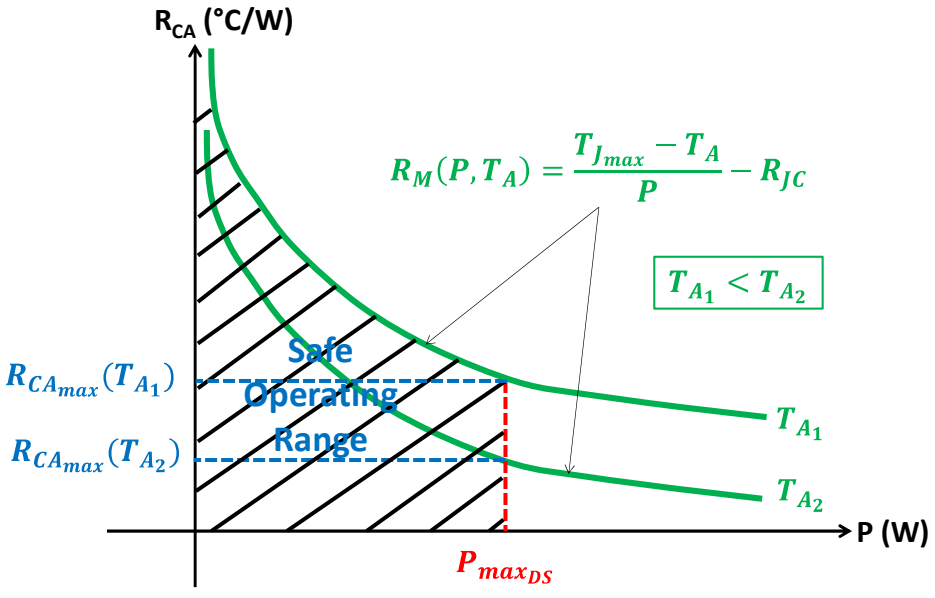

Fig. 3.6 Heat sink thermal resistance safe operating range.

Equation (3.20) and Fig. 3.6 show that $R_{CA_{max}}$ is a decreasing function of T_A which validates the intuition that the constraints on the heat sink should be "tougher" when the ambient temperature is higher.

(3.14) and (3.20) give a mean of immediately extracting the thermal properties of the heat source and the heat sink at the same time by only using the information given in the heat source power derating curve (Fig. 3.3). An example of a real derating curve for a commercial 20 W @ 100 °C power resistor is shown in Fig. 3.7 (a percentage of $P_{max_{DS}}$ is used instead of $P_{max_{DS}}$ in the y-axis in order to be able to reuse the same derating curve for the same resistors made out of the same technology). The thermal information can be easily calculated: $R_{JC} = \frac{150-100}{20}\ °C/W = 2.5\ °C/W$ and $R_{CA_{max}}$ can be evaluated using different values of T_A, e.g. $R_{CA_{max}}(25\ °C) = \frac{100-25}{20}\ °C/W = 3.75\ °C/W$ and $R_{CA_{max}}(85\ °C) = \frac{100-85}{20} = 0.75\ °C/W$.

By using (3.7), it can be seen that T_C is a first order linear function of P, so in order to experimentally determine R_{CA}, one can sweep the power P and record several data points $T_C(P)$, the slope of the resulting line is exactly R_{CA}. As a final note, any given heat sink does not have a fixed thermal resistance R_{CA}. R_{CA} depends on the heat source to be cooled as well, the general trend shows that R_{CA} goes down as R_{JC} goes down.

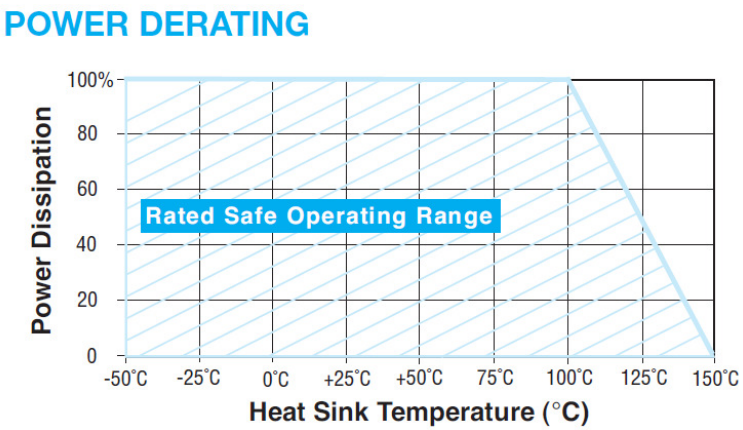

Fig. 3.7 Power derating curve of a commercial 20 W @ 100 °C power resistor [67].

3.2 Organic Heat Sink Stack-up and Heat Sources Description

The organic microfluidic heat sink consists of a 50.8 um (2 mil) layer of LCP on top of a 381 um (15 mil) Duroid channel where the fluid can circulate. Fig. 3.8 is a cross sectional view of the multilayer structure along with the different dimensions. The thermal model for such a complex structure is described in the next chapter.

The passive heat source used in this experiment is a 20 W surface mount thin film resistor derated at $T_C = 100\,°C$ for a maximum junction temperature rise of $T_{J_{max}} = 150\,°C$. The junction-to-case thermal resistance of this device is $R_{JC} = 2.5\,°C/W$. To operate this device at its full power rating ($P_{max_{DS}} = 20\,W$), the equivalent maximum thermal resistance that should be presented by any heat sink, at an ambient temperature $T_A = 25\,°C$ is $R_{CA_{max}}(25\,°C) = 3.75\,°C/W$. The resistive element used is tantalum nitride on an aluminum nitride substrate. The size of the resistor is 6.22 mm x 6.22 mm. Fig. 3.9 is a top view picture of the resistor.

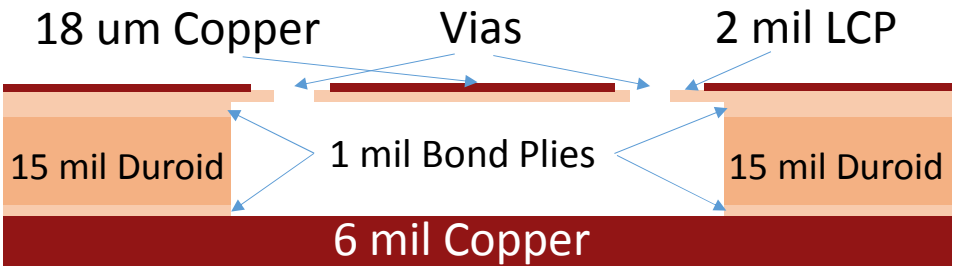

Fig. 3.8 Cross section of the multilayer organic structure.

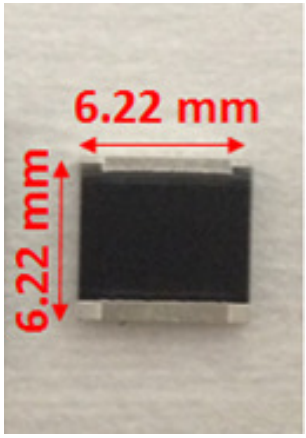

Fig. 3.9 Top view of the 20 W resistor heat source.

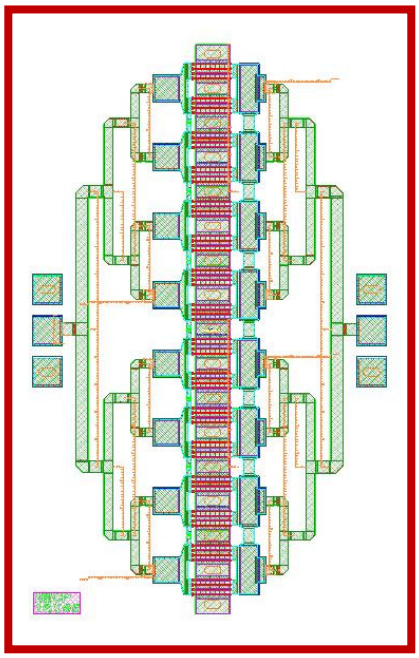

Fig. 3.10 16 x 0.5 mm GaAs bar die layout.

The active device is a 5 W discrete power GaAs HEMT, it was fabricated using standard 0.25 um power pHEMT production process. It consists of 16 unit cells with a gate width of 0.5 mm each. The power density for this process is 1 W per millimeter gate width, which translates into a total maximum power dissipation of 8 W for the actual die. A power divider and a power combiner are positioned at the gate and drain side respectively. The RF input and output ports are Ground-Signal-Ground (GSG). The overall size of the active area of the die is 2 mm x 1.5 mm. Fig. 3.10 shows the layout design of the discrete GaAs bar die.

3.3 Fabrication Procedure

For the fabrication procedure, 15 mil double copper clad RO3003 panel is used with a size of 6 inch x 6 inch. The copper is etched out from both sides of RO3003 and 1.4 inch x 0.6 inch cavities are ablated on it. This sheet is then placed between two bond plies that are 1 mil thick. Copper is etched out from one side of a 2 mil ULTRALAM 3850 sheet and vias with a diameter of 1.2 mm are drilled on it using a CO_2 laser. A 6 mil copper shim is placed at the bottom to ensure a good mechanical support of the

structure and to enhance heat dissipation thanks to copper excellent thermal conductivity (401 $Wm^{-1}K^{-1}$). The top metal layer is patterned to open up the vias. For continuous fluid injection and circulation, 2.4 mm tubes are attached to the vias, using a commercial plastic epoxy, one of the tubes is connected to a micropump. Fig. 3.11 (a) shows a disassembled channel where the capping LCP layer was removed. The resistor is soldered to the top metal layer along with electrical wires for biasing (Fig. 3.11 (b)), a small layer of thermal paste is placed beneath the resistor to enhance the thermal transfer. For the active device, the GaAs die is first attached to a 6 mil copper shim using indium silver, then the shim is soldered to the top surface of the microfluidic channel where a small layer of thermal paste is deposited (Fig. 3.11 (c)). Following this procedure offers many advantages: 1) good adhesion of the indium silver 2) capability of testing the die on the shim before attaching it to the microchannel 3) providing a flat mechanical support for the die 4) increasing the surface area of the interface layer between the die and the microchannel 5) avoiding the use of other poor thermal conductors for die-attach.

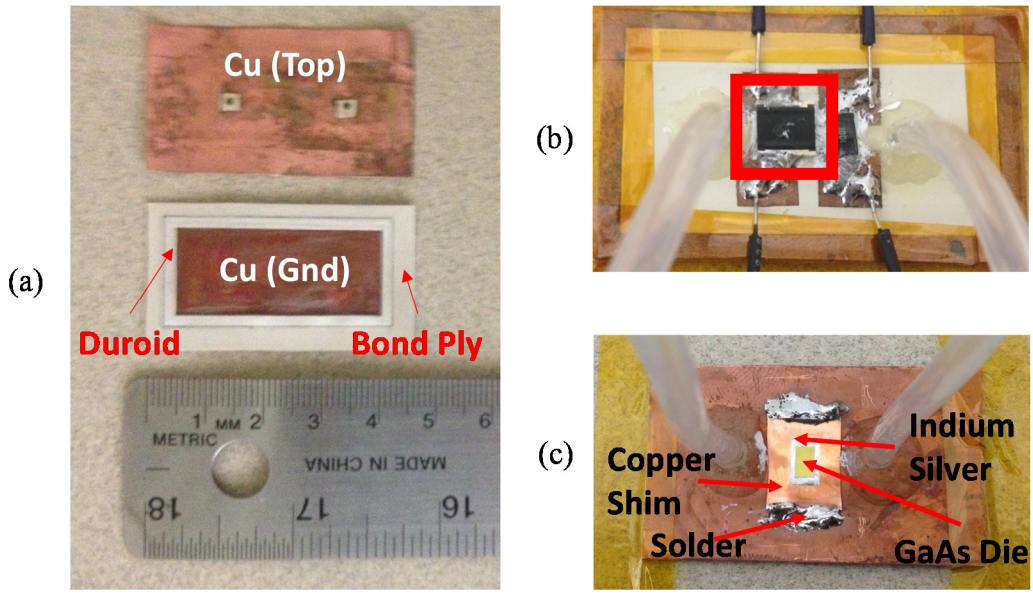

Fig. 3.11 a) Disassembled microfluidic channel.
b) Passive resistor on a microfluidic channel.
c) Active die on a microfluidic channel.

3.4 Measurements and Results

The case temperature of the resistor is measured using a 40 AWG K-type thermocouple placed at the resistor-LCP contact plane. The water temperature is 25 °C and the flow rate ranges from 300 ml/min to 350 ml/min. Fig. 3.12 compares modeled and measured temperature gradients for static and dynamic water. The results show that the resistor can be cooled up to 12.3 W dissipated power with water flow at room temperature, while the maximum dissipated power should not exceed 7 W in case of no water flow. The measured thermal resistance of the heat sink in the case of water flow (7.69 °C/W) is higher than the value calculated in Section 3.2 (3.75 °C/W), which explains why the resistor cannot reach its full maximum power rating of 20 W.

The GaAs die is biased for DC operation using 150 um GSG probes. When the GaAs die is DC biased, all of the power is dissipated into heat, which makes it a good case study in terms of thermal heat dissipation. Under RF operation, the power added efficiency (PAE) becomes non zero, at that point the dissipated power P_{dissip} can be determined for any input power level based on load pull measured data (Fig. 3.13) using the following equation:

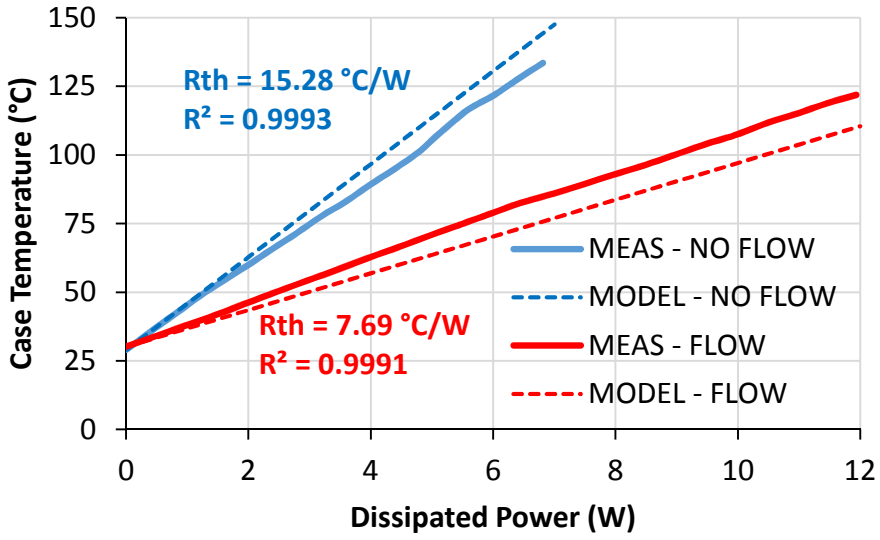

Fig. 3.12 Measured and modeled case temperature vs dissipated power.

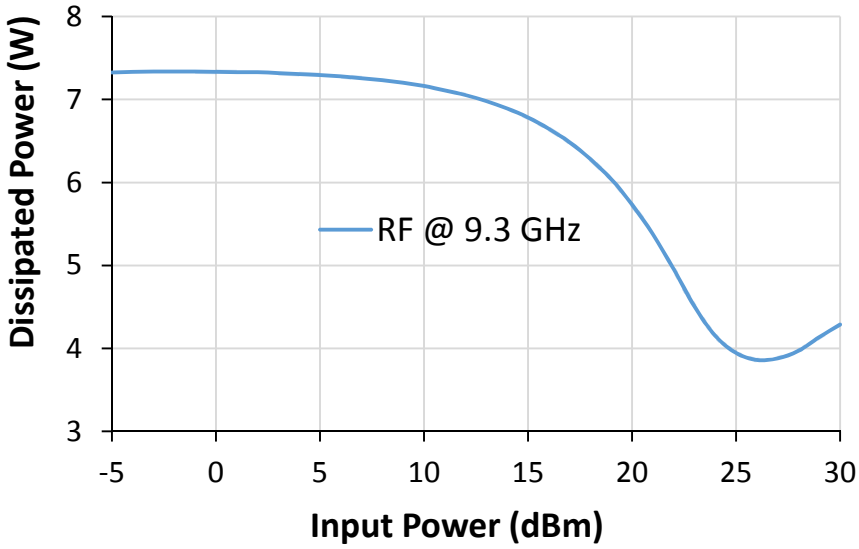

Fig. 3.13 Measured dissipated power vs input power for the GaAs die at 9.3 GHz.

$$P_{dissip} = (P_{out} - P_{in}) \times \frac{1 - PAE}{PAE} \tag{3.21}$$

where P_{in} and P_{out} are respectively the input and output power of the transistor. The analogy between RF and DC lies in the choice of the right quiescent point in DC mode that makes the transistor dissipate the same amount of heat in the RF regime. The temperature measurements are taken using IR thermal imaging.

The active die is placed on a metal chuck with a baseplate temperature of 60 °C. The water temperature is 25 °C and is pumped into the microchannel with a flow rate ranging from 300 ml/min to 350 ml/min. Results using the IR camera (Fig. 3.14) show that the center region is heating up while the source and drain fingers should be the only regions dissipating the maximum heat. The explanation to that may come from the non-perfect contact of the metal chuck and the channel that is slightly bent to allow a smooth fluid circulation. The die could still be cooled down to operate at 3.45 W at 60°C using this cooling technique for a maximum junction temperature of 130 °C. 2.45 W is the maximum dissipated power at 60 °C in the case of static water.

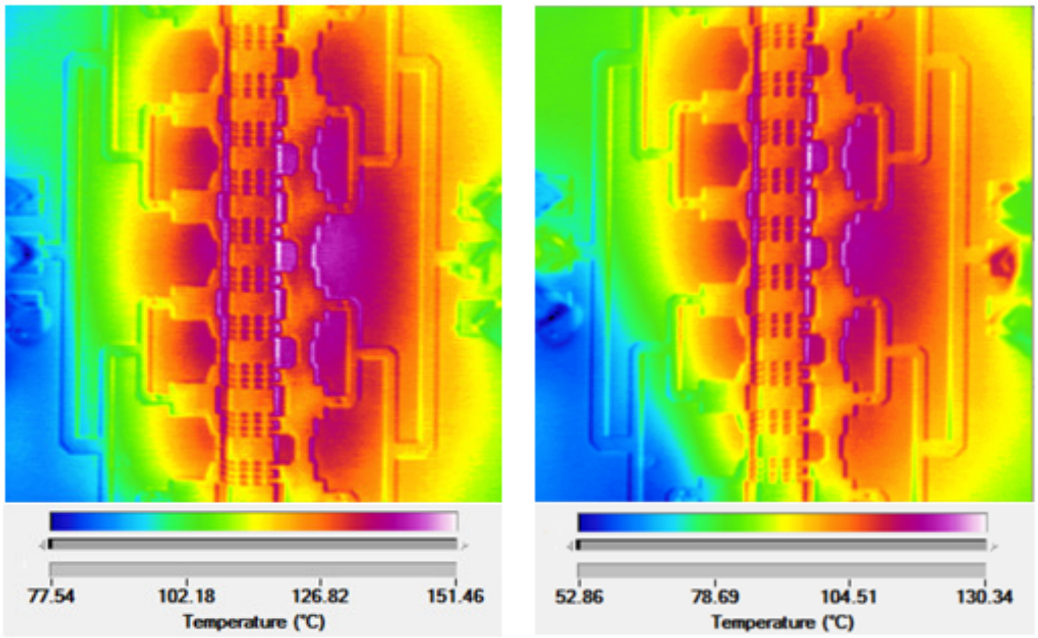

(a) (b)

Fig. 3.14 IR thermal image of the GaAs die with a power dissipation of 2.45 W with a) no water flow b) water flow.

3.5 Summary

An integrated microfluidic solution for cooling high power devices on multilayer organic substrate has been presented. A 20 W surface mount thin film power resistor was cooled by circulating DI water inside a 15 mil thick microfluidic channel. The passive device could be operated up to 12.3 W with flowing water at 25 °C, showing a net improvement of 5.3 W compared to the no flow case. A 5 W discrete power GaAs pHEMT was cooled to operate at 3.44 W at 60 °C compared to 2.45 W operation despite the fact that the die was showing minor thermal degradation due to the non-uniform heat distribution at the interface layer between the microchannel and the metal chuck. The passive resistor was cooled efficiently because it presented a bigger active surface area compared to the active die.

CHAPTER 4

THERMAL MODELING OF MICROFLUIDIC CHANNELS ON MULTILAYER ORGANIC SUBSTRATE

It has been stated in the last chapter that a simple model cannot accurately predict the thermal behavior of the microfluidic system because of the motion of the fluid inside the microchannel and because of the complex geometries involved. Therefore, this chapter presents a complete thermal model to fully predict the thermal resistance of the microfluidic structure. The model is validated by comparing the values extracted from the model with real measurements. In order to get a reliable comparison, several heat sources with different power ratings and sizes have been used as well as microchannels with different thicknesses.

4.1 Thermal Model

The multilayer microfluidic structure consists of a 50.8 um (2 mil) LCP layer with a micromachined Duroid channel beneath it. The microchannel thicknesses studied are 254 um (10 mil), 381 um (15 mil), 508 um (20 mil) and 762 um (30 mil). The surface mount resistors are modeled as uniform rectangular heat sources sitting on top of the LCP layer. The spreading of the heat is subject to four concurrent heat transfer mechanisms: conduction, forced convection, natural convection and thermal radiation. An important factor to consider as well is the spreading effect that is occurring at the top layer because of the small heat source to substrate area ratios. It will be shown later that natural convection and thermal radiation can be neglected for the scope of this work. Fig. 4.1 shows the layers of the microfluidic organic structure along with the different types of heat transfer involved. Table 4.1 gives the dimensions and the thermal conductivities for each individual layer.

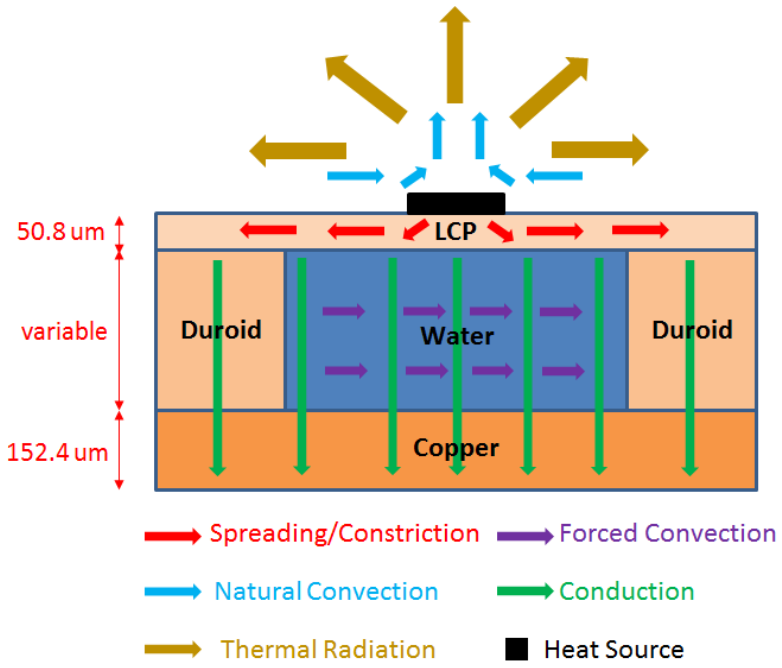

Fig. 4.1 2D cross section of the multilayer organic structure with heat circulation paths.

TABLE 4.1
LAYERS PROPERTIES OF THE MICROFLUIDIC STRUCTURE

Layer No.	Layer Material	Thermal Conductivity – k (W/(m.K))	Thickness - t (um)
1	Cu	401	152.4
2	Duroid	0.5	254, 381, 508 or 762
	DI water	0.6	254, 381, 508 or 762
3	LCP	0.2	50.8

4.1.1 Multilayer Heat Transfer

A part of the dissipated heat travels from the bottom carrier of the resistor and propagates in a 3D isotropic way along the LCP layer. The temperature distribution calculations should take into account the multilayer nature of the structure. For a quick but less accurate approximation, an average value of cross-plane and in-plane thermal conductivities can be used to estimate the effective thermal conductivity of the structure [68]:

Cross-plane thermal conductivity:

$$k_s = \frac{\sum_{i=1}^{3} t_i}{\sum_{i=1}^{3} t_i / k_i} \tag{4.1}$$

In-plane thermal conductivity:

$$k_p = \frac{\sum_{i=1}^{3} t_i k_i}{\sum_{i=1}^{3} t_i} \tag{4.2}$$

Effective thermal conductivity: $k_{eff} = Average(k_s, k_p)$ (4.3)

where t_i and k_i are respectively the thickness and thermal conductivity of layer i, i = 1..3. To simplify the calculation over layer 2, DI water and Duroid can be assimilated into one single layer of thermal conductivity $t_2 = 0.6\, W/(m.K)$. This is a valid approximation since the thermal conductivities of the two materials have very close values, however this can only be applied to the static DI water case. In (4.3) the average function can be a harmonic, a geometric or an arithmetic mean. The problem with this approach is that k_{eff} depends on the average function used, the averaged values are spread out between k_s and k_p (Table 4.2). The other problem is the fact that this simplistic model does not take into account the heat spreading effect. Therefore, using the known formula $R = \frac{L}{k_{eff}A}$ to predict the heat sink thermal resistance yields erroneous values.

TABLE 4.2
EFFECTIVE THERMAL CONDUCTIVITY WITH THREE DIFFERENT AVERAGE FUNCTIONS

Harmonic Mean	Geometric Mean	Arithmetic Mean
$\frac{2k_sk_p}{k_s + k_p}$	$\sqrt{k_sk_p}$	$\frac{k_s + k_p}{2}$
1.08 W/(m.K)	5.88 W/(m.K)	32.13 W/(m.K)

*values calculated for a microchannel thickness t_2 = 762 um (30 mil).

To solve this issue, an exact recursive relation was developed by Albers in [69] to calculate the steady-state surface temperature for any number of layers in a multilayer structure. The solution presented in [69] is adapted to the microfluidic structure illustrated in Fig. 4.1 with the following conditions: 1) there is a unique rectangular heat source placed at the center of the structure, 2) layer 2 is replaced with uniform DI water, 3) the heat generated by the heat source is uniform and constant over time, 4) the temperature is evaluated at the center of the heat source and 5) the boundary condition (B.C.) at the bottom Cu layer is an isothermal B.C. (this is a limitation of the model).

TABLE 4.3
MULTILAYER THERMAL RESISTANCE

Entity	Description	Unit	Expression	
$R_{multi}(x,y)$	multilayer thermal resistance	°C/W	$\frac{1}{L_x L_y}\left(\sum_{i=1}^{N}\frac{t_i}{k_i}+\frac{4}{k_N}\sum_{(n,m)\neq(0,0)}^{+\infty}\frac{U(n,m)\tau_N(n,m)\cos\left(\frac{n\pi x}{L_x}\right)\cos\left(\frac{m\pi y}{L_y}\right)}{(\delta_{n,0}+1)(\delta_{m,0}+1)\gamma(n,m)}\right)$	(4.4)
$U(n,m)$	heat source geometrical distribution factor – general form	-	$\int_0^{L_x}\int_0^{L_y}U(x,y)\cos\left(\frac{n\pi x}{L_x}\right)\cos\left(\frac{m\pi y}{L_y}\right)dxdy$	(4.5)
$U(n,m)$	heat source geometrical distribution factor – single heat source	-	$\cos\left(\frac{n\pi}{L_x}\left(p_x+\frac{S_x}{2}\right)\right)sinc\left(\frac{n\pi}{L_x}\frac{S_x}{2}\right)\cos\left(\frac{m\pi}{L_y}\left(p_y+\frac{S_y}{2}\right)\right)sinc\left(\frac{m\pi}{L_y}\frac{S_y}{2}\right)$	(4.6)
$(p_x,\ p_y)$	bottom left corner coordinates of the heat source	m	$\left(\frac{L_x-S_x}{2},\frac{L_y-S_y}{2}\right)$	(4.7)
$(n,m),\ \tau_N(n,m)$	thermal recursion relation	-	$tanh(\gamma t_1),\quad \frac{k_{N-1}tanh(\gamma t_N)+k_N\tau_{N-1}}{k_{N-1}+k_N\tau_{N-1}tanh(\gamma t_N)}$	(4.8)
$\tau_N(0,0)$	thermal recursion relation – ($\gamma\rightarrow 0$)	-	$k_N\gamma\sum_{i=1}^{N}\frac{t_i}{k_i}$	(4.9)
$\gamma(n,m)$	separation of variables constant	m^{-1}	$\sqrt{\left(\frac{n\pi}{L_x}\right)^2+\left(\frac{m\pi}{L_y}\right)^2}$	(4.10)
$\delta_{i,0}$	Kronecker delta	-	1 if i = 0, 0 otherwise	

*S_x x S_y and L_x x L_y are the respective areas of the heat source and the LCP layer. N = 3.

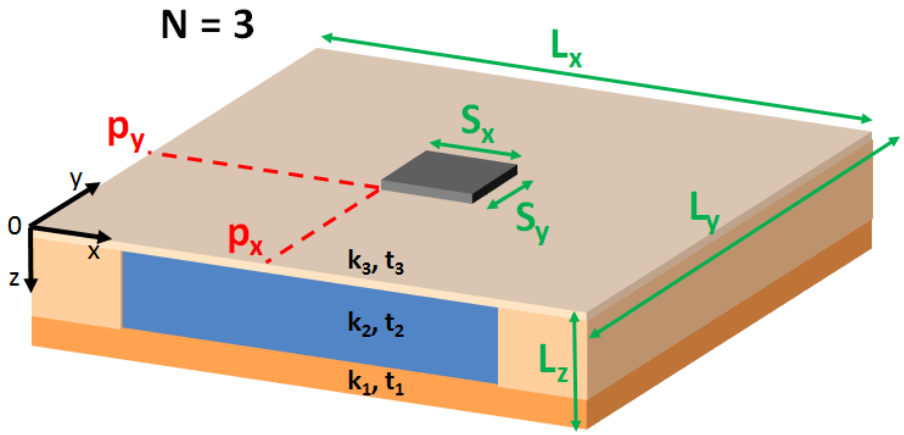

Fig. 4.2 Multilayer model adapted to the microfluidic case study.

Fig. 4.2 shows a 3D view of the structure. Table 4.3 summarizes the formulas needed to compute the multilayer thermal resistance. The thermal resistance in (4.4) is derived from (23) in [69], which is the top surface temperature formula for an N-layer structure. The series diverges for (n,m)=(0,0), therefore the corresponding term has been calculated in (4.9) by developing the recursive formula in (4.8) for a very small γ ($\gamma\rightarrow 0$). Equation (4.5) is the dimensionless geometrical distribution factor and is simplified into a closed-form expression in (4.6) for the single heat source case.

4.1.2 Forced Convection

As discussed in the previous section, the multilayer model allows only an isothermal B.C. at the bottom layer ($T = T_0$). When dealing with dynamic water, forced convection requires a Robin B.C. at that layer with a convective heat transfer coefficient h ($\frac{\partial T}{\partial z} = -\frac{h}{k}(T - T_0)$). Therefore, the previous model only works for solid and static layers. To model the forced convection effect, a thermal model has been developed by Lee et al. in [70] to estimate the temperature rise for a circular heat source centered on top of a single circular layer with convective cooling at the sink surface. In contrast with Albers model, although Lee's solution works only for a single layer, it uses a Robin B.C. which allows defining a convective coefficient h at the bottom boundary. For the single layer case, Albers model is in fact a particular case of Lee's model when $h \to \infty$. Fig. 4.3 is a 3D view of the equivalent structure of the microfluidic stack-up adapted for convective cooling modeling. A_s and A_p are the surface areas of the heat source and the microchannel layer respectively, t is the thickness of LCP, k is the thermal conductivity of LCP and h is the convective heat transfer coefficient originating from DI water motion inside the microchannel. Because this study focuses on rectangular geometry, it is necessary to transform the rectangular problem into a circular one using the following equations as given in [70]:

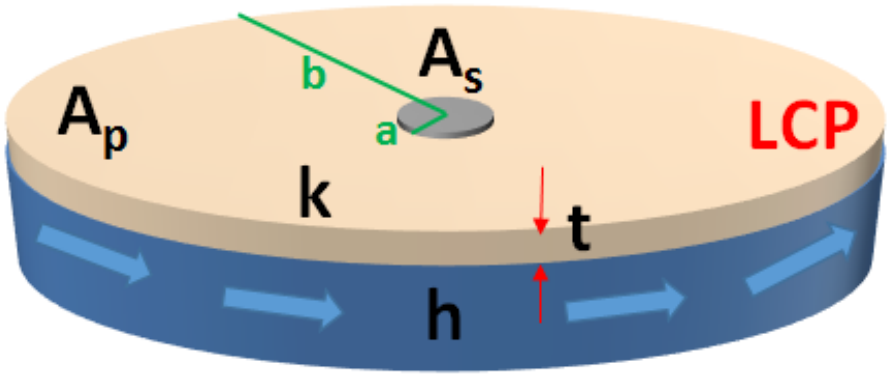

Fig. 4.3 Convective model adapted to the microfluidic case study.

$$a = \sqrt{\frac{A_s}{\pi}} \tag{4.11}$$

$$b = \sqrt{\frac{A_p}{\pi}} \tag{4.12}$$

The relative error introduced by this transformation is insignificant when the area ratio $\frac{A_s}{A_p}$ is small; the error increases when this ratio becomes large. However, for large area ratios, the constriction resistance is often much smaller than other thermal resistances in the system that this error has minimal to no effect on the overall thermal resistance. Dimensionless parameters are calculated from A_s, A_p, k, t and h: $\epsilon = a/b$, $\tau = t/b$, $Bi = hb/k$. The forced convection thermal resistance is given by:

$$R_{fc} = \frac{1}{k\sqrt{A_s}}\left(\frac{\epsilon\tau}{\sqrt{\pi}} + \frac{\epsilon}{\sqrt{\pi}Bi} + \frac{2}{\sqrt{\pi}}\sum_{n=1}^{\infty}\frac{J_1(\lambda_n\epsilon)}{\lambda_n^2 J_0^2(\lambda_n)}\Phi_n\right) \tag{4.13}$$

where J_0 and J_1 are Bessel functions of the first kind of order 0 and 1. λ_n is the nth root of J_1 and Φ_n is given by:

$$\Phi_n = \frac{tanh(\lambda_n\tau) + \frac{\lambda_n}{Bi}}{1 + \frac{\lambda_n}{Bi}tanh(\lambda_n\tau)} \tag{4.14}$$

R_{fc} can also be written as:

$$R_{fc} = R_m + R_f + R_c \tag{4.15}$$

where:

$$R_m = \frac{1}{k\sqrt{A_s}}\frac{\epsilon\tau}{\sqrt{\pi}} = \frac{t}{kA_p} \tag{4.16}$$

$$R_f = \frac{1}{k\sqrt{A_s}}\frac{\epsilon}{\sqrt{\pi}Bi} = \frac{1}{hA_p} \tag{4.17}$$

$$R_c = \frac{1}{k\sqrt{A_s}}\frac{2}{\sqrt{\pi}}\sum_{n=1}^{\infty}\frac{J_1(\lambda_n\epsilon)}{\lambda_n^2 J_0^2(\lambda_n)}\Phi_n \tag{4.18}$$

While the parameters k, t, A_s and A_p can be easily determined, h is a non-constant coefficient and depends on three parameters: the fluid intrinsic properties, the fluid flow rate and the channel geometry and dimensions. The fluid intrinsic properties are the viscosity, the thermal conductivity, the specific heat and the density. All these parameters vary with the fluid temperature. The channel geometry is also an important factor, rectangular channels are investigated in this study, Fig. 4.4 shows an illustration of such channels.

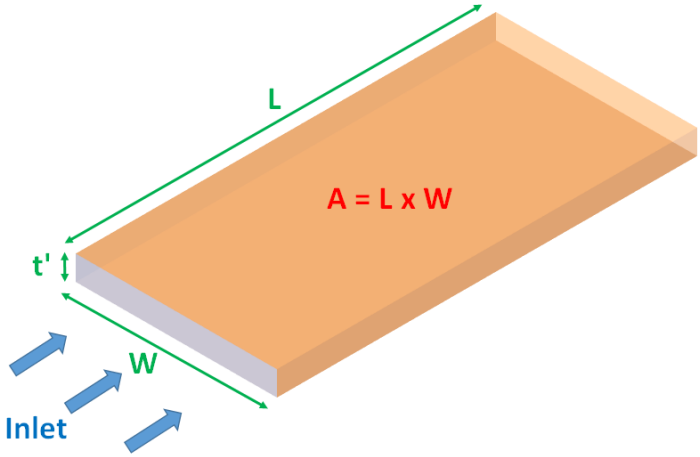

Fig. 4.4 Flow in rectangular microchannels.

The procedure to calculate h is to determine the Nusselt number through some approximate correlations. Many correlations can be found in literature [71] and they all depend on the type of flow: 1) laminar, transitional or turbulent, 2) hydrodynamically/thermally developing or fully developed, 3) constant heat flux or constant temperature. In all studied cases in this chapter, the type of flow is laminar because the Reynolds number satisfies $Re < 2300$. The experimental study in this work involves sweeping the power dissipated by a heat source, which translates into a constant heat flux problem. In order to assess whether the flow is thermally developing or fully developed, the channel length L is compared to the thermal and hydraulic entry lengths L_t and L_h. For a laminar flow, these lengths are given by [72]:

$$L_t = 0.05\, RePrD_h \tag{4.19}$$

$$L_h = 0.05\, ReD_h \tag{4.20}$$

In this work, the flow is thermally developing because $L_h < L < L_t$.

In order to derive general formulas to see how h varies as a function of the different system parameters, a correlation for thermally developing laminar flow with a constant heat flux in circular ducts is used [73]:

$$Nu = \begin{cases} 1.953\left(RePr\dfrac{D_h}{L}\right)^{1/3} & RePr\dfrac{D_h}{L} \geq 33.3 \\ 4.364 + 0.0722\, RePr\dfrac{D_h}{L} & RePr\dfrac{D_h}{L} < 33.3 \end{cases} \tag{4.21}$$

where the hydraulic diameter is defined in the case of rectangular channels as:

$$D_h = \frac{2Wt'}{(W + t')} \tag{4.22}$$

The convective coefficient is related to the Nusselt number by the relation:

$$h = \frac{Nu\, k'}{D_h} \tag{4.23}$$

This correlation can be written as a general expression of the form $a + b\left(RePr\frac{D_h}{L}\right)^{1/n}$, the following derivations are based on this general form. It can be shown that:

$$hA \underset{\varepsilon=\frac{t'}{W}}{=} c_1\left[\left(\frac{L}{\varepsilon}\right)^{\frac{n-1}{n}}(1+\varepsilon)^{\frac{n-2}{n}}\right] + c_2\left[\left(\frac{L}{\varepsilon}\right)(1+\varepsilon)\right] \tag{4.24}$$

where c_1 and c_2 are two non-geometrical constants, $\varepsilon = \frac{t'}{W}$ is the thickness to the width ratio of the channel and L is the channel length. The overall goal is to minimize R_{fc}. Based on equations (4.15) to (4.18), the important parameters that can influence R_{fc} are h, A and hA ($R_{fc}(h, A, hA) = R_m(A) + R_f(hA) + R_c(h, A)$). In (4.24), h and A are not independent, because of that it is important to consider hA as a separate variable to assess the influence of the geometrical parameters. As an example, if the value of W decreases while maintaining a constant ε then hA does not change but h increases. Table 4.4 shows the direction of variation of different parameters when the channel

TABLE 4.4
VARIATION OF THE CONVECTION THERMAL RESISTANCE WITH CHANNEL THICKNESS AND WIDTH

	ε	A	h	hA	R_m	R_f	R_c	R_{fc}
$t' \searrow$	$\searrow$	-	$\nearrow$	$\nearrow$	-	$\searrow$	$\searrow$	$\searrow$
$W \searrow$	$\nearrow$	$\searrow$	$\nearrow$	$\searrow$	$\nearrow$	$\nearrow$	$\searrow$	$\searrow$[a]

[a] R_m and R_f are very small compared to R_c for $W > W_0 = A_s/L$. R_c decays rapidly to zero when $W = W_0$ ($A_s = A_p$). However, in practice, $W \gg W_0$.

thickness and width decrease, R_{fc} decreases in both cases.

Equation (4.24) can be rewritten in another form to reflect the effect of fluid properties on the convective heat transfer coefficient h:

$$h = c_3\left(\rho Q C_p\right)^{\frac{1}{n}} (k')^{\frac{n-1}{n}} + c_4 k' \tag{4.25}$$

where c_3 and c_4 are two geometrical constants. Intuitive expectations can be extracted from (4.25): a higher fluid specific heat, flow rate, density, thermal conductivity and flow rate would increase the value of h.

In a recent 2014 paper from Smith et al. [74], correlations have been developed for laminar thermally developing flow in rectangular channels and parallel plates with uniform heat flux for all aspect ratios $\alpha = \frac{1}{\varepsilon} = \frac{W}{t'}$. It is exactly the type of channels we are trying to model, therefore the average Nusselt number correlation in [74] has been chosen for this work:

$$Nu = \left(Nu_{x^*\to 0}{}^N + Nu_{fd}{}^N\right)^{1/N} \tag{4.26}$$

$$Nu_{fd} = 8.235\left(1 - \frac{2.0421}{\alpha} + \frac{3.0853}{\alpha^2} - \frac{2.4765}{\alpha^3} + \frac{1.0578}{\alpha^4} - \frac{0.1861}{\alpha^5}\right) \tag{4.27}$$

$$Nu_{x^*\to 0} = 2.053\left(1 - \frac{1.016}{\alpha} + \frac{1.281}{\alpha^2} - \frac{0.5659}{\alpha^3}\right) x^{*m} \tag{4.28}$$

$$x^* = x/RePrD_h \tag{4.29}$$

$$m = -0.3302\left(1 + \frac{0.1083}{\alpha} - \frac{0.06569}{\alpha^2}\right) \tag{4.30}$$

$$N = 3.673\left(1 - \frac{0.3279}{\alpha} + \frac{0.2924}{\alpha^2}\right) \tag{4.31}$$

with x evaluated at half the channel length ($x = \frac{L}{2}$).

Fig. 4.5 shows the effect of t' and W on R_{fc}, the plots were obtained for $A_s = 6.22\ mm \times 6.22\ mm$ ($0.245\ inch \times 0.245\ inch$), $L = 3.556\ cm$ ($1.4\ inch$), $t = 50.8\ um$ ($2\ mil$), $k = 0.2\ W/(m.K)$, $Q = 150\ ml/min$, $W = 1.524\ cm$ ($0.6\ inch$) for Fig. 4.5 (a) and $t' = 762\ um$ ($30\ mil$) for Fig. 4.5 (b). The fluid used is DI water. Fig. 4.5 (a) shows that a 254 um (10 mil) channel is "thermally" better than a 762 um

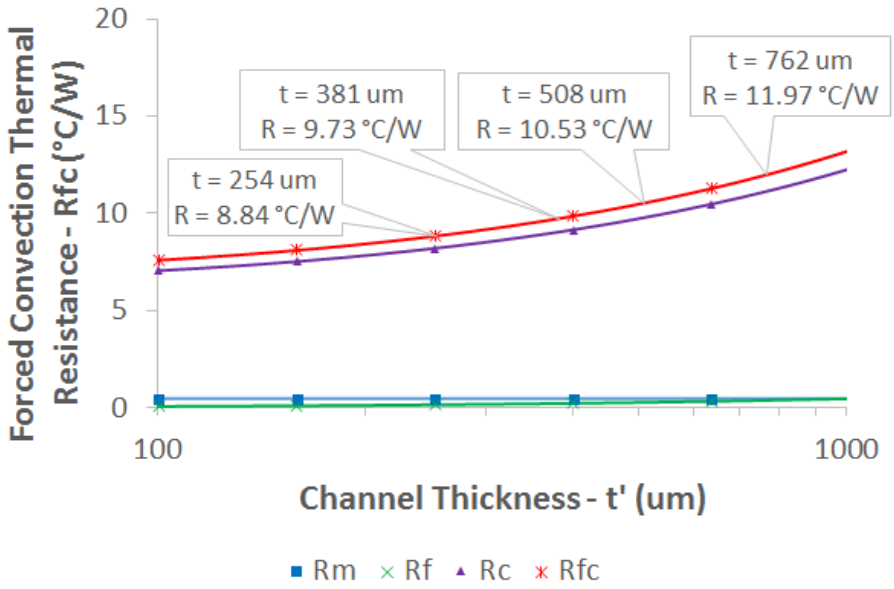

(a)

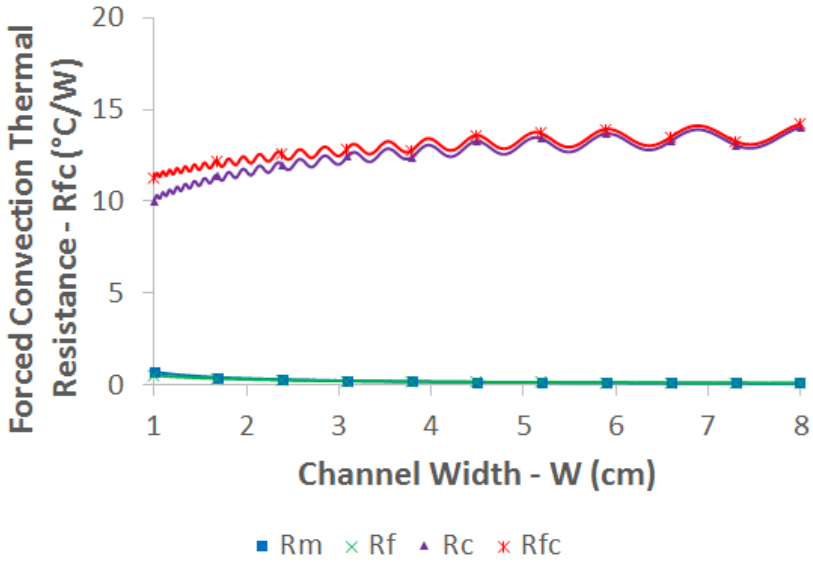

(b)

Fig. 4.5 Variation of the forced convection thermal resistance with a) channel thickness b) channel width.

(30 mil) channel. This trend can also be derived from the fact that h is inversely proportional to D_h in case Nu is taken as a constant. Therefore, a thinner channel would theoretically yield a better ”thermal” performance, but for good mechanical support of the heat source and, more importantly, for a reliable fluid circulation inside the microchannel, the channel thickness cannot be infinitely small. For fabrication purposes, it is recommneded to keep it above 254 um (10 mil).

4.1.3 Natural Convection

The natural convection coefficient calculation as well relies on Nusselt number correlations found in literature [75]. While forced convection uses the Reynolds number, natural convection, on the other hand, uses the Rayleigh number. Correlations depend on the surface geometry, on its orientation, on the fluid and on the flow type. In order to use correlations from literature, the heat source is assumed to behave like a 2D rectangular horizontal surface with laminar air flow. Laminar flow correlations for horizontal surfaces are generally of the form [75]:

$$Nu = CRa^n \tag{4.32}$$

where C and n are two constants.

The Nusselt number depends on the characteristic length L_C of the rectangular surface, which is given by:

$$L_C = \frac{A_s}{P} = \frac{S_x S_y}{2(S_x + S_y)} \tag{4.33}$$

where A_s and P are respectively the surface area and the perimeter of the surface. L_C is an increasing function of S_x and S_y and therefore increases with increased heat source size. If (4.32) is used to determine Nu, then the natural convective heat transfer coefficient h' can be written as:

$$h' = k'C\left(\frac{Prg\beta(T_s - T_{amb})}{\nu^2}\right)^n \times \frac{1}{L_C^{1-3n}} \tag{4.34}$$

k', β, ν and Pr values for air should be evaluated at the film temperature T_f:

$$T_f = \frac{T_s + T_{amb}}{2} \tag{4.35}$$

The natural convection thermal resistance R_{nc} is calculated over the heat source surface area A_s using the following equation:

$$R_{nc} = \frac{1}{h' A_s} \tag{4.36}$$

This thermal resistance decreases with increasing values of A_s and h'. For the best case scenario where A_s and h' are taking maximum values, R_{nc} can be evaluated to assess the influence of natural convection. For $A_s = 9.4\,mm\ x\ 9.4\,mm$ (maximum heat source size in this work) and $h' = 30\ W/(m^2.K)$ (typical maximum free convection value for air), $R_{nc} = 377.24\ °C/W$. This shows that natural convection, for this application, does not play a big role in heat dissipation compared to conduction or forced convection especially that R_{nc} will have a much bigger value for lower values of A_s and h'. The 3D thermal simulations also confirm that natural convection can be neglected.

4.1.4 Thermal Radiation

Thermal radiation calculations use Stefan-Boltzmann law for a grey body applied to our heat source with an emissivity ε, the radiated power can be calculated as:

$$P_{rad} = A_s \varepsilon \sigma (T_s^4 - T_{amb}^4) \tag{4.37}$$

To prove that thermal radiation can be neglected, P_{rad} is evaluated in the same way R_{nc} was evaluated in the last section where maximum values of A_s, T_s and ε are chosen. For $A_s = 9.4\,mm\ x\ 9.4\,mm$, $T_s = 150\ °C$ and $\varepsilon = 1$, $P_{rad} = 2.53\,mW$. If we consider, in average, that 10 W is dissipated when this heat source temperature reaches 150 °C, the radiated power constitutes only 0.025 % of the overall dissipated power.

This contribution is even lower when we consider smaller heat sources, lower junction temperatures and real emissivity values. Therefore thermal radiation can be neglected and will not be considered in the thermal model.

4.1.5 Contact Thermal Resistance

A thermal contact resistance $R_{contact}$ is present to account for the non-perfect surface contact at the device-heat sink interface. The thermal interface material (TIM) used in this work is a commercial thermal grease. Models for the contact resistance between two surfaces with a TIM layer in between have been investigated in the past [76-77]. Other models were also developed in [78] and [79] but they are difficult to use because the values for material hardness and microhardness are rarely reported in datasheets; that is also the case for the materials used in this work. For a first approximation, in case it is assumed that enough pressure is applied on the heat source, the contact thermal resistance can be estimated as follows:

$$R_{contact} \approx \frac{BLT}{k_{TIM} A_s} \tag{4.38}$$

where BLT is the bond line thickness, k_{TIM} is the thermal conductivity of the thermal grease and A_s is the heat source surface area. In general, the bond line thickness BLT is not a constant and depends on the applied pressure. However, for most thermal grease compounds, this value is often estimated to be around $50.8\ um\ (2\ mil)$ [80]. Based on that, it is assumed in this work that $BLT = 50.8\ um\ (2\ mil)$ and is not dependent on pressure.

4.1.6 Lumped Parameter Thermal Model

The final lumped thermal model reflects the fact that conduction and forced convection are the two predominant heat transfer mechanisms. Heat is generated at the junction level and goes through the case or body of the device with a thermal resistance R_{jc}. Heat is then conducted to the bottom Cu layer with a thermal resistance R_{hs} after

passing through the thermal grease layer with a contact thermal resistance $R_{contact}$. R_{hs} can either be equal to R_{multi} in the case of static water (no flow) or it can be equal to R_{fc} in the case of dynamic water (flow). The models and the 3D simulations all consider a 2D heat source and therefore R_{jc} is not taken into account in the model (the temperatures derived give immediately the junction temperature T_J), however, as far as the measurements are concerned, R_{jc} has to be added to the measured case-to-ambient temperature R_{ca} before any comparison can be made (T_J values cannot be directly measured). In (4.4), R_{multi} is evaluated at the center point $\left(\frac{L_x}{2}, \frac{L_y}{2}\right)$. The complete lumped thermal model proposed in this work is presented in Fig. 4.6. The heat sink thermal resistance R_{hs} and the junction-to-ambient thermal resistance R_{ja} are given by:

$$R_{hs} = \begin{cases} R_{multi}, & static\ case \\ R_{fc}, & dynamic\ case \end{cases} \tag{4.39}$$

$$R_{ja} = R_{hs} + R_{contact} + R_{jc} \tag{4.40}$$

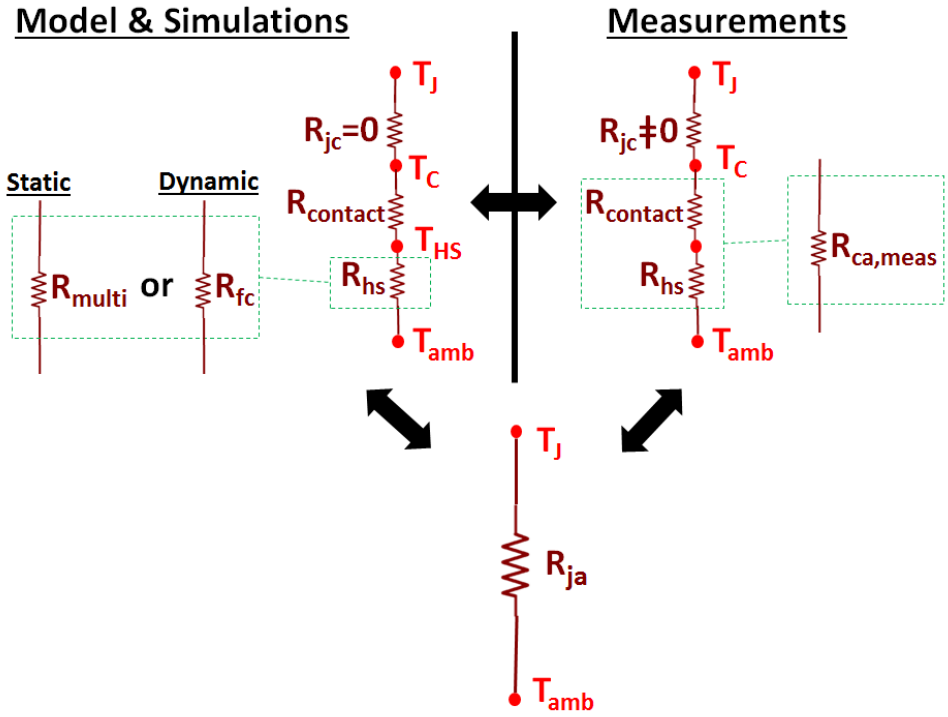

Fig. 4.6 Lumped thermal model for the microfluidic multilayer structure.

4.1.7 COMSOL 3D Model

A 3D electro-thermal model is created in COMSOL to simulate the temperature rise of the system for the static and the dynamic cases. The heat source is modeled as a 2D heat source sheet above a 50.8 um (2 mil) layer of thermal grease. For a constant dissipated power, the steady-state maximum junction temperature is obtained, that value is then used to derive the simulated junction-to-ambient thermal resistance. Fig. 4.7 shows the simulation results of a 9.4 mm x 9.4 mm heat source on a 254 um (10 mil) microchannel for the dynamic case (Fig. 4.7 (a)) and the static case (Fig. 4.7 (b)). The parameters that can be changed in the simulation are the heat source area, the microchannel thickness and the type of flow.

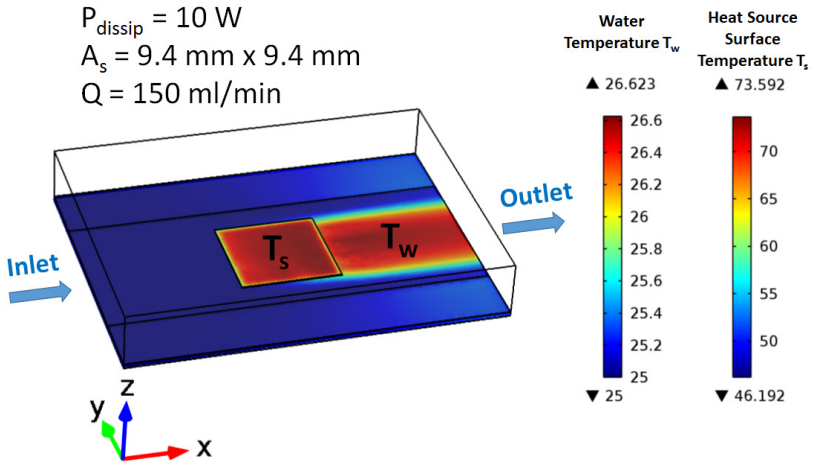

(a)

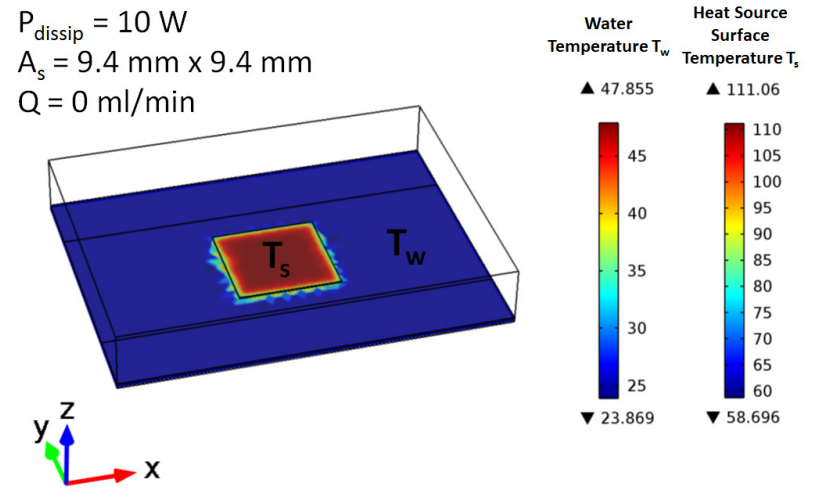

(b)

Fig. 4.7 COMSOL 3D model for a) dynamic case b) static case.

4.2 Heat Sources Specifications

Two high power surface mount thin film resistors with different maximum power ratings are used as heat sources (Fig. 4.8). The heat sink role is to provide a sufficient heat removal rate so that the resistor junction temperature T_J stays always below its maximal specified value $T_{J_{max}}$. If the heat sink thermal resistance is not small enough, then the resistor dissipated power starts to derate with a slope of $1/R_{jc}$. R_{jc} is calculated using the following equation:

$$R_{jc} = \frac{T_{J_{max}} - T_C}{P_{max}} \tag{4.41}$$

To operate the resistors at their full power ratings at room temperature ($T_{amb} = 25\ °C$), the junction-to-ambient thermal resistance should not exceed a maximum value $R_{ja_{max}}$ which is given by:

$$R_{ja_{max}} = \frac{T_{J_{max}} - T_{amb}}{P_{max}} \tag{4.42}$$

Table 4.5 summarizes the resistors dimensions and thermal properties while Fig. 4.9 shows the power derating curves of the resistors based on the manufacturer's datasheets.

TABLE 4.5
SURFACE MOUNT RESISTORS SPECIFICATIONS

Resistor No.	Length (mm)	Width (mm)	P_{max} (W) @ T_C (°C)	T_{Jmax} (°C)	R_{jc} (°C/W)	$R_{ja\ max}$ (°C/W)
1	9.53	6.35	30 @ 100	150	1.67	4.17
2	9.40	9.40	40 @ 100	150	1.25	3.13

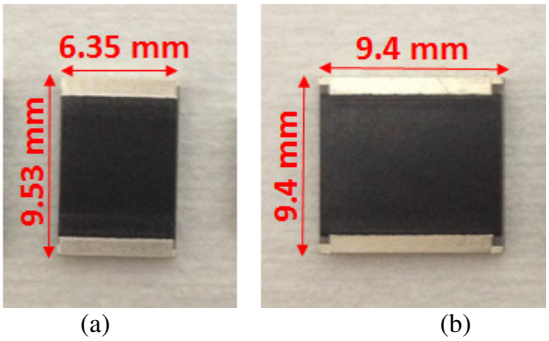

(a) (b)

Fig. 4.8 Top view pictures of the high power resistors a) 30 W b) 40 W.

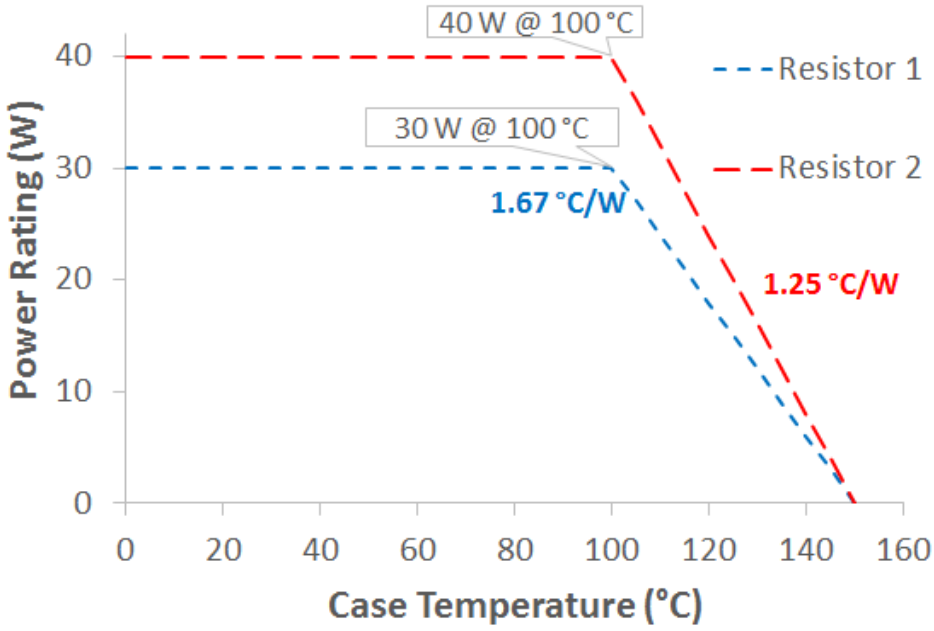

Fig. 4.9 Resistors power derating curves.

4.3 Fabrication Procedure

The fabrication of the microchannel structure shown in Fig. 4.10 starts with a 15.24 cm x 15.24 cm (6 inch x 6 inch) double copper clad RO3003 panel. Copper is etched out from both sides of the panel and 3.556 cm x 1.524 cm (1.4 inch x 0.6 inch) cavities are ablated on it. The panels used for this work have thicknesses of 254 um (10 mil), 381 um (15 mil), 508 um (20 mil) and 762 um (30 mil) respectively and are sandwiched between two bondplies with a thickness of 25.4 um (1 mil) each. The same cavities are ablated on the bondplies but are 3 mm larger from each side to give room for bondplies to expand after they melt. A 15.24 cm x 15.24 cm (6 inch x 6 inch) double copper clad ULTRALAM 3850 panel, with a thickness of 50.8 um (2 mil), serves as

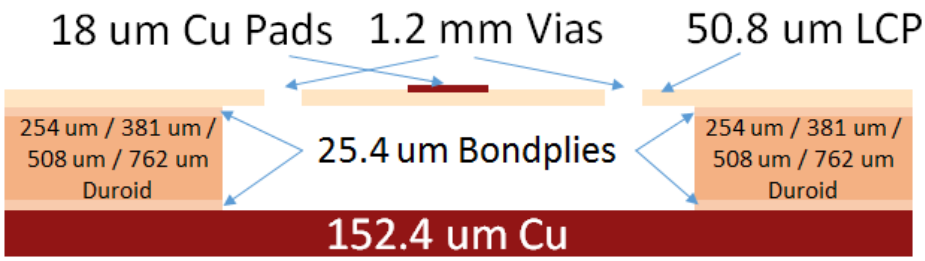

Fig. 4.10 Cross section of the laminated multilayer stack-up.

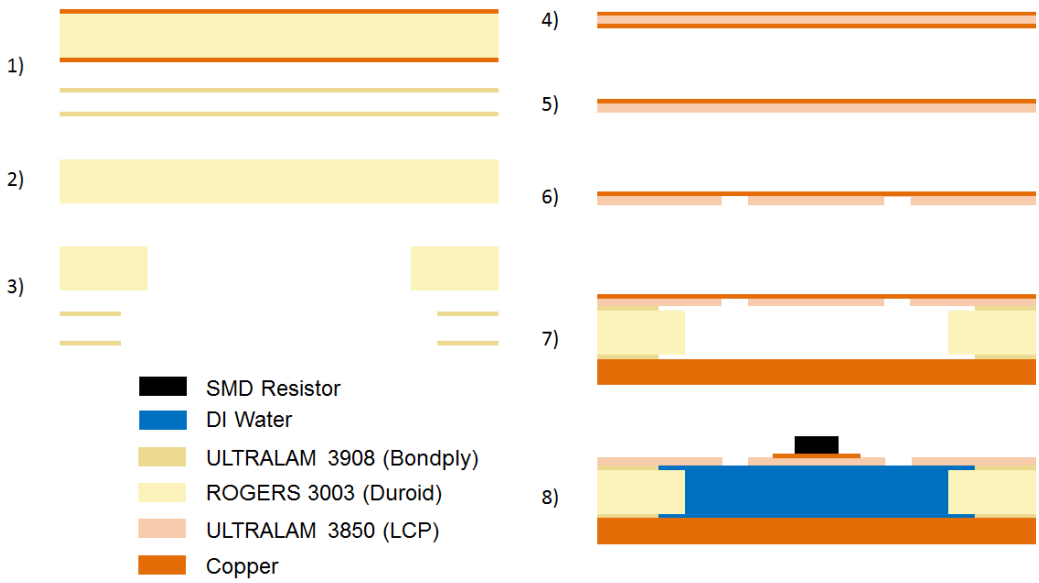

Fig. 4.11 Package fabrication flow. 1) Double clad Duroid + 2 bondplies 2) Copper etching from both sides of Duroid 3) Cavity ablating on Duroid and bondplies 4) Double cladded LCP 5) Copper etching from one side of LCP 6) Via drilling 7) Lamination 8) Final micromachined structure.

the microchannel top capping layer. Copper is etched out from one side of the LCP panel and vias, with a diameter of 1.2 mm, are drilled on it using a CO_2 laser. The vias are used as injection points for the liquid. A 15.24 cm x 15.24 cm (6 inch x 6 inch) copper shim, with a thickness of 152.4 um (6 mil), is used as the bottom capping layer. The whole stack-up is laminated to form solid bonds between the different layers using a thermal press. The temperature and force for lamination were 285 °C and 48 kN (5.4 tf) respectively. A detailed fabrication flow is illustrated in Fig. 4.11.

Copper at the top is patterned using standard lithographic and wet etching processes to create biasing pads for the resistors and to open up the vias. Microchannels are cut individually, the size of a single structure is 4.5 cm x 2.7 cm (1.77 inch x 1.06 inch). A top view of the aligned layers (without the Cu ground) before the lamination step is presented in Fig. 4.12 (a), while the fully laminated and patterned sample is presented in Fig. 4.12 (b). It can be seen that this process allows large panel processing with the creation of 15 microchannels in one fabrication cycle. One disassembled sample is shown in Fig. 4.13 along with a text description of the different layers.

(a) (b)

Fig. 4.12 5 x 3 samples a) bottom view (before lamination) b) top view (after lamination).

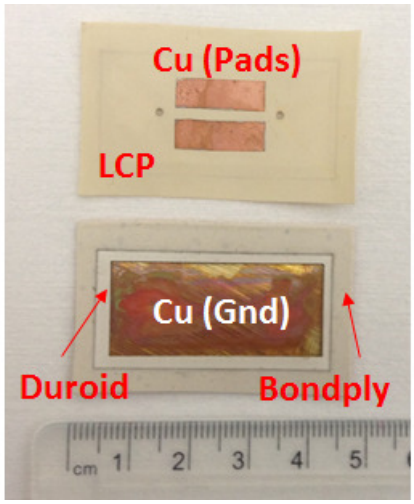

Fig. 4.13 Disassembled microfluidic channel.

After the lamination step, it is important to test the quality of the fabricated channels because, most of the time, the top LCP layer sticks to the bottom ground after being subject to high pressure levels. A long sharp needle or a long syringe can be used to detach the bottom copper from LCP. A liquid flow test is then performed with a syringe to make sure that the channel has been opened up correctly, this is done by injecting the liquid from one via and monitoring if the liquid comes out from the second via. This step is essential and is done before attaching any tubes so that any flaws in the sample can be detected up front. Two flexible silicone tubes, with a diameter of 2.4 mm each, are attached to the vias using a commercial plastic epoxy. Liquid circulation is tested using a micropump, this step allows the detection of any leaks or cracks in the

(a) (b)

Fig. 4.14 Resistors on microfluidic channels. a) 30 W resistor b) 40 W resistor.

sample; a thing that could happen due to a high flow rate of the liquid inside the microchannel. A small layer of thermal grease is deposited on top of the LCP before soldering the resistors, the thermal grease thermal conductivity reported by the manufacturer is $k_{TIM} = 0.95\ W/(m.K)$. It is important to put enough pressure on the resistors during the soldering phase in order to minimize the bond line thickness. Wires for biasing the resistors are soldered on the pads. Fig. 4.14 shows pictures of the resistors mounted on the microfluidic channels.

4.4 Measurements and Results

4.4.1 Test Bench Description

The temperature of the high power resistors is measured using a K-type thermocouple, with a diameter of 80 um (40 AWG), placed at the center of the resistor and secured with a small piece of Kapton tape. The use of thermocouples for thermal characterization measurements is a commonly used technique in industry provided that the wire gauge is small (36 AWG or higher which corresponds to a diameter of 127 um or lower) [81]. A fine gauge thermocouple reduces the heat sinking effect generated by the contact of the thermocouple leads with the device under test [82]. The different samples sit on a 2 mm (0.079 inch) thick metal chuck at room temperature. A micropump is used to ensure a closed loop flow of the fluid inside the microchannel at

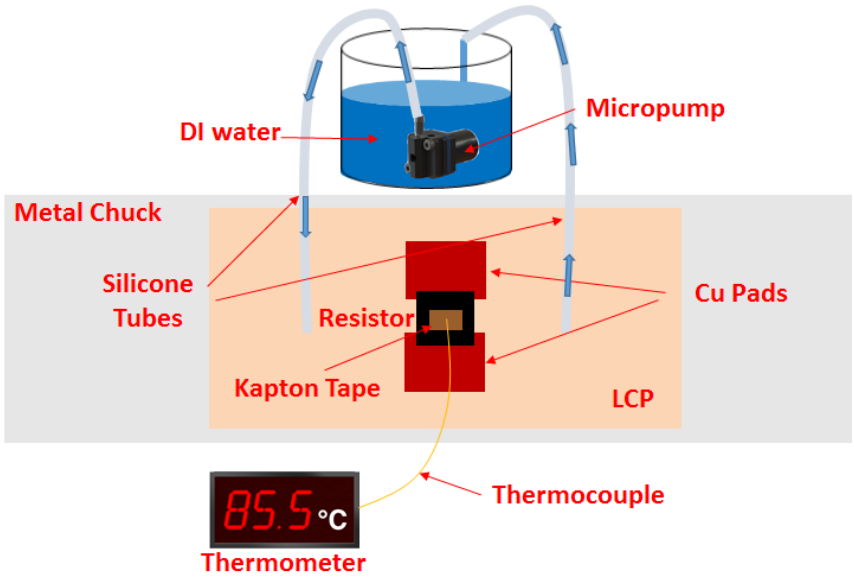

(a)

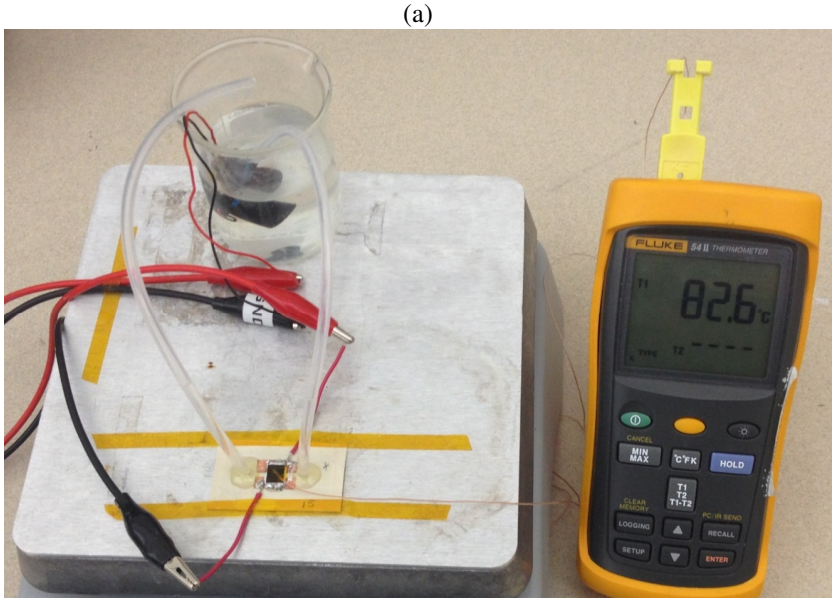

(b)

Fig. 4.15 a) Temperature measurement test bench b) Picture of the measurement setup.

a rate of 150 ml/min. Fig. 4.15 (a) is an illustration of the measurement setup and Fig. 4.15 (b) is a picture of the actual setup.

Based on (4.24), the microchannel thickness should be small to enhance the convection heat transfer. For this reason, thicknesses from 254 um (10 mil) to 762 um (30 mil) were chosen so that ε is small (ε ranging from 1.67 % to 5 %). The thickness should not be chosen below 254 um (10 mil) to ensure reliable fluid flow inside the channel and adequate mechanical support.

TABLE 4.6
FIGURES OF MERIT FOR LIQUID COOLANTS

	Water	DI Water	EG+H_2O	FC-43
Compatible with Copper	++	--	++	++
High Thermal Conductivity	++	++	+	--
High Heat Capacity	++	++	+	-
Low Viscosity	++	++	+	--
Low Freezing Point	-	-	+	++
High Boiling Point	-	-	+	++
Low Flash Point	++ *	++ *	-	++ *
Low Corrosivity	-	--	++	+
Low Toxicity	++	++	-	-
High Thermal Stability	++	++	++	++
Good Electrical Insulation	--	-	+	++
Low Cost	++	+	-	--

++ Excellent + Good - Poor -- Bad
*Not flammable

The most commonly used fluids for cooling are water, DI water, a mixture of DI water and ethylene glycol (EG) and finally dielectric fluids such as FC-43. Table 4.6 is a comparative table between these coolants. DI water has the best thermal conductivity amongst liquids (0.6 W/(m.K)) and is only second best to mercury (8.69 W/(m.K)); it also has the highest specific heat value (4180 J/(kg.K)). It has already been shown in (4.25) that these two parameters are key to improving the forced convective heat transfer coefficient. DI water has also a low viscosity, a high thermal stability and is non-toxic. For all these excellent properties that DI water is chosen in this work.

4.4.2 Results and Discussion

The measurement setup described in the previous section is used to measure the temperature values of the different resistors for different flow configurations. In order to determine the case-to-ambient thermal resistances, power sweeps are performed on the resistors from 0 W to power levels that correspond to the maximum case temperature tolerated by the devices with temperature data being recorded for each single power point. The slope of the case temperature T_C as a function of the dissipated power P yields the measured case-to-ambient thermal resistance $R_{ca_{meas}}$. The junction-to-case thermal resistance R_{jc} has to be added to $R_{ca_{meas}}$ to calculate the

measured junction-to-ambient thermal resistance $R_{ja_{meas}}$. $R_{ja_{meas}}$ is then compared to the modeled and simulated case-to-ambient thermal resistance ($R_{ja_{model}}$ and $R_{ja_{simu}}$). The values of h are determined using the following thermal properties of DI water at 25 °C: $\mu = 0.891.10^{-3}\ Pa.s$, $C_p = 4180\ J/(kg.K)$ and $\rho = 997.13\ kg/m^3$. The measured junction-to-ambient thermal resistance is plotted versus the channel thickness in Fig. 4.16 for the static and dynamic cases and is compared to the values extracted from the model and the simulation. A detailed summary of modeled, simulated and measured results can be found in Table 4.7.

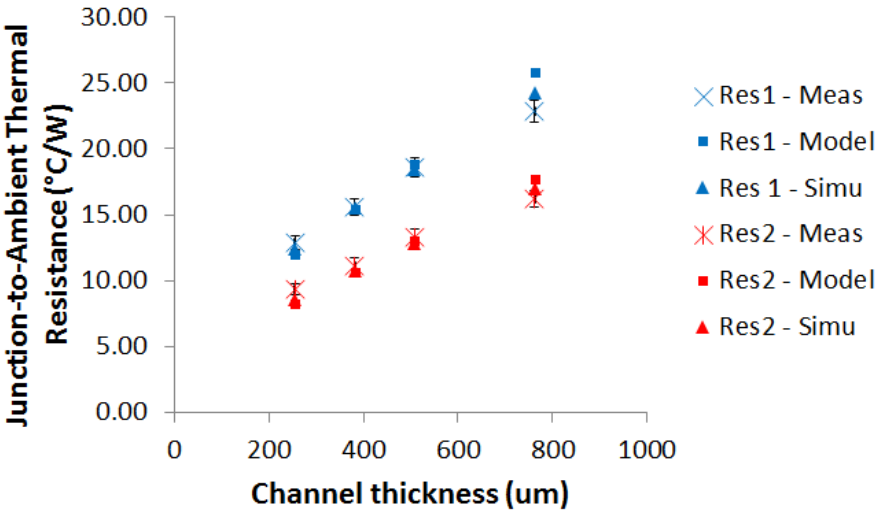

(a)

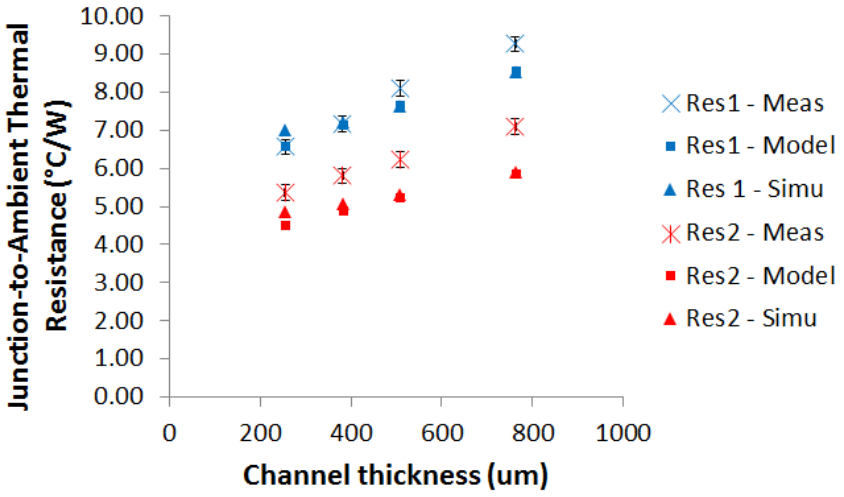

(b)

Fig. 4.16 Junction-to-ambient thermal resistance comparison between measured data, model and simulation for a) static water b) dynamic water.

TABLE 4.7
MODEL VS SIMULATIONS VS MEASUREMENTS

Channel Thickness (um/mil)			254/10		381/15		508/20		762/30	
Flow Type [a]			S	D	S	D	S	D	S	D
Model	R_{multi} (°C/W)	Res. 1	11.08	-	14.55	-	18.01	-	24.90	-
		Res. 2	7.64	-	10.01	-	12.38	-	17.12	-
	R_{fc} (°C/W)	Res. 1	-	5.70	-	6.27	-	6.78	-	7.70
		Res. 2	-	3.90	-	4.29	-	4.64	-	5.27
	$R_{contact}$ (°C/W)	Res. 1	0.88		0.88		0.88		0.88	
		Res. 2	0.61		0.61		0.61		0.61	
	R_{ja} (°C/W)	**Res. 1**	**11.97**	**6.59**	**15.43**	**7.15**	**18.89**	**7.67**	**25.79**	**8.59**
		Res. 2	**8.24**	**4.50**	**10.61**	**4.89**	**12.98**	**5.24**	**17.73**	**5.87**
Simulation	**R_{ja} (°C/W)**	**Res. 1**	**12.43**	**7.01**	**15.52**	**7.22**	**18.46**	**7.62**	**24.28**	**8.54**
		Res. 2	**8.61**	**4.86**	**10.75**	**5.08**	**12.83**	**5.32**	**16.95**	**5.91**
Measurements	**R_{ja} (°C/W)**	**Res. 1**	**12.90**	**6.57**	**15.57**	**7.17**	**18.60**	**8.10**	**22.83**	**9.27**
		Res. 2	**9.38**	**5.38**	**11.10**	**5.80**	**13.34**	**6.23**	**16.20**	**7.09**
Relative Error (%)		**Res. 1**	**7.23**	**0.28**	**0.88**	**0.20**	**1.56**	**5.37**	**12.93**	**7.35**
		Res. 2	**12.08**	**16.22**	**4.38**	**15.66**	**2.66**	**15.84**	**9.41**	**17.16**

[a] S: Static, D: Dynamic

It can be seen from Fig. 4.16 and the highlighted last four blocks in Table 4.7 that there is a good match between the model and the simulation. The model and the simulation are in good agreement with the measurements as well. The relative error between the model values and measured data is given by:

$$Relative\ Error\ (\%) = \frac{\left|R_{ja_{meas}} - R_{ja_{model}}\right|}{R_{ja_{meas}}} \times 100 \tag{4.43}$$

The maximum relative error is about 17.16 % for resistor 1 on the 762 um (30 mil) microchannel while the average cumulative error for all the data is about 8.08 %. The other information that can be extracted from the data is the maximum absolute power rating P_{max} of the resistors when they are mounted on different heat sink configurations with or without DI water flow. For that, the following equation is used:

$$P_{max} = \frac{T_{J_{max}} - T_{amb}}{R_{ja}} \tag{4.44}$$

Table 4.8 summarizes the maximum power ratings and the maximum power densities of the resistors in the static and dynamic cases. The data indicates that the microfluidic solution presented in this work allows the resistors to operate at higher power levels, e.g. a net power difference of 10 W is observed for the 40 W resistor on top of a 254 um (10 mil) microchannel. Back to (4.42), the measured junction-to-ambient thermal

TABLE 4.8
RESISTORS MAXIMUM POWER RATINGS FOR STATIC AND DYNAMIC DI WATER AT 25 °C

Channel Thickness (um/mil)		254/10		381/15		508/20		762/30	
Flow Type [a]		S	D	S	D	S	D	S	D
P_{max} @ 25°C (W)	Res. 1	9.69	19.04	8.03	17.44	6.72	15.43	5.47	13.49
	Res. 2	13.33	23.26	11.26	21.55	9.37	20.06	7.72	17.63
Max. Power Density @ 25°C (W/cm^2)	Res. 1	16.01	31.46	13.27	28.82	11.11	25.50	9.05	22.29
	Res. 2	15.09	26.32	12.74	24.39	10.60	22.71	8.73	19.95

[a] S: Static, D: Dynamic

resistances are higher than $R_{ja_{max}}$ values reported in Table 4.5 which explains why the resistors could not be operated at their full power rating specified by the datasheet.

Measured data shows that the microfluidic heat sink is more efficient when the size of the heat source is bigger. Overall, thermal heat transfer by conduction remains inefficient because of the poor thermal conductivity of LCP, however, conduction becomes more influential for bigger devices. This is mainly due to the fact that the constriction resistance is always decreasing when the heat source size is increasing and decays rapidly to zero when the heat source size is converging towards the sample size. Therefore, this study shows that this kind of microfluidic cooling solution can be used to cool heat sources with large surface areas efficiently, for smaller devices there could be other solutions like reducing the thickness of the LCP layer and/or to add a thin layer of high thermal conductivity material on top of the LCP layer.

Measurements also confirm the theoretical results developed in Section 4.1 with regards to the channel thickness effect on the overall thermal resistance of the system: as the channel thickness decreases, the junction-to-ambient thermal resistance decreases as well for both the static and the dynamic case studies. Qualitatively, this can be explained by the fact that water, even though being the best choice amongst liquids, still has a low thermal conductivity compared to good solid conductors like

copper. Minimizing that layer of water helps conduct heat more efficiently. This variation can be approximately quantified as follows:

$$\delta \approx \begin{cases} \frac{3}{25.4}\%/um\ (3\ \%/mil),\ static\ fluid \\ \frac{1.5}{25.4}\%/um\ (1.5\ \%/mil), dynamic\ fluid \end{cases} \tag{4.45}$$

$$\frac{\Delta R_{ja}}{R_{ja}} = \frac{-\Delta P_{max}}{P_{max}} = \delta \Delta t' \tag{4.46}$$

where δ is the experimental percentage change per unit length, ΔR_{ja} is the junction-to-ambient thermal resistance change, ΔP_{max} is the maximum power rating change and $\Delta t'$ is the microchannel thickness change.

4.4.3 Design Guidelines

Based on the results of this study, the following are general guidelines for designing multilayer organic microchannels for cooling purposes with a low thermal resistance:

- Microchannel length ($\boldsymbol{L}$) and width ($\boldsymbol{W}$): L and W have minimal effect on the thermal resistance, yet lower values of L and W yield a slightly lower thermal resistance.
- Microchannel thickness ($\boldsymbol{t'}$): t' is an important factor and should be minimized. Equations (4.45) and (4.46) give a mean to quantify the change in the thermal resistance and the maximum power rating, i.e. 3 % or 1.5 % change is expected per 25.4 um (1 mil) variation in $\boldsymbol{t'}$. t' should not be too small (preferably not below 254 um (10 mil)) to ensure reliable fluid flow.
- Sample surface area ($\boldsymbol{A}$): a bigger sample helps conduct heat more efficiently, this can be clearly observed in (4.4) with the term "$\frac{1}{L_x L_y}$". There is clearly a tradeoff here between the system compactness and the system thermal resistance.
- LCP thickness ($\boldsymbol{t}$): the thickness of LCP is an important factor and should be minimized because LCP has a very low thermal conductivity. This is not a general

rule though, the thickness should be increased in the case of a high thermal conductivity material. Values extracted from (4.4) and (4.18) support this claim. t should not be too small (preferably not below 50.8 um (2 mil)) to ensure a good mechanical support of the heat source.

- Copper thickness: varying this parameter has almost no effect because it is not the limiting factor in the system. Smaller values would keep the sample highly flexible which makes it easy to test the fluid flow in the fabrication/assembly phase.
- Fluid: for pure thermal considerations, DI water would be the best choice based on the properties discussed in Section 4.4.1 and on Table 4.6.

4.4.4 Limitations

4.4.4.1 Fabrication & Measurement Limitations

- Fabrication, packaging, assembly and test were done manually, so repeatability and reliability could be an issue with this kind of microfluidic solution. For example, some channels are very good and allow very smooth circulation of the fluid inside, some may not be as good.
- There could be differences in the contact thermal resistances across the different samples due to applying different pressure levels during the soldering process, or using different amounts of thermal grease.
- LCP is a flexible material which induces a non-flat surface at the top especially if the thickness of LCP is small. This could alter the quality of contact between the LCP and the heat source.
- The measurement procedure involved the use of a thermocouple. Even though it is recommended to reduce the wire gauge to reduce the parasitic effect introduced by the leads of the thermocouple, there is still an error introduced by the test equipment

which conducts some of the generated heat. Also the temperature readings are very sensitive to the positioning of the thermocouple on the heat source.

- The metal chuck on top of which the samples are sitting also contribute to heat dissipation.
- Additional errors can come from the differences that exist between same heat sources due to manufacturing variance.

4.4.4.2 Model Limitations

- This model can accurately predict the thermal resistance of the system for large heat source areas. Although the model and the simulation agree even for smaller devices, it has been noticed, through other measurements of smaller resistors (6.22 mm x 6.22 mm and lower), that the model and simulation start diverging significantly from the model, the model could be improved to be valid for all heat source sizes.
- All the parameters that are taken from datasheets are subject to uncertainty errors. These parameters can be thermal conductivities, thicknesses, resistors junction-to-case thermal resistances, resistors sizes…
- The contact thermal resistance is difficult to model accurately for this complex structure. More accurate models involving thermal greases are needed in this case.
- Errors are introduced when DI water and Duroid are replaced by one uniform layer with a fixed thermal conductivity. This assumption was acceptable because the thermal conductivities of the two materials are close. This assumption cannot be used if another material was used instead of Duroid.
- DI water thermal properties change with temperature. The model, in the other hand, calculates the forced convective heat transfer coefficient using the thermal properties of DI water at a fixed temperature.

- The model and the simulations assume that the heat source is a 2D sheet dissipating a constant power over its whole surface area.

4.5 Summary

A microfluidic cooling solution on multilayer organic substrate with dynamic DI water flow has been presented for cooling high power surface mount resistors. A general thermal model has been detailed along with all the necessary theoretical assumptions and formulations. Different heat transfer mechanisms and their influence have been discussed with an emphasis on the effect of geometrical dimensions of the microchannel on the overall cooling efficiency. The model has also been validated using a 3D electro-thermal model in COMSOL. Microchannels fabrication procedure has been described in detail along with the measurement test bench. The modeled and simulated data agreed well with the measurements when heat sources with large sizes were used, the model fails for smaller heat source sizes. Measurements have also proven that this microfluidic solution on LCP could increase the maximum dissipated power of resistors; a maximum net power difference of 10 W at 25°C was achieved with dynamic water flow for the 40 W resistor sitting on top of the 254 um (10 mil) microchannel. It was also discussed that this microfluidic cooling solution is more efficient when heat sources have a bigger surface area. Moreover, an approximate experimental percentage change was developed to predict the effect of varying the microchannel thickness. Guidelines on how to design multilayer organic microchannels with low thermal resistance were also provided. Finally, limitations and approximation errors that could be originating from fabrication, from the measurement setup and/or from the model were discussed as well.

PART II

INTEGRATED MICROFLUIDIC TUNING ON MULTILAYER ORGANIC SUBSTRATE

"Science investigates; religion interprets.
Science gives man knowledge which is power;
religion gives man wisdom which is control."
-Martin Luther King, Jr

Reconfigurable RF circuits can be very important in some cases where there is a need to minimize the size of the overall system while being able to target multi-band applications at the same time. In the wireless transmission chain, these multi-band applications usually involve the use of RF resonators/filters and RF PAs. As discussed in Chapter 1, there are many techniques available to achieve the desired re-configurability, and amongst these techniques is the use of microfluidic channels. This kind of approach is suitable for RF microstrip circuits in general, and it is applied in this work for specific RF circuits to prove the concept. By changing the fluids inside the microchannel, the electrical response of the microstrip RF circuit on top of it changes. For an RF filter, this change can translate into a frequency shift of the resonance and/or the alteration of the fractional bandwidth whereas for an RF PA, this change can result in shifting the frequency of operation of the PA while minimizing any degradation in the electrical performance. In this part, RF bandpass filters and RF PAs are tuned using an integrated microfluidic solution on multilayer organic substrates.

CHAPTER 5

MICROFLUIDICALLY RECONFIGURABLE L-BAND MICROSTRIP BANDPASS FILTER ON MULTILAYER ORGANIC SUBSTRATE

Reconfigurable RF bandpass filters are types of filters where the center frequency and/or the bandwidth are tuned. Below are the results of investigating the usage of a microfluidic solution on organics to tune an L-band microstrip bandpass filter.

5.1 Tunable Filter Design

5.1.1 Effective Dielectric Constant

The microstrip filter is designed on top of an LCP layer and a channel initially filled with DI water, the stack-up is illustrated in Fig. 5.1. It is important to estimate the "effective" dielectric constant of this two layer structure. A first estimation is given by [83]:

$$\varepsilon_{r_{eff}} = \frac{\varepsilon_{r_1}\varepsilon_{r_2}(h_1 + h_2)}{\varepsilon_{r_1}h_2 + \varepsilon_{r_2}h_1} \tag{5.1}$$

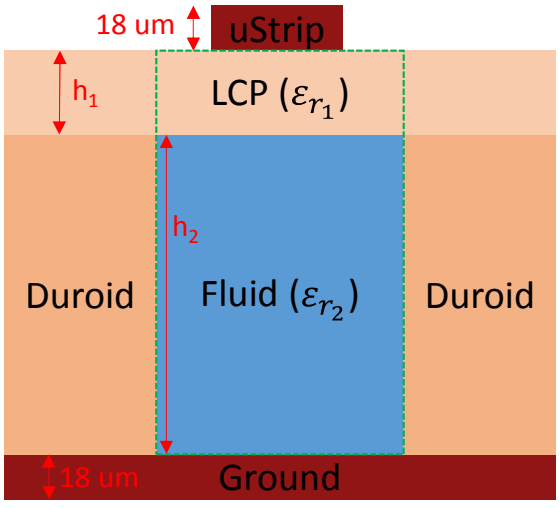

Fig. 5.1 2D cross section of the multilayer structure.

where ε_{r_1} and ε_{r_2} are the dielectric constants of the LCP layer and the fluid respectively, and h_1 and h_2 are their respective thicknesses.

LCP has a stable dielectric constant $\varepsilon_{r_1} = 2.9$ and a low loss tangent $tan\delta_1 = 0.0025$ in the frequency band of interest (from 100 MHz to 2 GHz). However, the dielectric constant and loss tangent of DI water depend on frequency and temperature. To account for this dependency the Debye model [84], with three relaxation terms and two resonance terms, is used (Fig. 5.2). Values are averaged and used as a good first approximation: $\varepsilon_{r_2} = 80$ and $tan\delta_2 = 0.06$ at 20°C.

It is important to state that (5.1) is only an approximation that is most of the time very inaccurate. A more accurate modeling approach is discussed in detail in Chapter 7. That is why, a correction factor has been introduced in this work to the formula in (4.1) to re-center the filter response:

$$\varepsilon_{r_{eff}}(\varepsilon_{r_1}, h_1, \varepsilon_{r_2}, h_2) = 0.67 \times \frac{\varepsilon_{r_1}\varepsilon_{r_2}(h_1 + h_2)}{\varepsilon_{r_1}h_2 + \varepsilon_{r_2}h_1} \tag{5.2}$$

Equation (5.2) is only valid within the scope of this design, and because (5.2) is based on an approximation, the simulated and measured filter bandwidth is slightly smaller than what was originally designed.

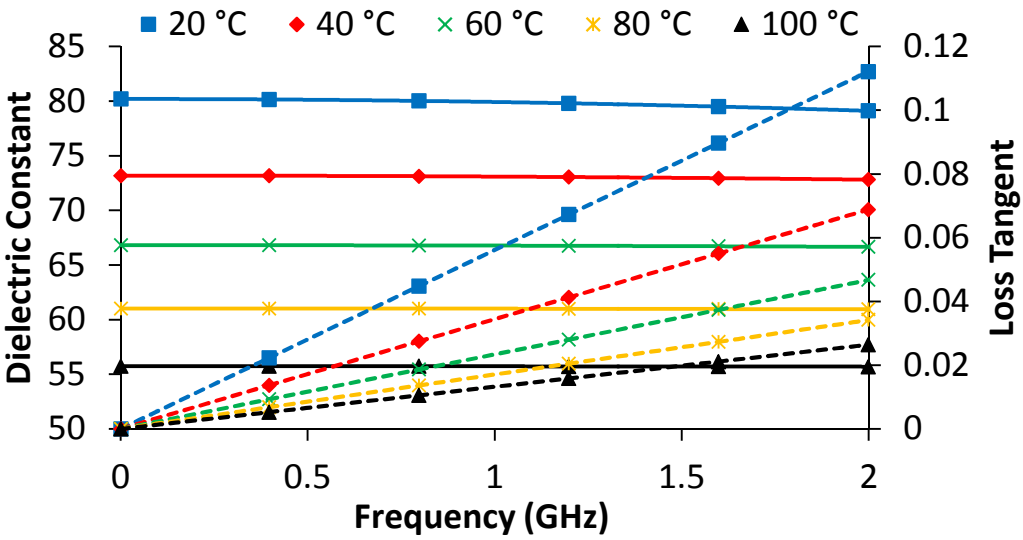

Fig. 5.2 Variation of the dielectric constant (solid lines) and loss tangent (dashed lines) of water with frequency and temperature.

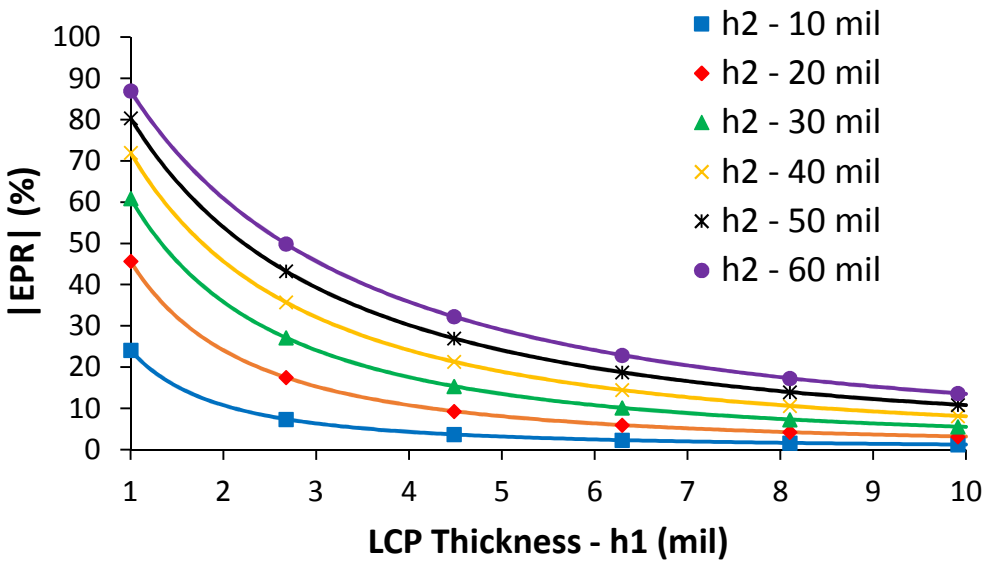

Fig. 5.3 Absolute value of the EPR with ε_{r_2} ranging from 20 to 80 at 25°C.

Given a two layer structure in which the dielectric constant of the second layer can be changed from a minimum value $\varepsilon_{r_2\,min}$ to a maximum value $\varepsilon_{r_2\,max}$, we define, in this paper, the effective permittivity range (EPR) as:

$$EPR = \frac{\varepsilon_{r_{eff}}\left(\varepsilon_{r_1}, h_1, \varepsilon_{r_2\,min}, h_2\right) - \varepsilon_{r_{eff}}\left(\varepsilon_{r_1}, h_1, \varepsilon_{r_2\,max}, h_2\right)}{\varepsilon_{r_{eff}}\left(\varepsilon_{r_1}, h_1, \varepsilon_{r_2\,max}, h_2\right)} \tag{5.3}$$

The pair (h_1, h_2) is chosen to maximize EPR. It can be seen from Fig. 5.3 that the best choice for (h_1, h_2) is when h_2 is very large and h_1 is very small. The value chosen for h_1 is 2 mil. A thickness of 1 mil is too thin for adequate mechanical support and reliability. The value of h_2 is set to 60 mil. With these values, $EPR \approx -60\%$. This number means that in case we replace DI water ($\varepsilon_{r_2\,max} = 80$) with acetone ($\varepsilon_{r_2\,min} = 20.7$), the effective dielectric constant of the structure would drop by 60%. Using this drop in the effective dielectric constant, the filter response can be tuned.

5.1.2 Filter Topology

The filter topology and the design equations can be found in [85]. A 3rd order filter using Butterworth coefficients centered at 1 GHz and with a 3 dB fractional

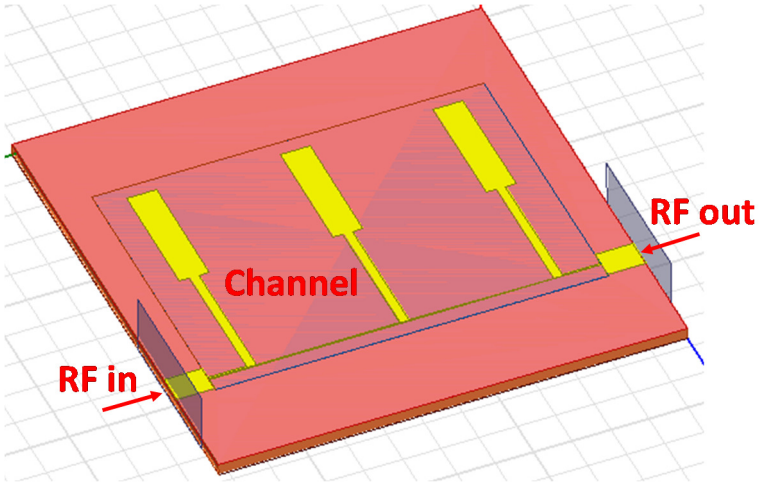

Fig. 5.4 Microstrip filter 3D model in HFSS.

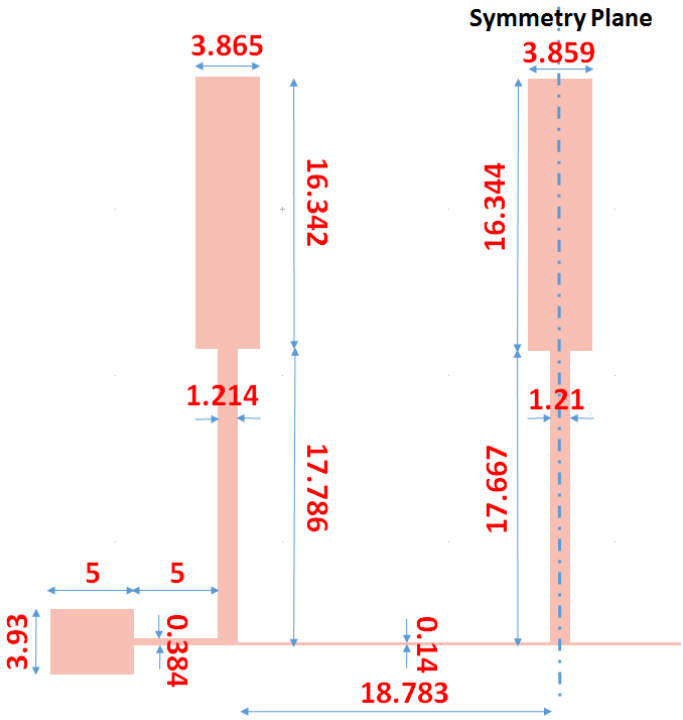

Fig. 5.5 Filter layout in ADS with dimensions in mm.

bandwidth (FBW) of 40% has been designed using inverter lines and parallel open stubs. The design was simulated in ADS with LCP and DI water layers ($\varepsilon_{r_{eff}} = 28.88$) and a 3D model was created and simulated in HFSS (Fig. 5.4). The different dimensions are reported in Fig. 5.5. The size of the filter without including the channel is 6.1 cm x 3.6 cm.

5.2 Fabrication Procedure

The fabrication starts with two 30 mil double copper clad RO3003 panels with a size of 8 inch x 6 inch each. Copper is etched out from both sides of RO3003. Cavities with dimensions of 4 cm x 5.1 cm are ablated on the two sheets using a CO_2 laser. The copper on a 2 mil LCP panel is etched from one side and vias with a diameter of 1.2 mm are drilled through the substrate. The vias serve as access points for fluid injection. Three bond plies, with a thickness of 1 mil each, are interposed between each of the layers and the whole stack-up is laminated along with a 6 mil thick copper shim. The top side of 2 mil LCP is then patterned to create the microstrip lines using standard photolithography process. A cross sectional view of the stack-up is shown in Fig. 5.6. With this process, 8 filters can be created in one fabrication cycle, each filter is cut individually and SMA connectors are soldered to each one of them. Fig. 5.7 (a) shows the layers stacked-up before lamination and Fig. 5.7 (b) is a picture of the fabricated filter.

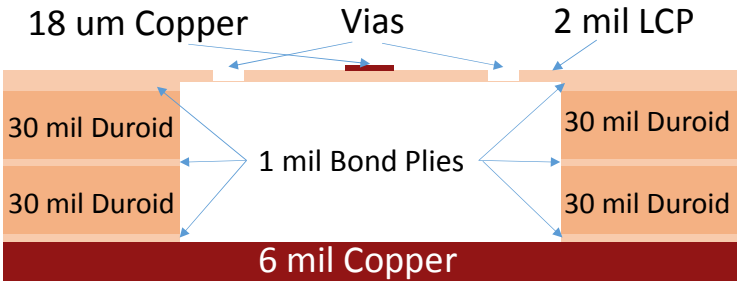

Fig. 5.6 Cross section of the multilayer structure.

(a) (b)

Fig. 5.7 a) Layers stack-up before lamination b) Fabricated tunable filter.

5.3 Measurements and Results

A 2.4 mm tube, as shown in Fig. 5.7 (b), is attached to one of the vias for fluid injection while the other via is sealed with a piece of tape. A micropump is used to inject the fluids, it provides the necessary pressure to trap the fluid inside the channel. Fluids used are DI water and acetone and the response of the filter is measured for both cases. Fig. 5.8 shows the measurement setup while Fig. 5.9 compares simulated and measured S-Parameters.

The measured results agree with the simulated results for DI water and acetone. 50% tuning is achieved with good insertion and return loss. Table 5.1 is a comparison of the two filters.

TABLE 5.1
DI WATER FILTER VS ACETONE FILTER

	DI water	Acetone
Center Frequency (GHz)	1	1.5
3 dB Fractional Bandwidth	33%	31%
Insertion Loss (dB)	1.4	1.3
Return Loss (dB)	25	15.8

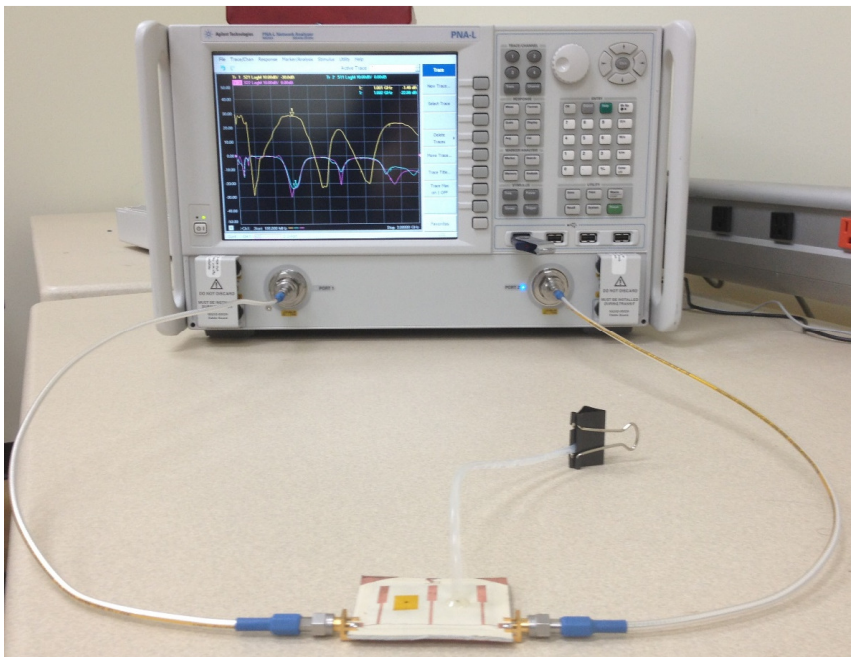

Fig. 5.8 Measurement setup for the tunable filter.

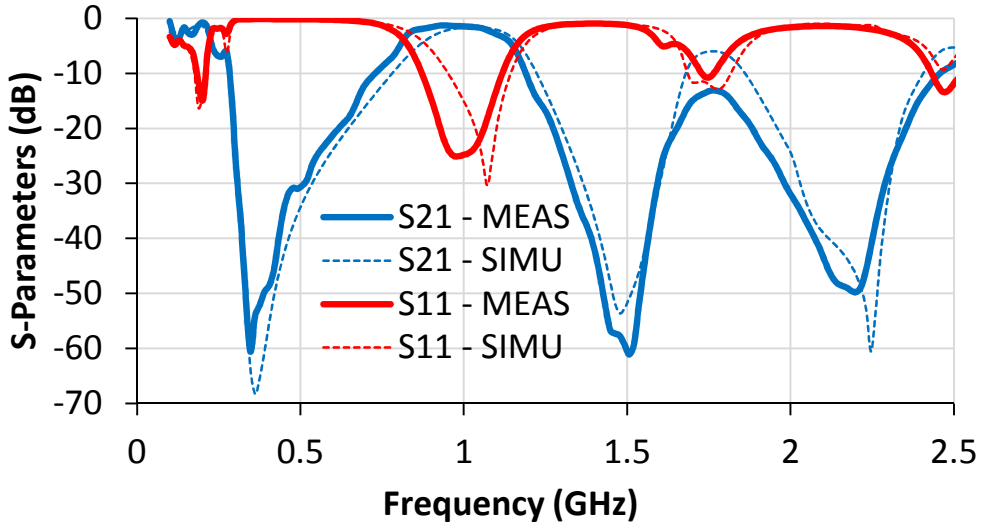

(a)

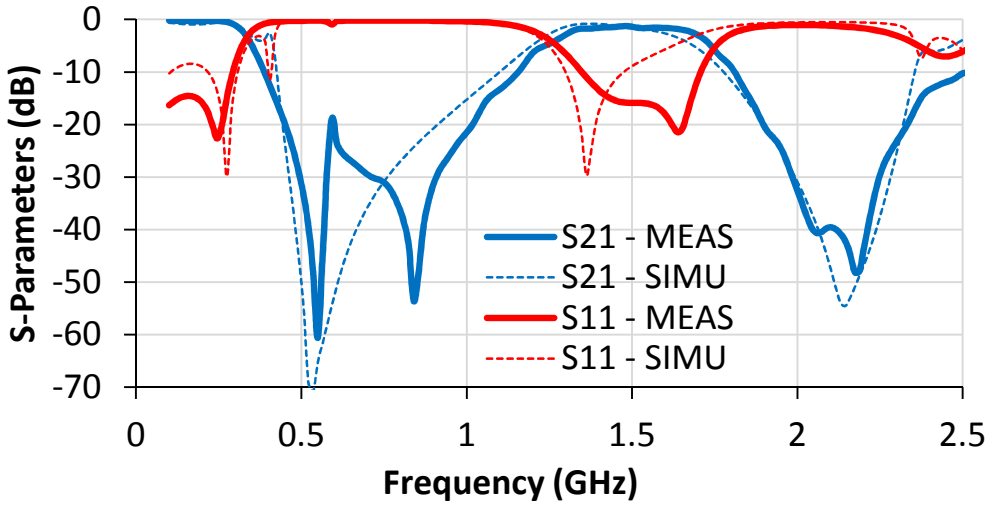

(b)

Fig. 5.9 Comparison of simulated and measured S-Parameters for a) DI water b) acetone.

5.4 Summary

A tunable L-band microstrip bandpass filter on LCP with an integrated microfluidic channel has been presented. Design guidelines about how to choose the thicknesses of the LCP layer and the channel were discussed. The filter has been successfully fabricated and measured. Measured data accurately matched HFSS simulations. The center frequency of the filter was shifted from 1 GHz for DI water to 1.5 GHz for acetone, i.e. 50% tuning was achieved. There was no significant change

for the 3 dB FBW and for the insertion loss, the return loss was affected but was still above 15.8 dB.

CHAPTER 6

MICROFLUIDICALLY RECONFIGURABLE GAN POWER AMPLIFIER ON MULTILAYER ORGANIC SUBSTRATE

Tunable PAs are useful RF components for multiband wireless applications. A microfluidic tuning technique similar to the approach discussed in Chapter 5 is used to design a tunable RF PA on organics. A novel way is presented on how to combine the advantages of organic substrates and the high power capabilities of GaN devices by designing a reconfigurable GaN-based PA that can work optimally at 2.4 GHz and 5.8 GHz based on the fluid injected inside the matching networks micromachined channels. The choice of the frequencies is very suitable for wireless local area network (WLAN) applications. This solution paves the way for combining tuning and cooling at the same time by circulating different fluids for different purposes (see Chapter 7). This is the first time microfluidics are used to design a reconfigurable GaN-based PA.

6.1 Tunable Power Amplifier Design

6.1.1 General Overview

The objective of this study is the design and implementation of a reconfigurable PA that can work optimally for two different frequencies: 2.4 GHz and 5.8 GHz. In order to achieve the desired tunability, reconfigurable matching networks are used to present different optimal impedances to the transistor die depending on the frequency (Fig. 6.1). The source and load matching networks frequency response is changed by using different fluids inside their respective microchannels. In this work, acetone (ε_r = 20.7) and air (ε_r = 1) are used to provide optimal impedances at 2.4 GHz and 5.8 GHz respectively.

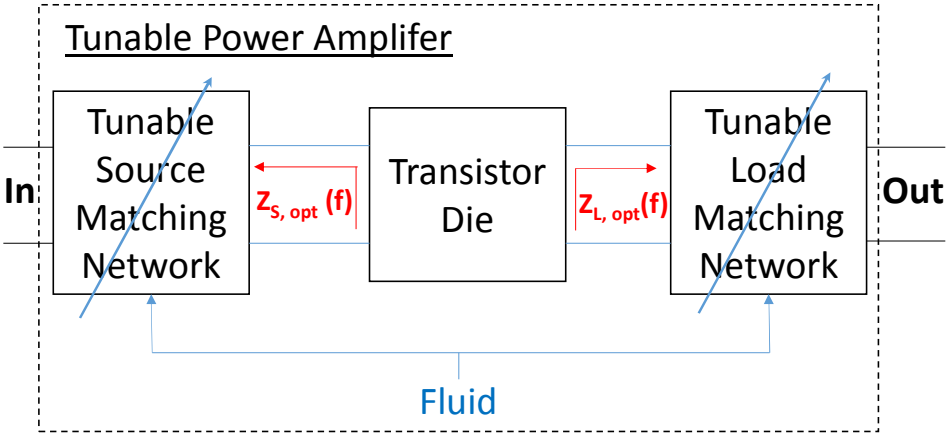

Fig. 6.1 Proposed tunable PA functional diagram.

6.1.2 Device Under Test

The transistor die used is a high voltage gallium nitride (GaN) high electron mobility transistor (HEMT) on a silicon carbide (SiC) substrate using a 0.25 um gate length fabrication process. The overall size of the die is 0.8 mm x 0.84 mm with a thickness of 100 um. Fig. 6.2 is a top view picture of the die.

A series gate resistance of 12.5 Ω is needed to stabilize the transistor at 2.4 GHz. Four SMD RF chip resistors with a value of 50 Ω each are placed in parallel to get the desired value. Because the transistor needs to operate at 5.8 GHz as well, a capacitor (2 pF) is placed in parallel with the resistors. The die is connected to the input and output networks by the means of 1 mil thick bond wires. The input and output pads are modeled as shunt capacitors and series inductors. The DUT is the combination of

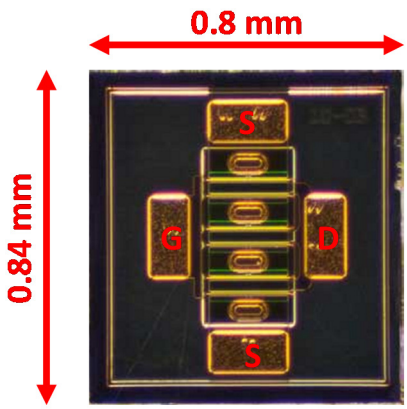

Fig. 6.2 GaN HEMT top view picture.

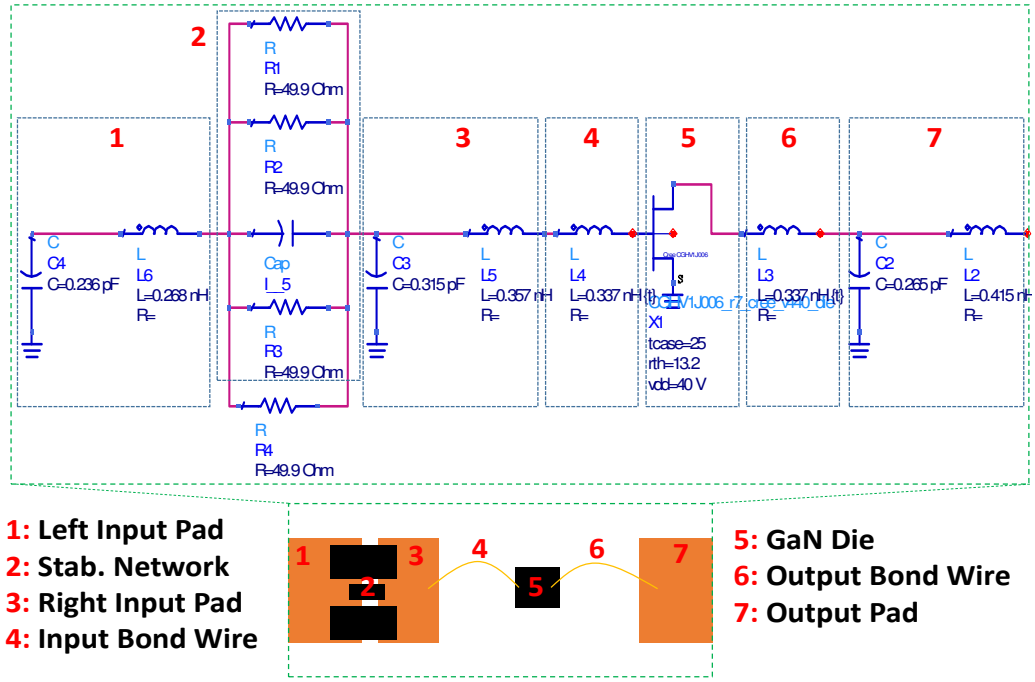

Fig. 6.3 Device under test illustration.

the input and output pads, the stabilization network, the input and output bond wires, and the transistor die (Fig. 6.3).

6.1.3 Load and Source Pull Simulations

Load and source pull simulations were performed on the DUT described in Secton 6.1.2 at 2.4 GHz and 5.8 GHz using Agilent Advanced Design System (ADS). A drain voltage V_{DS} = 40 V and a quiescent drain current I_{DS} = 60 mA were used in the simulation. The optimal impedances were obtained by iterative source and load pull simulations until convergence was reached. The optimization goal was to get the best trade-off between the maximum power added efficiency (PAE) and the maximium output power (P_{out}). The simulation results are summarized in Table 6.1.

6.1.4 Tunable Matching Networks

The tunable matching networks are designed on a multilayer organic substrate consisting of a 2 mil thick LCP layer (ε_r = 2.9) on top of a 20 mil thick Duroid layer (ε_r = 3). Fig. 6.4 is a cross sectional view of the stack-up used along with the different

TABLE 6.1
LOAD AND SOURCE PULL SIMULATION RESULTS

Frequency (GHz)	2.4	5.8
K Factor	1.228	1.256
MAG (dB)	22.309	18.442
P_{in} (dBm)	21	25
$Z_{S,\,Opt}$ (Ω)	11.723+j9.720	14.287-j32.158
$Z_{L,\,Opt}$ (Ω)	42.633+j47.014	16.298+j12.767
Max. PAE (%)	57.39	53.19
Max. P_{out} (dBm)	38.103	38.271
Gain (dB)	17.103	13.271

Fig. 6.4 2D cross sectional view of the stack-up.

thicknesses. The channel thickness of 20 mil was chosen because it allows the design of low impedance lines while providing a reliable mechanical support for the microchannel.

The proposed topology for the tunable matching networks consists of two cascaded single matching networks M1 (Line 1 and Line 2) and M2 (Line 3 and Line 4). The one closer to the die (M1) matches Z_{Opt} to 50 Ω at 2.4 GHz with acetone in the microchannel, while M2 matches the impedance presented by M1 to the impedance presented by a quarter wavelength transfomer (Line 5) at 5.8 GHz with air filling the microchannel. Lines 1, 3 and 5 are all 50 Ω lines at 2.4 GHz with acetone in the microchannel. At 2.4 GHz, if Line 4 has an electrical length of 180°, then M2 has no effect on the matching. At 5.8 GHz, and with air filling the microchannel, M1 transformms Z_{Opt} to another impedance Z_{Opt}' which M2 transforms into $Z0_5^2/50$ where $Z0_5$ is the impedance of Line 5 with air filling the microchannel. The only constraint with this kind of approch is that Line 4 has to satisfy two conditions at the same time:

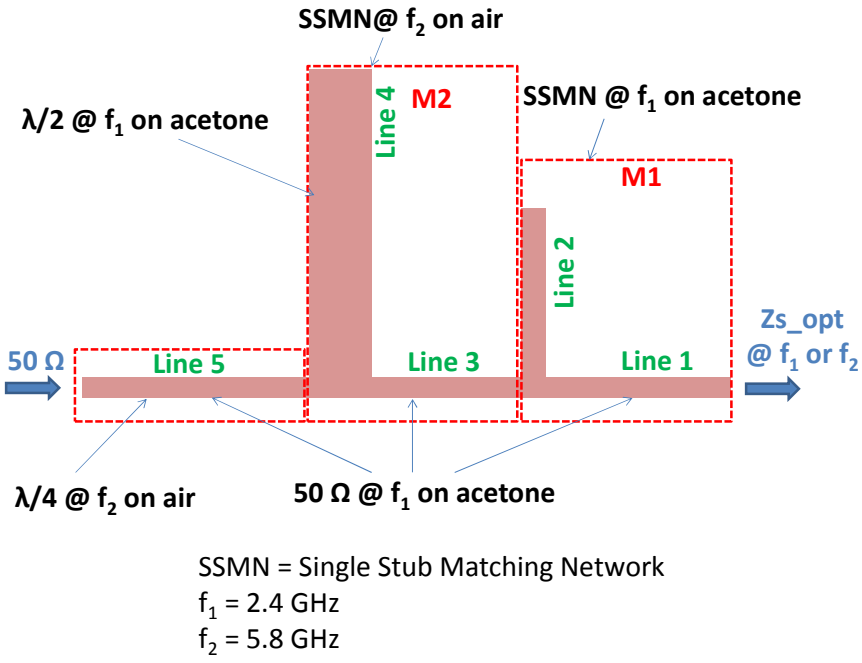

Fig. 6.5 Tunable source matching network design.

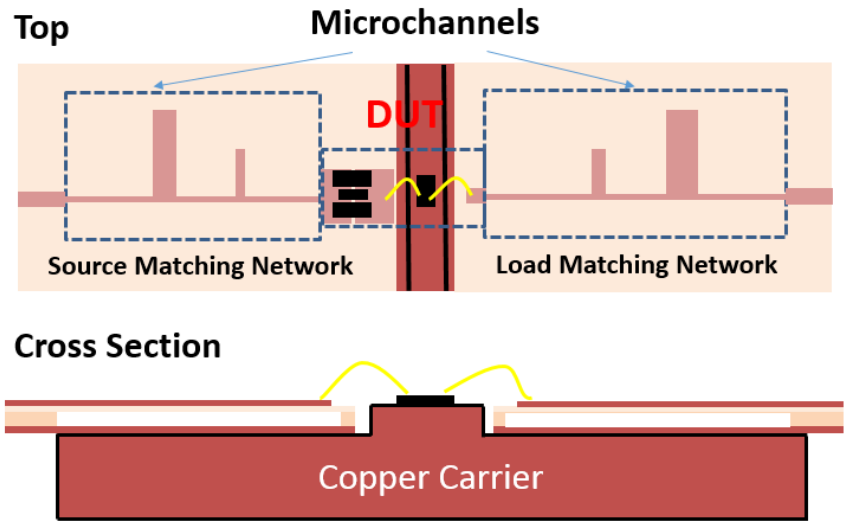

Fig. 6.6 Top and cross sectional view of the packaged PA.

1) be a λ/4 line at 2.4 GHz, 2) have a specific length that can match Z_{Opt}' to $Z0_5^2/50$ at 5.8 GHz. This condition is only met for one specific characteristic impedance of Line 4, for this application it comes to be around 20 Ω with acetone in the microchannel. The source and load matching networks are attached to a 5 mm thick copper carrier on top of which the die is sitting. A more thorough explanation of the equations behind the deisgn can be found in Chapter 7. Fig. 6.5 is a detailed illustration of the source

matching network design. The same design steps are applied to the load matching network. An illustration of the packaged PA is shwon in Fig. 6.6.

6.2 Fabrication Procedure

The fabrication starts with a 20 mil copper double clad RO3003 panel (6 in x 6 in). Copper is etched out from both sides using a wet etching process. Source and load matching networks cavities are ablated on it with dimensions 27 mm x 20.2 mm and 27.4 mm x 27 mm respectively. The copper is etched out from one side of a 2 mil copper double clad LCP (ULTRALAM 3850) panel (6 in x 6 in) and vias, with a diameter of 1.2 mm, are drilled on it. These vias serve as injection points for the fluids after the assembly is done. Two 1 mil bondplies (ULTRALAM 3908) (6 in x 6 in) are used in between the different layers to bond the whole stack-up after the lamination process. LCP and Duroid along with a 6 mil copper shim are laminated using a hot thermal press at a temperature of 285°C and a pressure of 300 psi. A seed layer of titanium (40 nm) is deposited on top of copper, and a layer of gold (0.4 um) is deposited on top of titanium using electron beam evaporation. Gold is required for wire-bonding during the assembly phase. With this fabrication procedure, four source matching networks and four load matching networks can be fabricated in one fabrication cycle. The panel is cut into four 3 in x 3 in samples, metal patterning is done on each one of them using standard lithography techniques (Fig. 6.7). Fig. 6.8 (a) is a picture of the packaged PA and Fig. 6.8 (b) is a zoomed picture of the wire-bonded die.

Fig. 6.7 3 in x 3 in patterned sample: source matching networks on the left, load matching networks on the right.

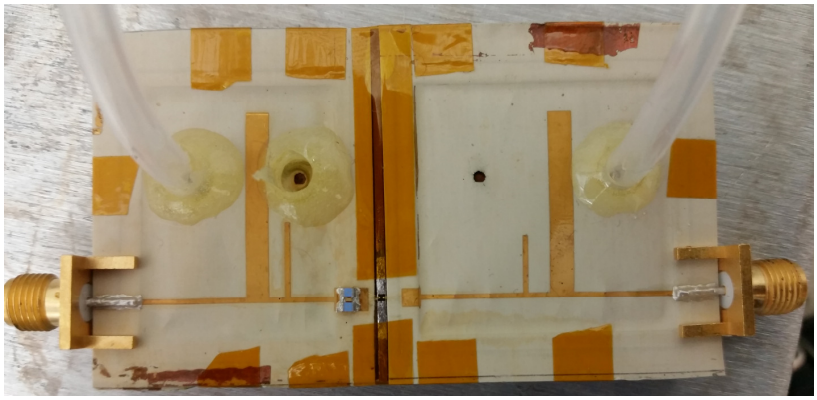

(a)

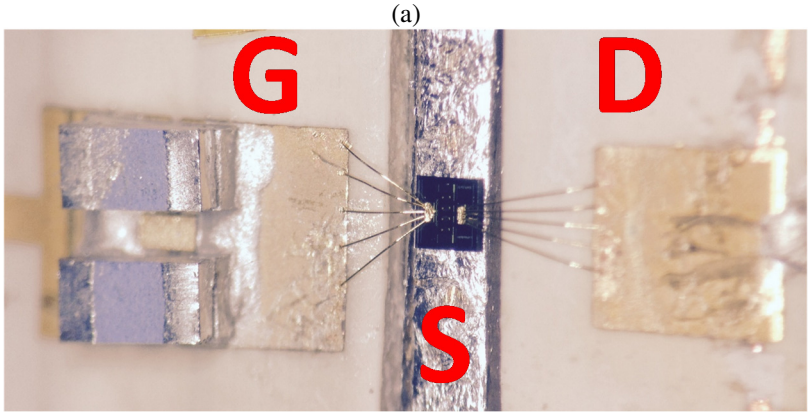

(b)

Fig. 6.8 Picture of the a) packaged PA b) GaN die.

6.3 Measurements and Results

The large signal data of the packaged PA was obtained using vector-receiver load pull measurements. Power sweeps are done at 50 Ω at the input and output with 10 % duty cycle and were compared with simulation. Because there were small shifts in the small signal gain for both acetone and air configurations, load pull measurements were done at 5.7 GHz for air and at 2.3 GHz for acetone while the simulated data was characterized at 5.8 GHz and 2.4 GHz respectively (Fig. 6.9). Overall, large signal measured results indicate that the microfluidic tuning solution presented in this work is working well. Because there was a mismatch at the source side with acetone, the overall performance was degraded compared to simulation at 2.4 GHz, but the measured data for the PA with air agrees well with the simulated data at 5.8 GHz. The measured PA characteristics with acetone are: P_{in} = 21 dBm, P_{out} = 35.02 dBm, PAE = 36.41 %. The measured PA characteristics with air are: P_{in} = 25 dBm, P_{out} = 36.88 dBm, PAE = 44.03 %.

6.4 Summary

A reconfigurable GaN-based PA at 2.4 GHz and 5.8 GHz has been presented for the first time using microfluidic channels integrated in a multilayer organic substrate. This PA has been successfully designed, simulated, fabricated and measured. new technique has been developed and described regarding the design of tunable matching networks. By changing the fluids (acetone and air) inside the source and load matching networks microchannels, and by carefully designing the microstrip lines, the optimal impedances presented to the transistor die have been tuned depending on the frequency of operation. The PA has an output power of 3.18 W / 4.88 W and a PAE of 36.41 % / 44.03 % for an input power of 21 dBm / 25 dBm at 2.3 GHz / 5.7 GHz respectively.

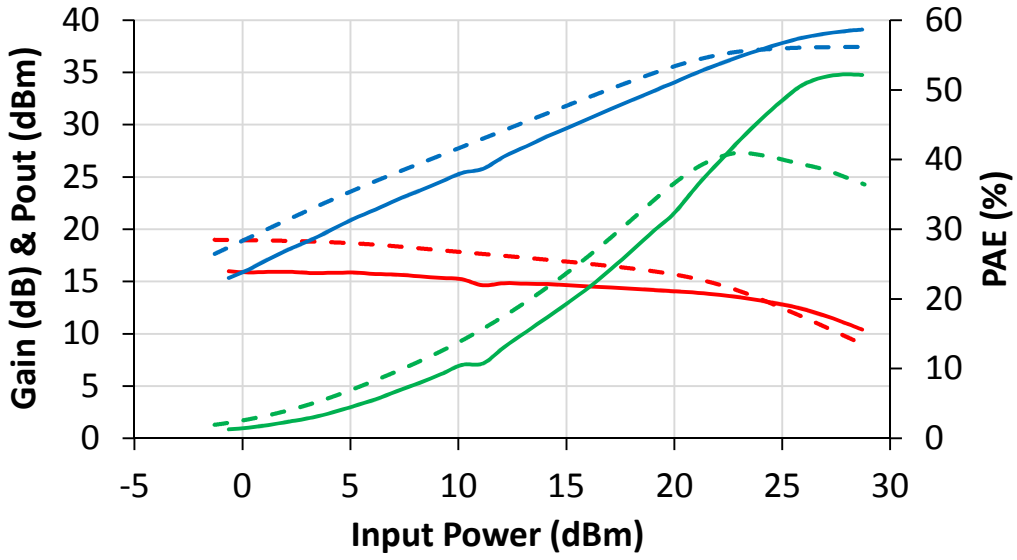

(a)

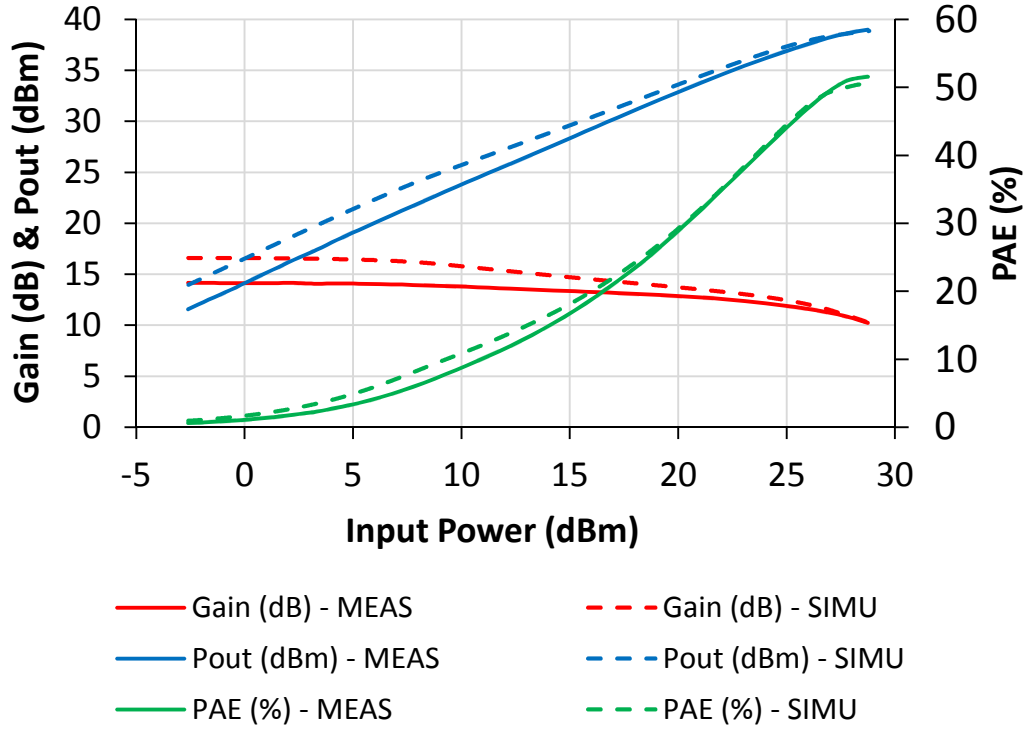

(b)

Fig. 6.9 a) Acetone configuration: measurements @ 2.3 GHz, simulations @ 2.4 GHz b) Air configuration: measurements @ 5.7 GHz, simulations @ 5.8 GHz.

PART III

COMBINED COOLING AND TUNING ON MULTILAYER ORGANIC SUBSTRATE

"A fact is a simple statement that everyone believes. It is innocent, unless found guilty. A hypothesis is a novel suggestion that no one wants to believe. It is guilty, until found effective."

-Edward Teller

Up to this point, cooling and tuning have been studied separately in order to better analyze the effects of each one of them. In this final part, tuning and cooling are combined together in a single organic multilayer package where a GaN-based PA is cooled and tuned at the same time. The GaN die is now sitting directly on top of LCP, and it is the integrated cooling solution described in Part I which deals with heat removal. The benefits of such an approach is a reduced size and weight of the system with high integration prospects with other front-end modules. Due to some instabilities encountered with die sitting directly on LCP, a copper-based PA with integrated microchannels is measured instead of the organic PA. Following the same methodology applied for the cooling part, multilayer microstrip design techniques are thoroughly analyzed, and equations and guidelines are given for the design of tunable matching networks.

CHAPTER 7

COOLING AND TUNING OF A GAN-BASED PA ON MULTILAYER ORGANIC SUBSTRATE

All the techniques developed in Part I and Part II are combined into a single organic packaged design. The objective of this work is to successfully cool and tune an RF GaN-based PA using integrated microfluidics on organics. Before going into the details of the PA design, multilayer microstrip design theory is developed and tunability parameters are defined. That would give the reader the necessary background to understand the design equations for microfluidically tunable matching networks.

7.1 Microchannels for Cooling and Tuning

There are two types of integrated microchannels used in this work:

1) *Cooling microchannels*: these microchannels are placed beneath the heat source to cool down the device. The liquid used for cooling is DI water, the cooling requires a pumping mechanism (micropumps) to ensure a steady flow of the coolant. These channels are localized and are only wide enough to cover the heat source area. This type of channels can be particularly interesting for high power applications.

2) *Tuning microchannels*: these microchannels are placed below the RF microstrip lines and are used to tune the frequency of operation of the reconfigurable RF structure. This is achieved by changing the fluid inside the microchannel, which in turn changes the effective dielectric constant of the medium where the electromagnetic wave travels. The motion of the fluid is not required, there should only be a way to get the fluid in and out. The dimensions of the microchannels are big enough to cover the area of the microstrip lines. This type of channels is useful for applications involving reconfigurable RF systems.

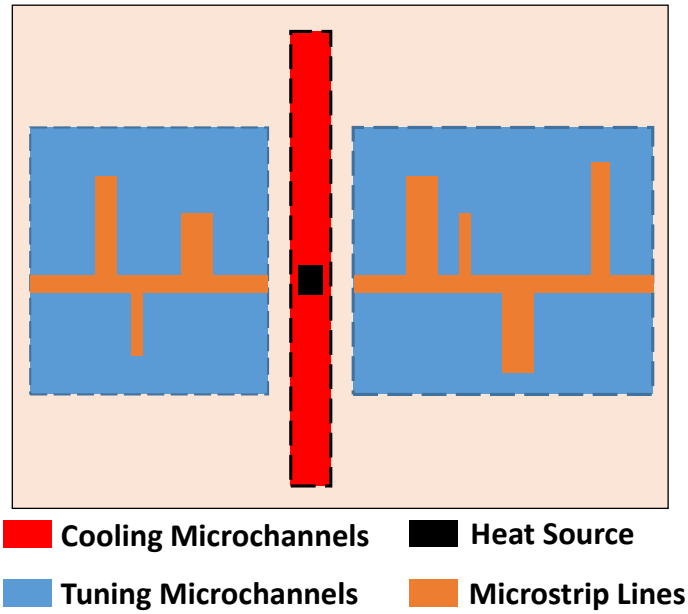

Fig. 7.1 Simplified sketch for cooling and tuning microchannels in a single design.

Combining these two types of channels in a single design is therefore suitable for high power reconfigurable RF designs, the idea of the implementation is illustrated in Fig. 7.1. As the characterization of cooling microchannels has been thoroughly studied in Chapter 4, we focus here on the tuning microchannels and how to design the microstrip lines on top of these microchannels for reconfigurable RF designs. Because of the presence of a microchannel, the RF signal will be carried on a substrate with at least two layers (cavity layer and the RF substrate), that is why we discuss in the next section the methodology used for synthesizing the microstrip line dimensions on a multilayer substrate.

7.2 Multilayer Microstrip Design

7.2.1 Approximate Methods for the Analysis and Synthesis of Microstrip Lines on a Multilayer Substrate

7.2.1.1 Multilayer vs Single-Layer Designs

The analysis and synthesis of microstrip lines on a single-layer substrate is now trivial, there are many reliable closed-form formulas for the characteristic impedance

Z_0 and the effective dielectric constant ε_{reff} [86] and there are a few automated tools that are based on those expressions that help during the design phase (e.g. LineCalc from ADS). While extensive material can be found regarding microstrip design on a single-layer substrate, it is very challenging to find a simple closed form expression for the multilayer case. The few formulas that are found are either very complex or very simplistic [83], or they work only under certain conditions or they do not match with the simulators.

One solution for the multilayer case could be to rely entirely on simulators like ADS to extract Z_0 and ε_{reff}, but this is time consuming especially that there is no way to extract ε_{reff} directly under ADS, although Z_0 is available. HFSS offers the possibility of extracting both values at the end of the simulation, but the simulation time is usually long and there is no automated way of reusing the extracted values in a script for optimization. However, for simple multilayer designs where there is no need to optimize line dimensions several times, this method could be a viable option. In this work, and as explained in Section 7.3.2, the length of a particular line in the design needs to be optimized to satisfy two simultaneous conditions. For that to be possible, Z_0 and ε_{reff} values need to be reevaluated at least a 1000 times in a written Matlab script, that is why it is necessary to have an accurate closed-form expression to analyze and synthesize line dimensions on a multilayer substrate.

A closed-form expression using the conformal mapping method for generalized multilayer microstrip designs has been suggested in [87], but when compared with simulators, the ε_{reff} value does not quite match. A correction to the ε_{reff} expression in equation (15) found in [87] is suggested in this work based on the two-layer closed form expression obtained in equation (16) in [88]. The derivation of Z_0 is also derived from [88]. To verify the results from [88], another two-layer closed form expression was

used for comparison in [89]. The factor K'/K has to be approximated, the value was substituted with a better approximation found in [90] (page 55), also K_{air} has to be found in another paper [86]. It has to be noted that all these formulas do not take into account the line thickness and the frequency of operation compared to the single-layer case where such formulas exist [86, 91-93]. Hence, the idea is to transform the multilayer problem into an equivalent single-layer problem by extracting the equivalent ε_r of the single-layer substrate that would yield the same ε_{reff}. The equations used and the steps followed are summarized here in an effort to provide the reader with accurate, corrected and tested expressions for the multilayer microstrip design in one place, the reader can then duplicate these steps easily without the need to go back to the aforementioned papers.

7.2.1.2 Extraction of Z_0 and ε_{reff} for a 2-layer Substrate

Given the two-layer problem depicted in Fig. 7.2, the following equations are used based on the results found in [89], [90] and [86]:

$$\varepsilon_{r_{eff}} = 1 + 2(\varepsilon_{eq} - 1)K_{air}G(k) \tag{7.1}$$

$$Z_0 = \frac{Z_0^{air}}{\sqrt{\varepsilon_{r_{eff}}}} \tag{7.2}$$

where:

$$G(k) = \frac{K'(k)}{K(k)} \approx \frac{2}{\pi}\operatorname{arccosh}\left(\frac{1+k'}{k} + \frac{k\sqrt[4]{k'}}{4(1+k')}\right) \tag{7.3}$$

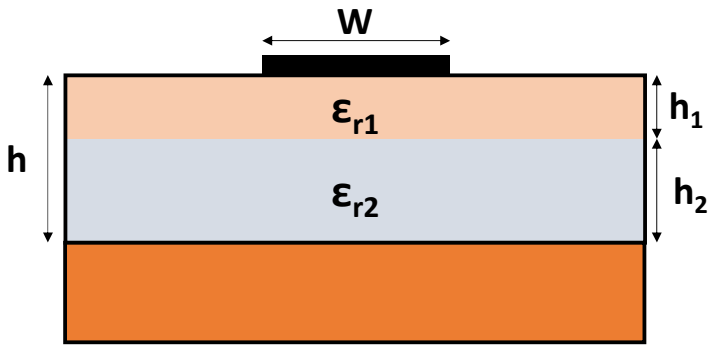

Fig. 7.2 A microstrip line on top of a two-layer substrate.

$$\begin{cases} k = \dfrac{1}{cosh\left(\frac{\pi}{4}u\right)} \;\; ; \quad k' = \sqrt{1-k^2} \\ k_1 = \dfrac{1}{cosh\left(\frac{\pi}{4}u_1\right)} \;\; ; \quad k_1' = \sqrt{1-k_1^2} \end{cases} \tag{7.4}$$

$$\begin{cases} u = {}^{W}/_{h} \\ u_1 = {}^{W}/_{h_1} \end{cases} \tag{7.5}$$

$$\varepsilon_{eq} = \frac{d_1 + d_2}{\frac{d_1}{\varepsilon_{r1}} + \frac{d_2}{\varepsilon_{r2}}} \tag{7.6}$$

$$\begin{cases} d_1 = \dfrac{1}{G(k_1)} \\ d_2 = \dfrac{1}{G(k)} - d_1 \end{cases} \tag{7.7}$$

$$K_{air} = \frac{Z_0^{air}}{120\pi} \tag{7.8}$$

$$Z_0^{air} = 60ln\left(\frac{f(u)}{u}\sqrt{1+\left(\frac{2}{u}\right)^2}\right) \tag{7.9}$$

$$f(u) = 6 + (2\pi - 6)exp\left(-\left(\frac{30.666}{u}\right)^{0.7528}\right) \tag{7.10}$$

7.2.1.3 Extraction of Z_0 and ε_{reff} for an M-layer Substrate

The model in the last section works only for single-layer and two-layer substrates. To extend the functionality to any number of layers M (Fig. 7.3), the model in [87] is used instead, along with the correction brought from [88]. This model also allows to study the cases where there are additional layers placed on top of the conductor line. To get the standard microstrip case where air is at the top, M should be set to N-1 and ε_{rM+1} to 1. For this model, the following equations are used:

$$\varepsilon_{r_{eff}} = q_N + \frac{\left(\sum_{i=1}^{N-1} q_i\right)^2}{\sum_{i=1}^{N-1} \frac{q_i}{\varepsilon_{ri}}} \tag{7.11}$$

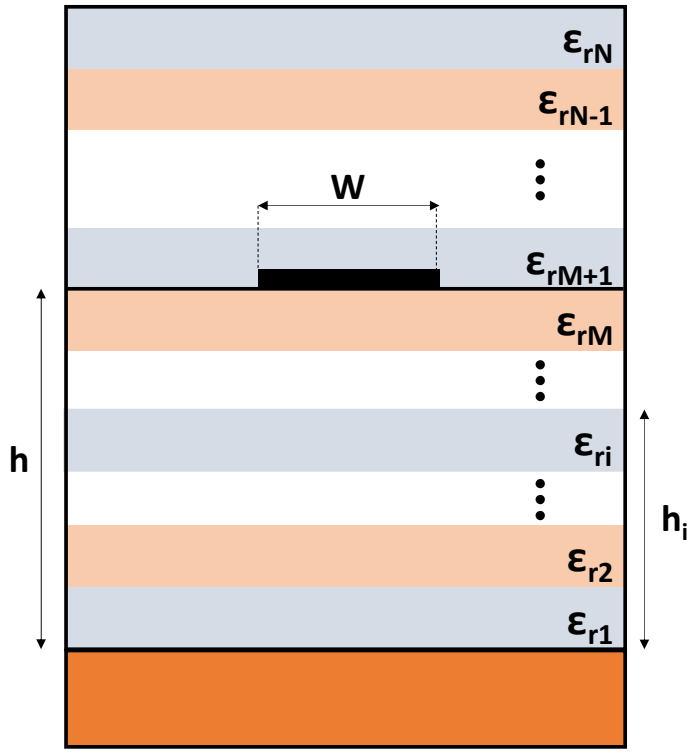

Fig. 7.3 A microstrip line on top of an M-layer substrate.

$$\begin{cases} Z_0 = \dfrac{60}{\sqrt{\varepsilon_{r_{eff}}}} ln\left(\dfrac{8h}{W}\right) & for\ {}^{W}/_{h} \leq 1 \\ Z_0 = \dfrac{120\pi}{\sqrt{\varepsilon_{r_{eff}}}} \dfrac{h}{W_{eff}} & for\ {}^{W}/_{h} \geq 1 \end{cases} \tag{7.12}$$

where for W/h ≤ 1:

$$f_1(H,A) = \frac{ln(A)}{2ln\left(\frac{8h}{W}\right)}\left[1 + \frac{\pi}{4} - \frac{1}{2} arccos\left(\frac{W}{8hH}\sqrt{A}\right)\right] \tag{7.13}$$

$$f_2(H,A) = \frac{1}{2} - \frac{0.9 + \frac{\pi}{4} ln(A) \arccos\left[\left(1 - \frac{1 - \frac{W}{8h}}{H}\right)\sqrt{A}\right]}{\pi ln\left(\frac{8h}{W}\right)} \tag{7.14}$$

$$\begin{cases} q_1 = f_1(H_1, A_1) \\ q_i = f_1(H_i, A_i) - f_1(H_{i-1}, A_{i-1})\ , i = 2..M-1 \\ q_M = \dfrac{1}{2} + \dfrac{0.9}{\pi ln\left(\frac{8h}{W}\right)} - f_1(H_{M-1}, A_{M-1}) \\ q_{M+1} = f_2(H_{M+1}, A_{M+1}) \\ q_i = f_2(H_i, A_i) - f_2(H_{i-1}, A_{i-1})\ , i = M+1..N-1 \end{cases} \tag{7.15}$$

$$\begin{cases} A_i = \dfrac{1 + H_i}{1 - H_i + \dfrac{W}{4h}}, i = 1..M \\ A_i = \dfrac{1 + H_i}{H_i - 1 + \dfrac{W}{4h}}, i = M + 1..N \end{cases} \tag{7.16}$$

and for W/h ≥ 1:

$$W_{eff} = W + \frac{2h}{\pi} ln\left[17.08\left(\frac{W}{2h} + 0.92\right)\right] \tag{7.17}$$

$$f_3(H) = \frac{H}{2}\left[1 + \frac{\pi}{4} - \frac{h}{W_{eff}} ln\left(2\frac{W_{eff}}{h}\frac{sin\left(\frac{\pi}{2}H\right)}{H} + \cos\left(\frac{\pi}{2}H\right)\right)\right] \tag{7.18}$$

$$f_4(H,V) = \frac{h}{2W_{eff}}\left\{ln\left(\pi\frac{W_{eff}}{h} - 1\right) - (1+V)ln\left[2\frac{W_{eff}}{h}\frac{cos\left(\frac{\pi}{2}V\right)}{2H - 1 + V} + sin\left(\frac{\pi}{2}V\right)\right]\right\} \tag{7.19}$$

$$\begin{cases} q_1 = f_3(H_1) \\ q_i = f_3(H_i) - f_3(H_{i-1}), i = 2..M-1 \\ q_M = 1 - \dfrac{h}{2W_{eff}} ln\left(\pi\dfrac{W_{eff}}{h} - 1\right) - f_3(H_{M-1}) \\ q_{M+1} = f_4(H_{M+1}, V_{M+1}) \\ q_i = f_4(H_i, V_i) - f_4(H_{i-1}, V_{i-1}), i = M+1..N-1 \end{cases} \tag{7.20}$$

$$V_i = \frac{2}{\pi} arctan\left(\frac{\pi}{\frac{\pi}{2}\frac{W_{eff}}{h} - 2}(H_i - 1)\right), i = M+1..N \tag{7.21}$$

and for all W/h:

$$H_i = \frac{h_i}{h} \tag{7.22}$$

$$q_N = 1 - \sum_{i=1}^{N-1} q_i \tag{7.23}$$

7.2.1.4 Conductor Thickness and Frequency Dependency

To be able to use the microstrip models that take into account conductor thickness and the dispersion effects as input parameters, the values of Z_0 and ε_{reff} are transformed into a single-layer substrate with an equivalent dielectric constant ε_{req}. In order to achieve that, we simply reverse the synthesis formula found in [94] for the single-layer case, and so we obtain:

$$\varepsilon_{r_{eq}} = \frac{2\varepsilon_{r_{eff}} + a - 1}{a + 1} \tag{7.24}$$

where:

$$a = \frac{1}{\sqrt{1 + \frac{12}{u}}}, u = {}^{W}/_{h} \tag{7.25}$$

After reaching this point, it is straightforward to use the conductor thickness model in [86] and any microstrip dispersion model (the Kirschning and Jansen model in [91] was used in this work).

7.2.1.5 Synthesis of Microstrip Lines on a Multilayer Substrate

It is obvious from the previous results that it is impossible to derive a closed-form expression to synthesize the width W of a microstrip line given its characteristic impedance Z_0. We use the dichotomy (or bisection) method to find a root to the function $f(W)=Z(W)-Z_0$ where Z(W) is one of the analysis functions discussed in Section 7.2.1.2 and Section 7.2.1.3. The algorithm flowchart is detailed in Fig. 7.4.

7.2.2 Converging Method for High Precision Extraction of Z_0 and ε_{reff} on a Multilayer Substrate

The synthesis function for multilayer microstrip design described in Section 7.2.1.5 offers many advantages; 1) it gives a good approximation of Z_0 and ε_{reff}, 2) the speed of the synthesis is very fast and the results are almost instantaneous and 3) it is very suitable for optimizations where the number of iterations is high during the simulation design phase. However, the values obtained are only approximations, and the error accumulates when the number of lines increases. Also, the microstrip frequency dispersion effect becomes very significant when the substrate height becomes large, which introduces significant errors compared with the already existing

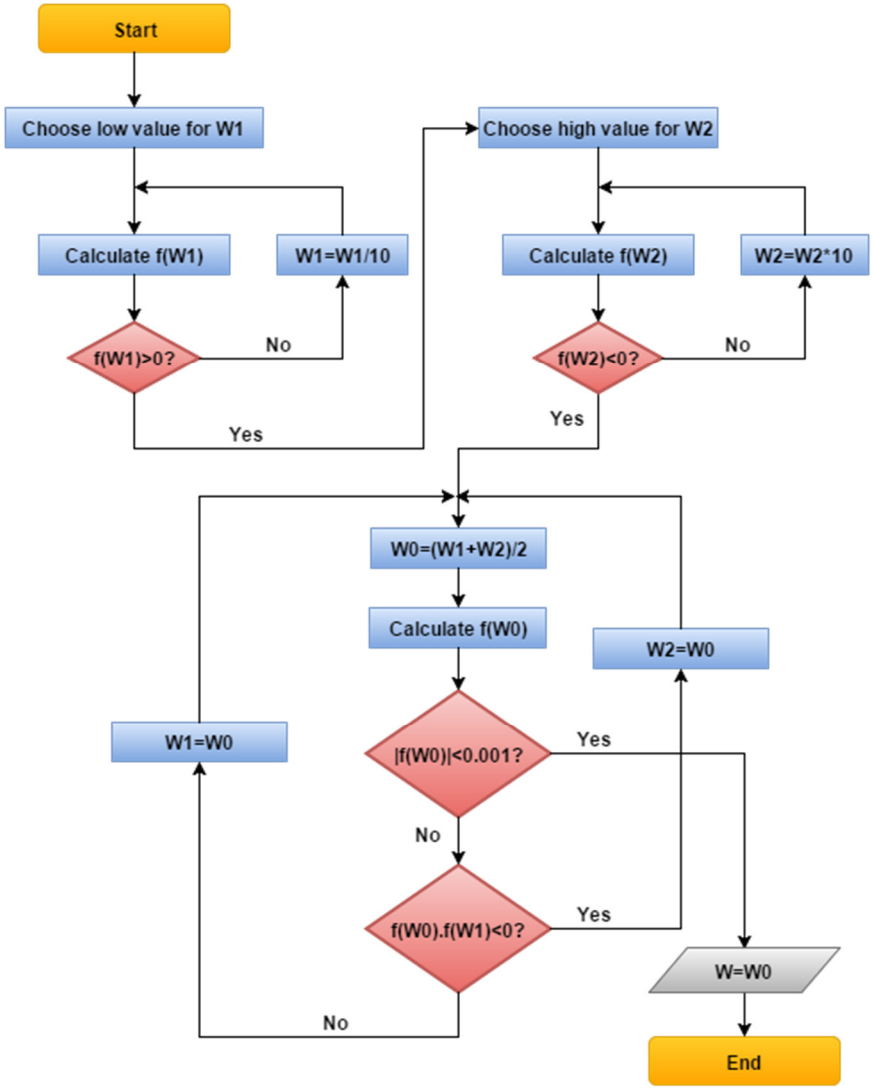

Fig. 7.4 Synthesis algorithm flowchart.

dispersion models. Moreover, the transformation done in 7.2.1.4 is only an approximation of a single-layer substrate in order to make the use of single-layer dispersion models possible, but this introduces inevitably further errors. It is not the intention to say that the work done in 7.2.1 is without importance, it is actually required to have a good starting approximation values at the simulation design phase, but the following logical step would be to optimize the length and the width of the lines under the simulator at the layout design phase to extract the real Z_0 and ε_{reff} that is internally used by the simulator. As mentioned before, the ε_{reff} value is not available under ADS to check the validity of the values obtained from the model. Therefore, the problem to

solve is the following: given a certain microstrip line width W on top of a substrate with any number of layers, what is the effective dielectric constant at a certain frequency point f_0, $\varepsilon_{reff}(W,f)$? Below are the steps to follow:

1) The analysis function in 7.2.1 is used on a line of width W to get a first approximation of Z_0 and ε_{reff}. The length of a 90° line is then calculated as follows:

$$L = \frac{C}{4f\sqrt{\varepsilon_{r_{eff}}}} \tag{7.26}$$

The λ/4 length is specifically chosen to maximize the phase error. Any length that is not close to a multiple of λ/2 would work.

2) A lossless microstrip line of length L and width W is simulated under ADS with two simulation ports of impedances Z_1 and Z_2 respectively. The impedance of the second simulation port Z_2 must be chosen such that $Z_2 \neq Z_0$.

3) The value $S_{11}(f)$ is extracted from the simulation. The normalized input impedance is then calculated as:

$$z'_{in} = \frac{1 + S_{11}}{1 - S_{11}} \tag{7.27}$$

4) Based on transmission line theory, the following equations have been developed to calculate the new ε_{reff}:

$$\varepsilon_{r_{eff}} = \left(\frac{C}{nLf}\right)^2 \tag{7.28}$$

where:

$$n = \frac{2\pi}{E} \tag{7.29}$$

$$E \equiv \frac{1}{2} Arg\left(\frac{1+\alpha}{1-\alpha}\right)[\pi] > 0 \tag{7.30}$$

$$\alpha = \frac{z_{out} - z_{in}}{z_{in} z_{out} - 1} \tag{7.31}$$

$$z_{in} = \frac{Z_1 z'_{in}}{Z_0} \tag{7.32}$$

$$z_{out} = \frac{Z_2}{Z_0} \tag{7.33}$$

5) The updated value $\varepsilon_{r_{eff}}$ is used to find the new value of Z_0. Based on transmission line theory, the following equations are used:

$$Z_0 = \frac{1}{2\tan(E)} Im\left(Z_{in} - Z_{out} \pm \sqrt{(Z_{in} - Z_{out})^2 - 4tan^2(E) Z_{in} Z_{out}}\right) > 0 \tag{7.34}$$

where:

$$E = \frac{2\pi f L \sqrt{\varepsilon_{r_{eff}}}}{C} \tag{7.35}$$

$$Z_{in} = Z_1 z'_{in} \tag{7.36}$$

$$Z_{out} = Z_2 \tag{7.37}$$

6) Steps 4) and 5) are repeated until Z_0 and ε_{reff} converge to a fixed value within the specified precision range.

7) Because $\varepsilon_{reff}(W,f)$ does not vary much with L, any line with a width W can be designed to have any specific length λ/n at the specified frequency f by using the equation below:

$$L = \frac{C}{nf\sqrt{\varepsilon_{r_{eff}}}} \tag{7.38}$$

7.3 Tunable Power Amplifier Design

The concept of the tunable PA is similar to the one presented in 6.1.1. The GaN transistor die used is the same as the one described in 6.1.2. In this section, we detail further the tunability parameters and the design equations behind tunable matching networks.

7.3.1 Tunability Parameters

In this section, $M(Z_0, E, \varepsilon_{reff}, f)$ denotes a microstrip line M with a characteristic impedance Z_0 and an electrical length E designed on top of a multilayer substrate Sub

with an effective dielectric constant ε_{reff} at a certain frequency f. Let M=M(Z_{01}, E_1, ε_{reff1}, f_1), if the substrate and/or the frequency change then M=M(Z_{02}, E_2, ε_{reff2}, f_2). Z_{02}, E_2 and ε_{reff2} are obtained by first synthesizing the line width W on Sub_1 and then analyzing the same width W on Sub_2. We define the microstrip impedance ratio MIR and the microstrip electrical ratio MER as the percentage change of Z_0 and E respectively:

$$\begin{cases} MIR(Z_{0_1}) = \dfrac{Z_{0_2} - Z_{0_1}}{Z_{0_1}} \\ Z_{0_2} = (1 + MIR)Z_{0_1} \end{cases} \tag{7.39}$$

$$\begin{cases} MER(Z_{0_1}) = \dfrac{E_2 - E_1}{E_1} = \sqrt{\dfrac{\varepsilon_{r_{eff2}}}{\varepsilon_{r_{eff1}}}}\dfrac{f_2}{f_1} - 1 \\ E_2 = (1 + MER)E_1 \end{cases} \tag{7.40}$$

Fig. 7.5 is a plot of the variation of MER and MIR with the microstrip impedance Z_{01} with ε_{r1} = 20.7 (acetone), f_1 = 2.4 GHz, ε_{r2} = 1 (air) and f_2 = 5.8 GHz over a two-layer substrate composed of a channel of variable thickness t at the bottom and a 2 mil LCP layer (ε_r = 2.9) at the top. As an example on how to interpret these

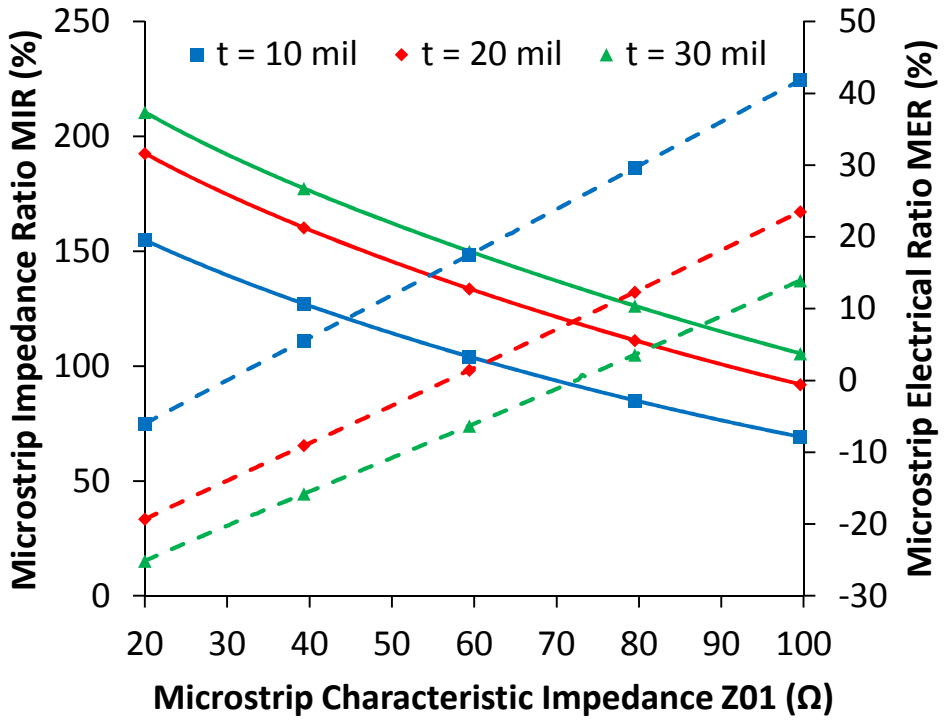

Fig. 7.5 Variation of MIR (solid lines) and MER (dashed lines) with the microstrip impedance Z_{01} and the channel thickness t.

results, if acetone is substituted with air inside a 20 mil channel, then a 50 Ω line on acetone at 2.4 GHz will see its characteristic impedance increase by 145.5 % (MIR = 145.5 %) and its electrical length decrease by 3.5 % (MER = -3.5 %) on air at 5.8 GHz.

7.3.2 Tunable Matching Networks Design

The tunable matching networks are designed on a multilayer organic substrate consisting of a 2 mil thick LCP layer ($\varepsilon_r = 2.9$) on top of a 20 mil thick RO3003 layer ($\varepsilon_r = 3$). Fig. 7.6 is a cross sectional view of the stack-up used along with the different thicknesses. The channel thickness of 20 mil is chosen because it allows the design of low impedance lines for reasonable line widths while providing a reliable mechanical support for the microchannel.

The topology of the tunable matching networks consists of two standard single stub matching networks M_1 and M_2 at the source and at the load. Fig. 7.7 is an example of a tunable source matching network, the design methodology is the same for the load matching network. The top and cross sectional view of the complete structure is shown in Fig. 7.8. M_1 and M_2 are used to match the optimal source impedance $Z_S(f_1 = 2.4\ \text{GHz})$ and $Z_S(f_2 = 5.8\ \text{GHz})$ to 50 Ω respectively. M_1 consists of two microstrip lines L_1 and L_2 while M_2 is composed of two other lines L_3 and L_4. The tunable source matching network has a fifth line L_5 from the signal input side. The design is complete when the pairs (Z_{0i}, E_i) i=1..5 are determined where Z_{0i} and E_i are the characteristic impedance and the electrical length of the line L_i respectively.

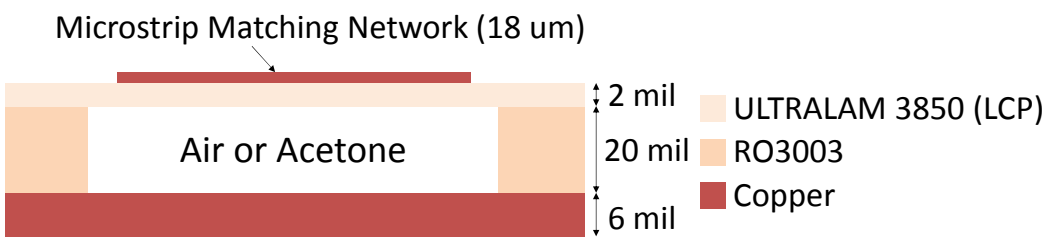

Fig. 7.6 2D cross sectional view of the stack-up.

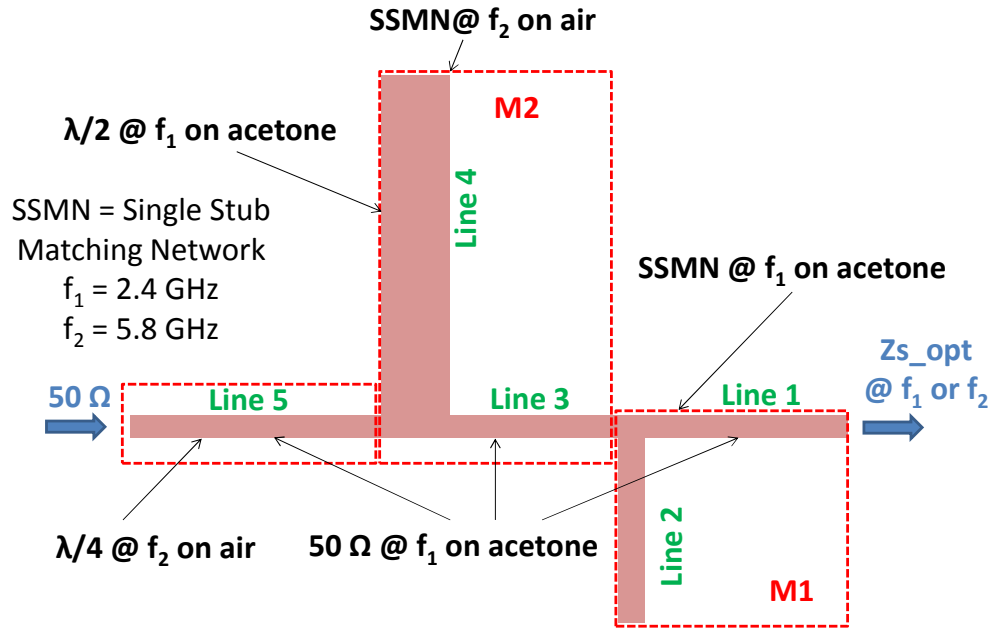

Fig. 7.7 Tunable source matching network design.

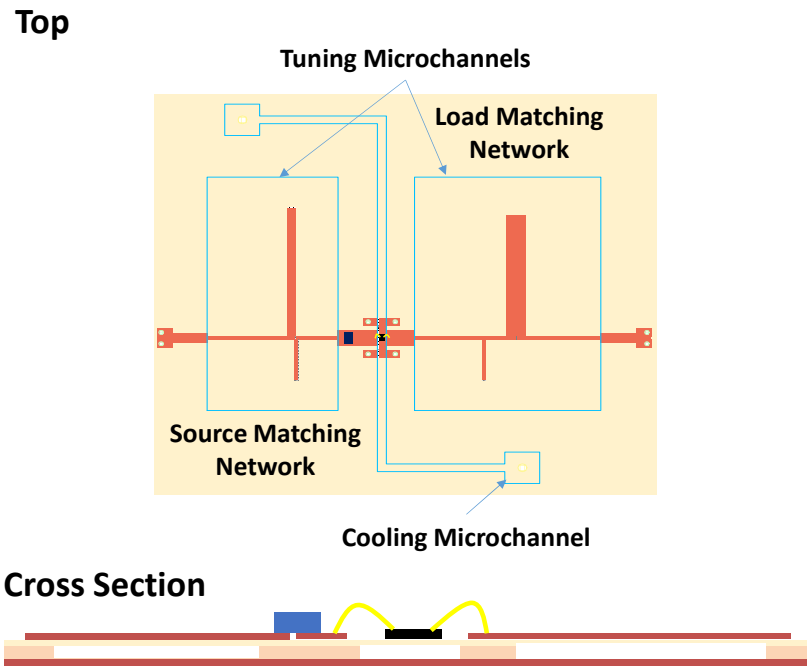

Fig. 7.8 Top and cross sectional view of the packaged PA.

7.3.2.1 Operation on acetone at f_1 = 2.4 GHz

L_1, L_2, L_3 and L_5 are designed to be 50 Ω lines on acetone at f_1. L_4 must necessarily be a λ/2 line at f_1 in order to remove the influence of M_2 while operating the tunable matching network on acetone at f_1. As M_1 is a single stub matching network, the electrical lengths E_1 and E_2 are determined by matching $Z_S(f_1)$ = 18.62+j11.12 Ω to

50 Ω, and so we have $E_1 = 45.051°$ @ f_1 and $E_2 = 47.495°$ @ f_1. Because L_3 and L_5 are 50 Ω lines and $E_4 = 180°$ @ f_1 then $Z_S(f_1)$ is fully matched to 50 Ω on acetone at f_1 using this design.

7.3.2.2 Operation on air at f_2 = 5.8 GHz

The characteristic impedance of all 50 Ω lines changes to (1+MER(50)).50 ≈ 122 Ω on air at f_2. L_5 is chosen to be a λ/4 line at f_2 and so we have $E_5 = 90°$ @ f_2. M_1 transforms $Z_S(f_2) = 50.65\text{-}j50.14\ \Omega$ to $Z'_S(f_2) = 68.290\text{-}j130.875\ \Omega$ which is then transformed by M_2 to $122^2/50 \approx 300\ \Omega$. The λ/4 line L_5 transforms 300 Ω into 50 Ω at f_2. The electrical lengths obtained are $E_3 = 2.921°$ @ f_2 and $E_4 = 151.029°$ @ f_2. As L_4 is a λ/2 line at f_1 and is part of the single stub matching network M_2 at f_2, then L_4 should satisfy two conditions at the same time: $E_4 = 180°$ @ f_1 and $E_4 = 151.029°$ @ f_2. We noticed that a solution to this problem always exists for a certain characteristic impedance Z_{04} when carefully choosing a pair (E_1, E_3). The possible number of pairs for (E_1, E_3) is four, as any given single stub matching network always offers two solutions. By using (7.40), we are looking for a characteristic impedance Z_{04} such that $MER(Z_{0_4}) = \frac{E_4(f_2)-E_4(f_1)}{E_4(f_1)} = -16.1\%$. Finally, using Fig. 7.5, the solution is found to be $Z_{0_4} = MER^{-1}(-16.1\ \%) = 26\ \Omega$.

7.4 Fabrication Procedure

Two designs were fabricated and tested: 1) the Thru-Reflect-Line (TRL) de-embedding standards + transistor die and 2) the microfluidically tunable PA. The first design was used to perform source/load pull measurements to extract optimal source and load impedances for the actual transistor die, while the second design was meant to measure the performance of the final packaged microfluidically tunable PA. The fabrication of both structures starts with a 6 in x 6 in double copper clad ULTRALAM 3850 laminate with a thickness of 2 mil. Copper is etched out from one side using nitric

acid. For the tunable PA design, vias with a diameter of 1.2 mm are drilled using a CO_2 laser. These vias serve as entry points for the different fluids and they are also useful to separate the LCP from the bottom ground after the lamination process. A 6 in x 6 in double copper clad RO3003 laminate, which is 20 mil thick, is etched out from both sides using nitric acid. Cavities are ablated on it to create the microchannels in the case of the tunable PA. These same cavities, but slightly widened, are ablated on two 6 in x 6 in bond plies (ULTRALAM 3908) which are 1 mil thick. The bottom ground of the structure is made out of a 6 mil thick copper shim. The whole stack-up is then laminated at 285 °C using a thermal press. Electron beam evaporation is used to deposit 40 nm of titanium and 1 um of gold on top of the copper. Gold is used to facilitate the bonding of the gold wires during the wire-bonding phase and also for die-attach. Alignment vias and CPW ground vias with a diameter of 22 mil are drilled from the back side. CPW vias are filled with silver epoxy and cured to create the ground connections. Samples are then cut into 3 in x 3 in samples, so four samples can be created during the same fabrication process. The top side of each one of them is then patterned using standard lithography techniques. Gold, titanium and copper are etched out subsequently using GE-8148 gold etchant, a 10:1 diluted hydrofluoric acid (HF) solution and ferric chloride respectively. For the tunable PA design, the LCP is separated from the bottom ground using a sharp needle in order to open up the cavities. 2.4 mm silicone tubes are attached to the injection vias using a commercial plastic epoxy, water flow inside the cooling microchannel is then tested using a small TCS micropump. For both designs, the GaN die is attached using indium silver, the die is then wire-bonded to the gold pads using a semi-automatic wire-bonder after curing the indium silver. A detailed fabrication flow is illustrated in Fig. 7.9, steps 3 and 6 are not part of the TRL standards fabrication.

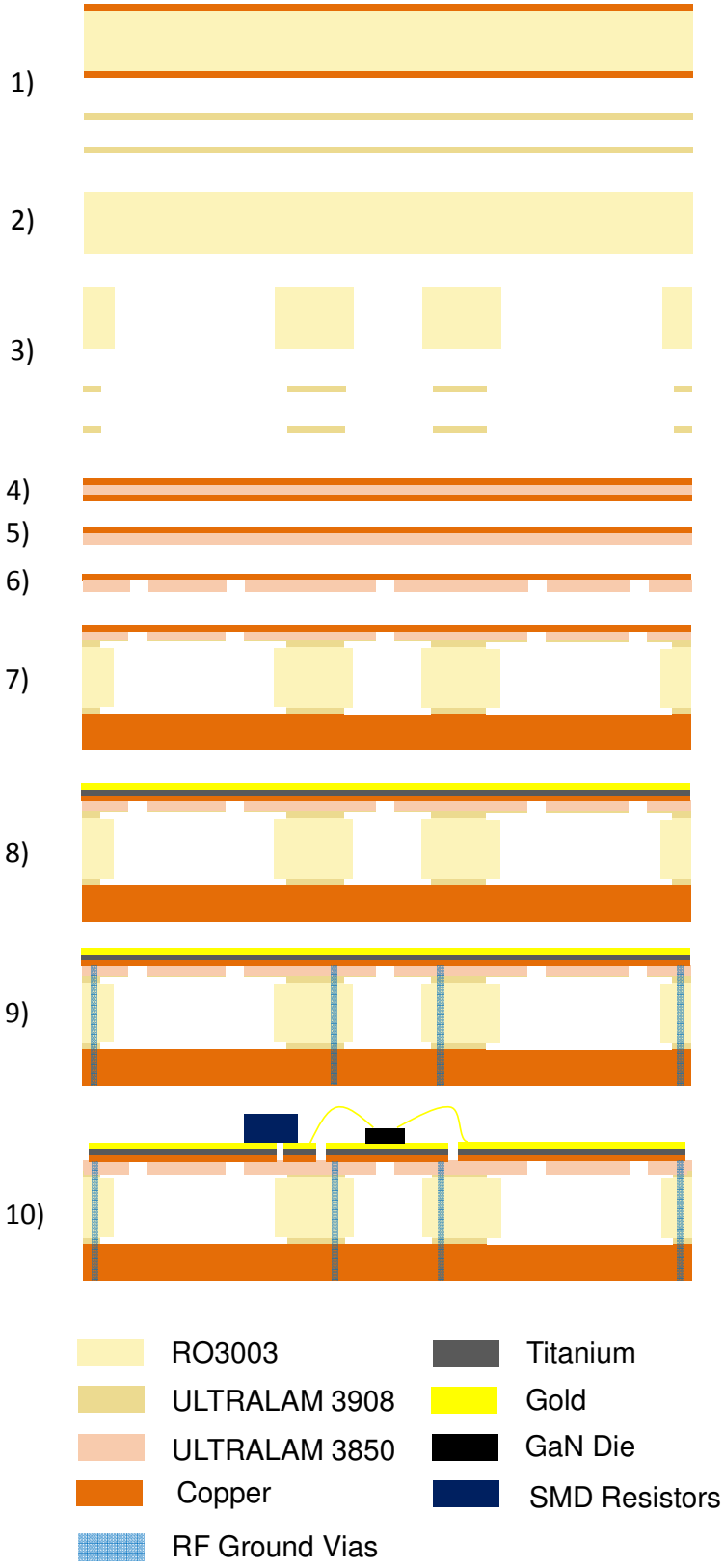

Fig. 7.9 Package fabrication flow. 1) double cladded RO3003 + two bondplies, 2) copper etching from both sides of RO3003, 3) cavity ablating on RO3003 and bondplies, 4) double cladded ULTTRALAM 3850, 5) copper etching from one side of ULTRALAM 3850, 6) drilling of injection vias, 7) lamination, 8) Ti/Au deposition, 9) drilling of RF ground vias, and 10) final micromachined structure.

Fig. 10 and Fig. 11 show pictures of both samples at each step of the fabrication process.

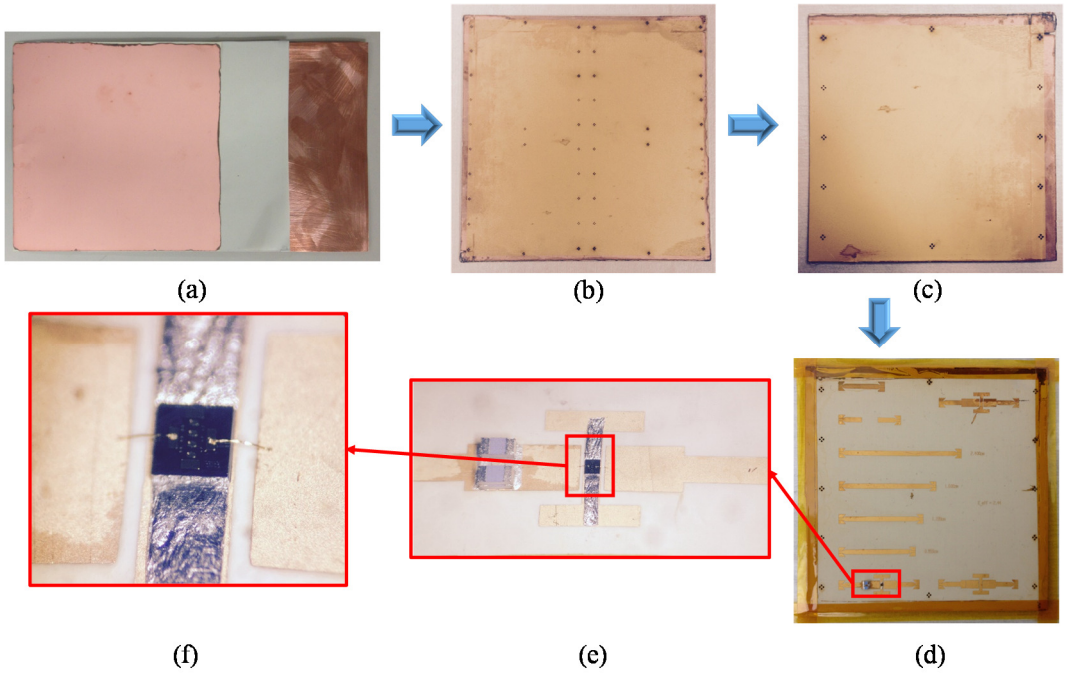

Fig. 7.10 TRL standards sample fabrication flow. a) stack-up preparation (6 in x 6 in) b) lamination + gold deposition + via drilling c) 3 in x 3 in cut sample d) top metal patterning e) zoomed DUT f) wirebonded GaN die.

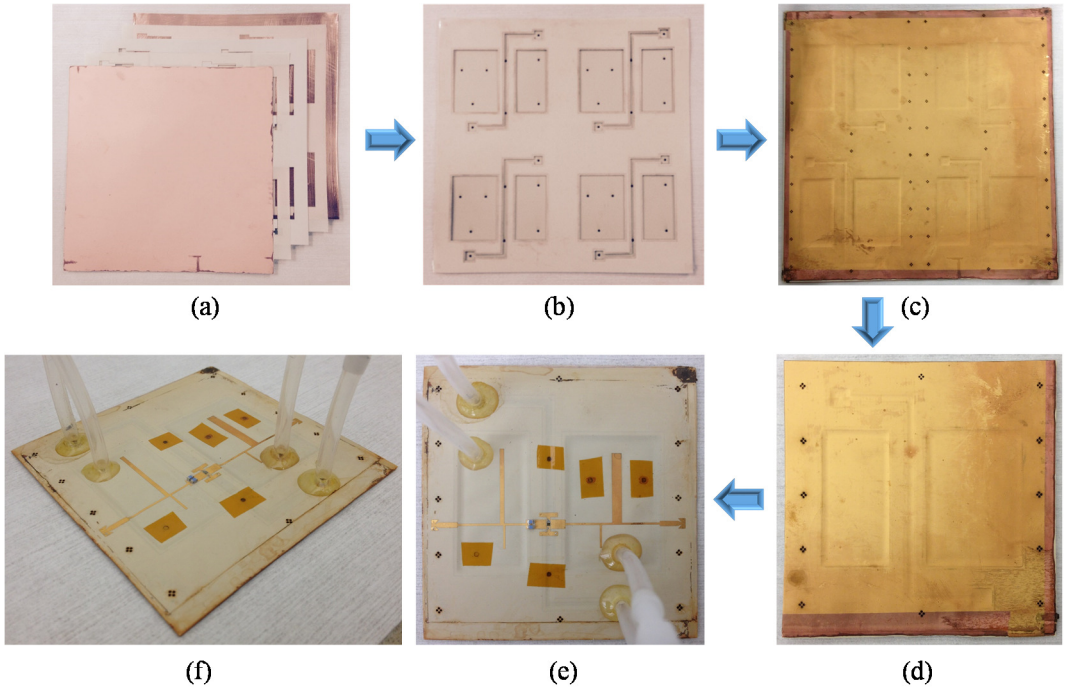

Fig. 7.11 Tunable PA sample fabrication flow. a) cavities ablating + stack-up preparation (6 in x 6 in) b) aligned layers from the back side c) lamination + gold deposition + via drilling c) 3 in x 3 in cut sample d) top metal patterning e-f) final packaged PA.

7.5 Measurements and Results

The first part of the measurements was dedicated to the characterization of the DUT, these characterizations were: effective dielectric constant extraction, TRL line de-embedding, pulsed-IV curves extraction, small signal S-parameters, load/source pull optimizations and power sweeps at optimal source and load impedances. The second part was about measuring the performance of the fully packaged tunable PA, the tests performed were: pulsed-IV and DC-IV, small signal S-parameters and 50 Ω power sweeps with air and acetone filling the tuning microchannels with or without water flow beneath the cooling microchannel.

The measurements were done using a vector-receiver load pull system. All small signal measurements were done from 1 GHz to 7 GHz and the device has been biased under class A operation for a quiescent current I_{DS} = 60 mA. The duty cycles used were either 10 % or DC/CW depending on the situation.

7.5.1 DUT Characterization

7.5.1.1 TRL Calibration and Effective Dielectric Constant Extraction

The TRL standards used were: Open, Thru and 2 GHz to 5 GHz λ/4 lines. A TRL calibration kit has been created by specifying the different line delays τ using the following equation:

$$\tau = \frac{L}{V_p} = \frac{L}{C}\sqrt{\varepsilon_{r_{eff}}} \approx 85\ ps/in \times L(in) \times \sqrt{\varepsilon_{r_{eff}}} \tag{7.41}$$

The extraction of the effective dielectric constant was done with the aid of a tool called “StatistiCAL Plus” from “NIST”. The estimated and measured $\varepsilon_{r_{eff}}$ is shown in Fig. 7.12. The figure shows that the estimated value (2.44) is very close to the average measured value (2.437) between 1 GHz and 9 GHz.

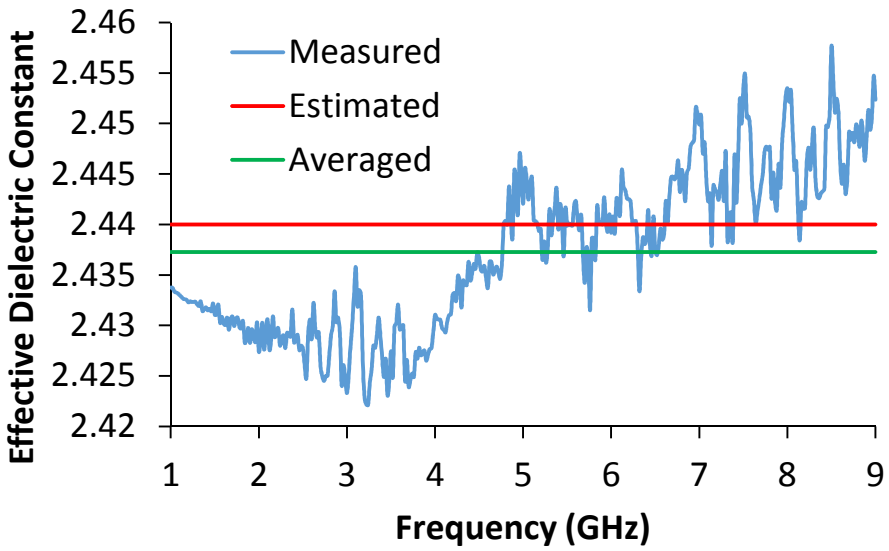

Fig. 7.12 Effective dielectric constant extraction.

To make sure that the fabricated standards are 50 Ω quarter-wave lines, the standards are measured and de-embedded using the TRL calibration method. The de-embedded measurements of the standards are then compared to simulation. To get meaningful comparison plots, a mismatch is introduced at the simulation ports such that the S-parameters are normalized to 30 Ω (it is important to do so when the characteristic impedance of the line is very close to the impedance of the simulation ports). However, 50 Ω S-parameters are also provided to get an idea about the measured return and insertion loss of the different lines. The results in Fig. 7.13, Fig. 14, Fig. 15 and Fig. 16 show a good agreement between measured data and simulations. Based on the return loss of the different lines, it can be seen that the characteristic impedance of the lines is very close to 50 Ω. Also, the phase information indicates that the lines have an electrical length of 90° at their respective design frequencies.

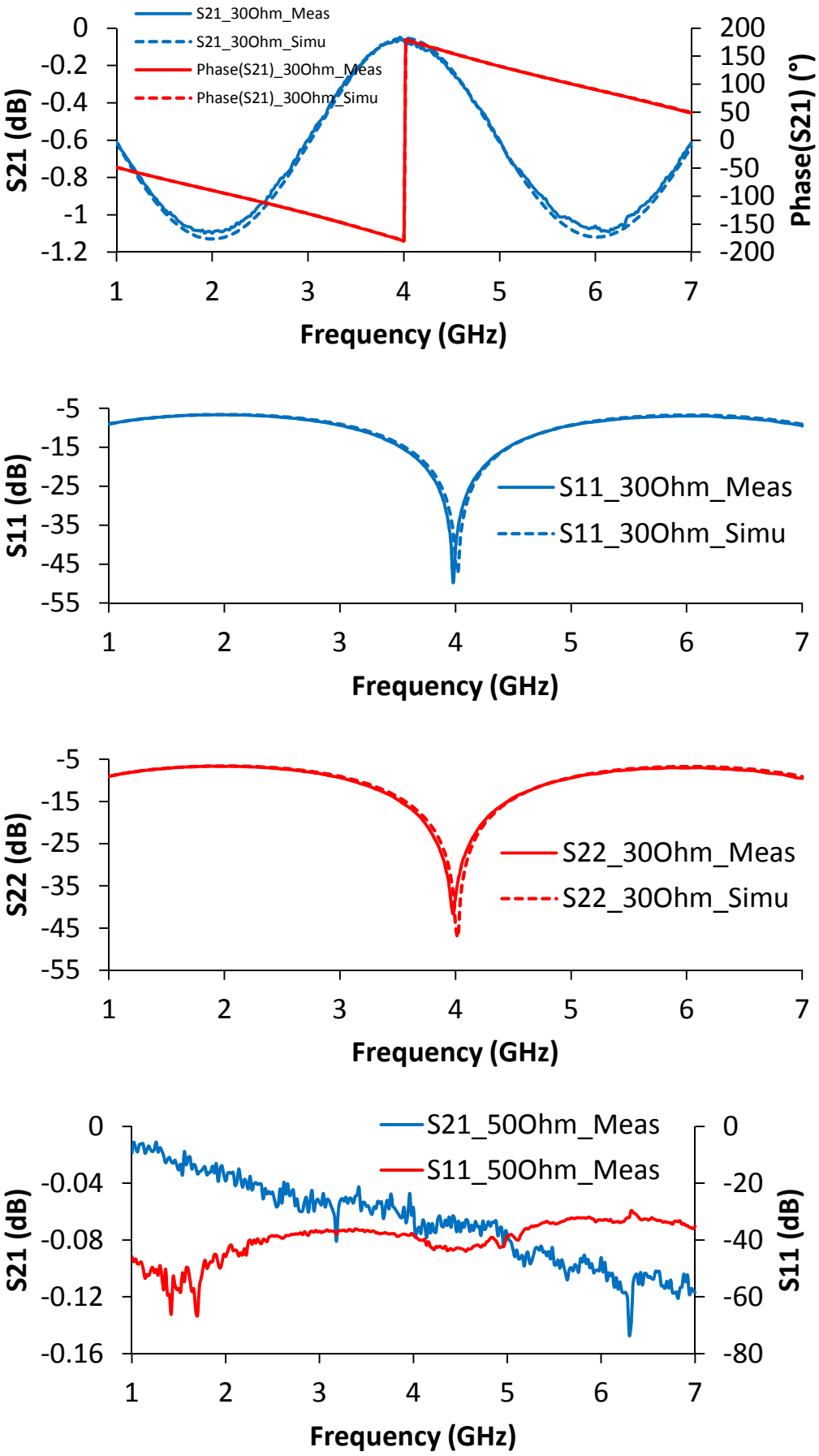

Fig. 7.13 2 GHz line S-parameters measurements and simulations.

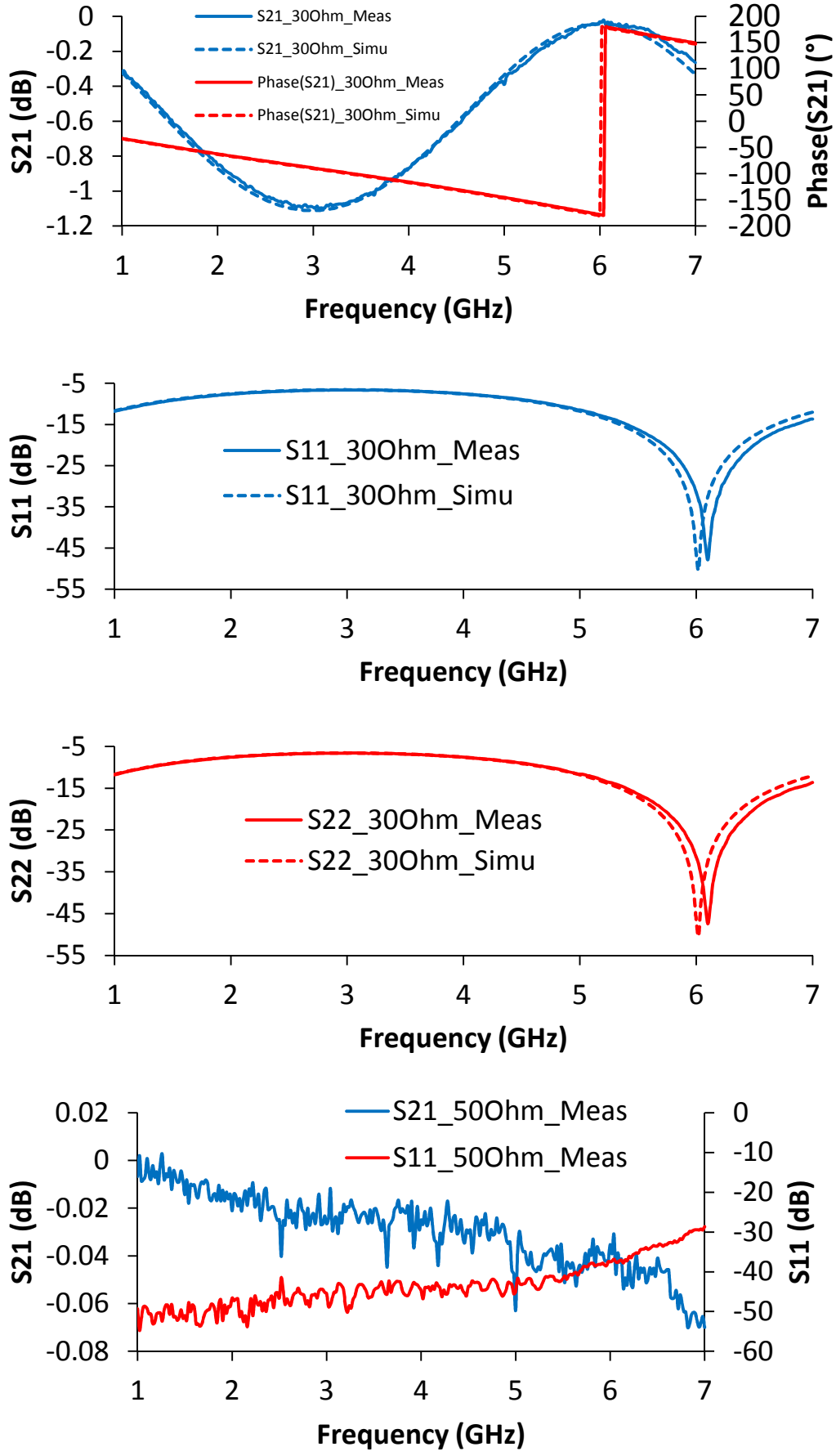

Fig. 7.14 3 GHz line S-parameters measurements and simulations.

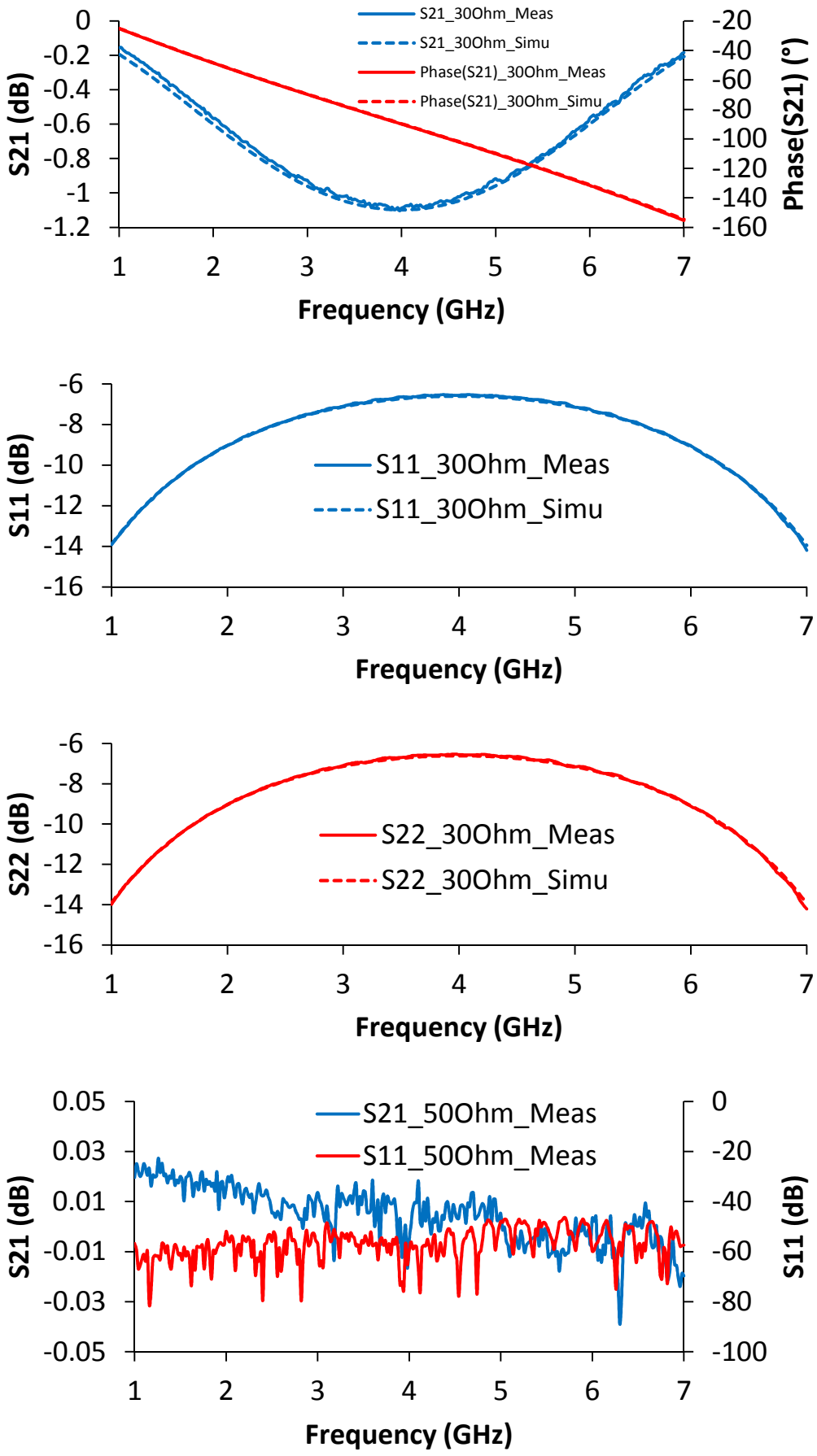

Fig. 7.15 4 GHz line S-parameters measurements and simulations.

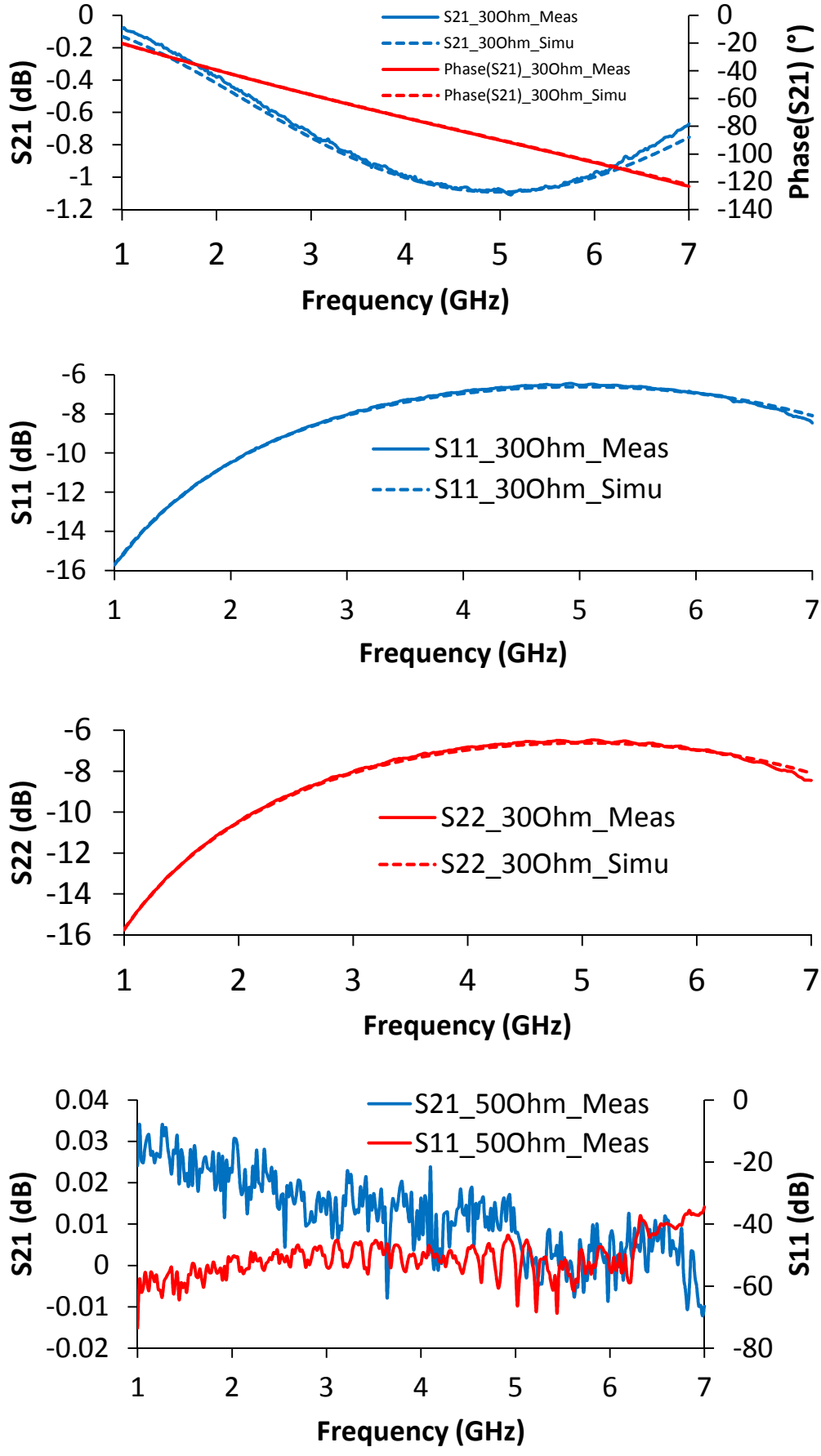

Fig. 7.16 5 GHz line S-parameters measurements and simulations.

7.5.1.2 I-V Curves and Small Signal S-Parameters

The following step was to measure the pulsed-IV characteristics of the GaN die. Fig. 7.17 shows the pulsed-IV curves of the die where V_{GS} and V_{DS} were swept from -2.6 V to -2.36 V and from 0 V to 40 V respectively with a duty cycle of 10 %. The small signal S-parameter measurement and simulation of the DUT is shown in Fig. 7.18. The inductance values assigned to model the wirebonds and the ground vias were tuned to match the simulation with the measurements. The value for the input inductance and the output inductance were set to 0.58 nH and 0.7 nH respectively while the ground inductance was set to 0.32 nH.

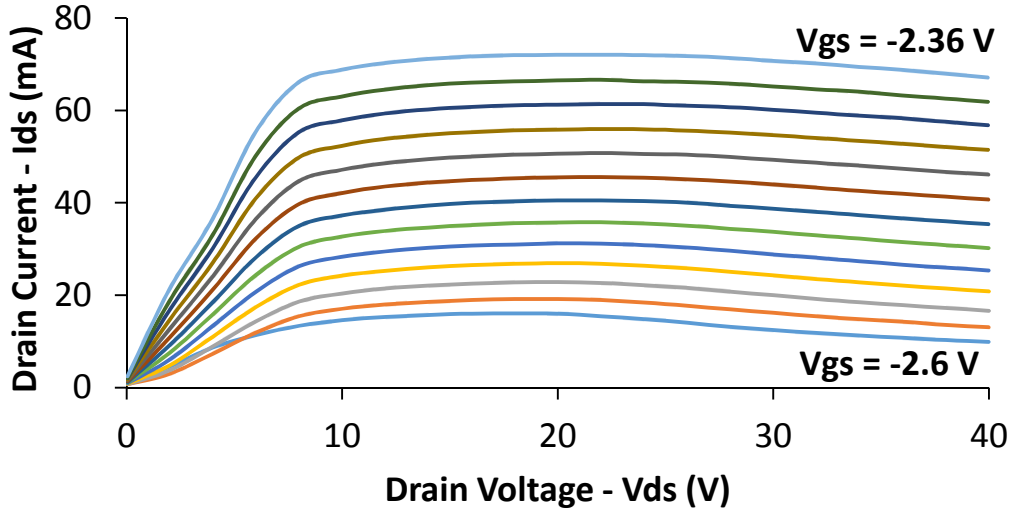

Fig. 7.17 DUT pulsed-IV curves.

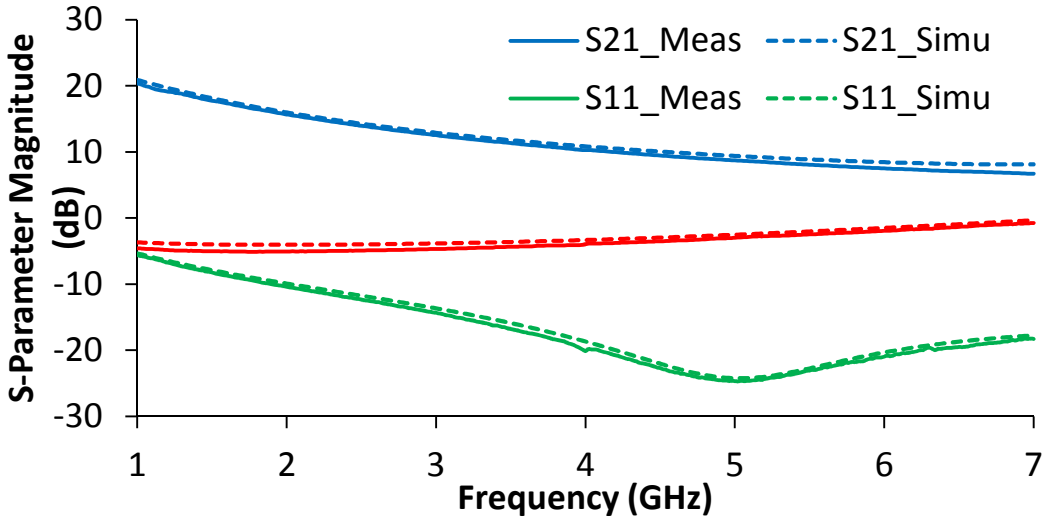

Fig. 7.18 DUT small signal S-parameter measurements and simulations.

7.5.1.3 Load/Source Pull Optimizations and Large Signal Power Sweeps

The large signal characterization was done at 2.4 GHz for P_{in} = 25 dBm and at 5.8 GHz for P_{in} = 28 dBm. The goal was to get the best trade-off between P_{out} and PAE. Fig. 7.19 and Fig. 7.20 are a comparison between simulated and measured P_{out} and PAE contours. Table 7.1 is a summary of the obtained results which shows once again a good correlation between simulations and measurements. The large signal power sweeps were performed at 2.4 GHz and 5.8 GHz at their respective optimal source and load impedances, the results are shown in Fig. 7.21 and Fig. 7.22.

It can be noted that the large signal measurements at 2.4 GHz in Fig. 7.21 are very close to the simulated values, however the measurements at 5.8 GHz in Fig. 7.22 show some unstable behavior for low input power levels but soon start to behave normally for input power levels greater than 24 dBm. As our goal was to optimize the PA at P_{in} = 28 dBm, that did not cause any issues with the designs later on.

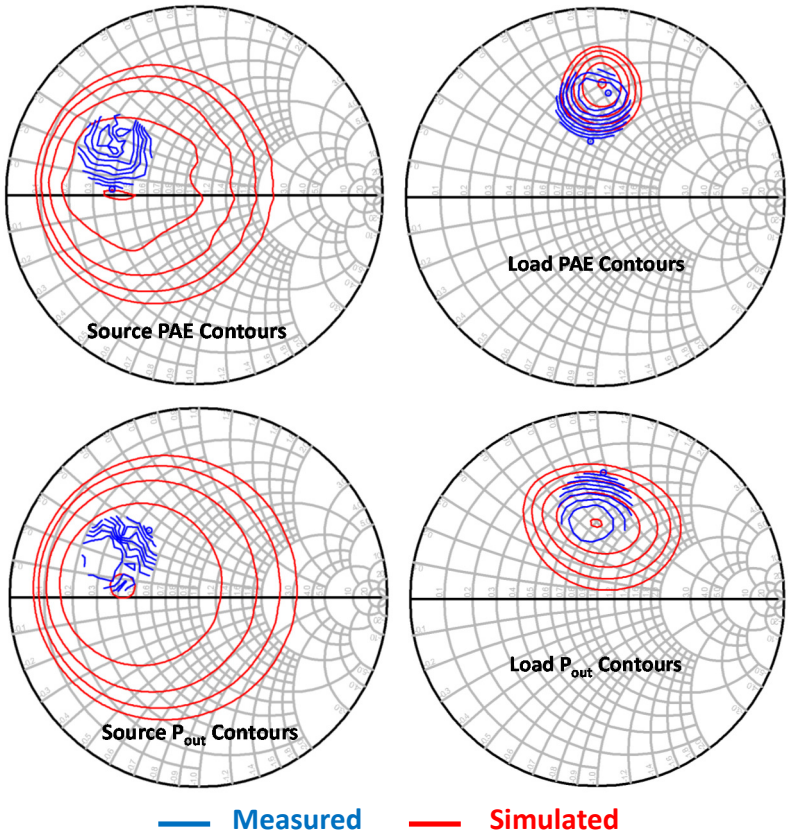

Fig. 7.19 P_{out} and PAE contours for the DUT at 2.4 GHz.

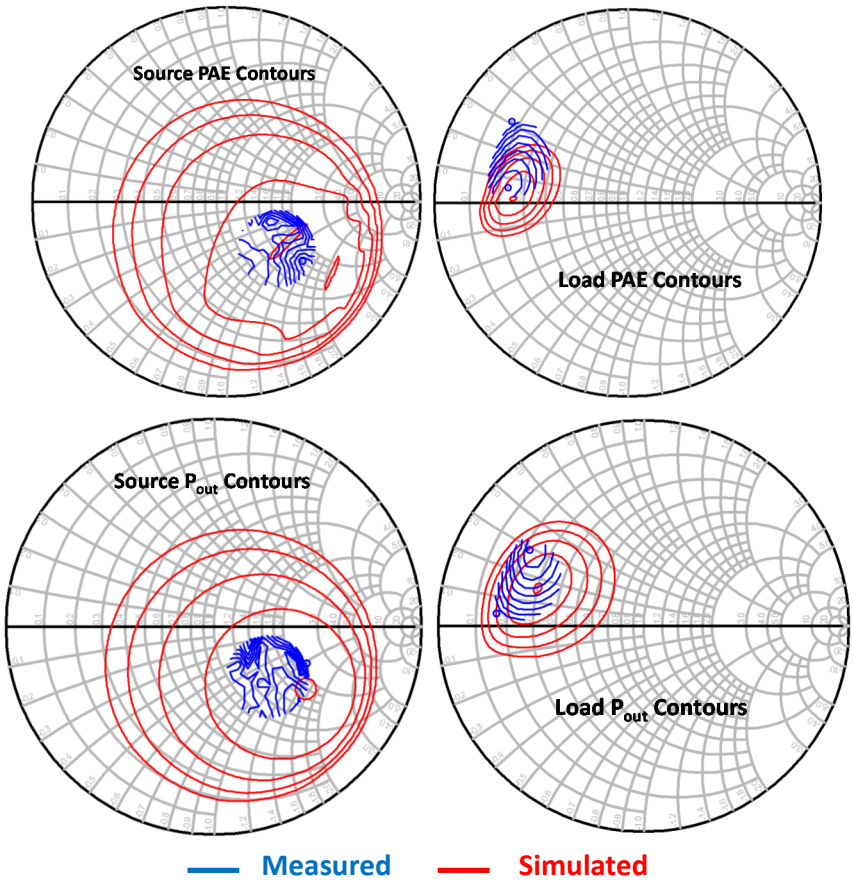

Fig. 7.20 P_{out} and PAE contours for the DUT at 5.8 GHz.

TABLE 7.1
LOAD AND SOURCE PULL RESULTS

Frequency (GHz)	2.4		5.8	
P_{in} (dBm)	25		28	
	Simulated	Measured	Simulated	Measured
$Z_{S,\,Opt}$ (Ω)	21.33+j2.24	18.62+j11.12	50.64-j50.10	50.65-j*50.14
$Z_{L,\,Opt}$ (Ω)	30.48+j41.56	30.24+j37.74	11.97+j7.73	11.96+j*8.46
Max. PAE (%)	59.07	60.56	49.51	46.85
Max. P_{out} (dBm)	38.25	38.27	37.33	37.11

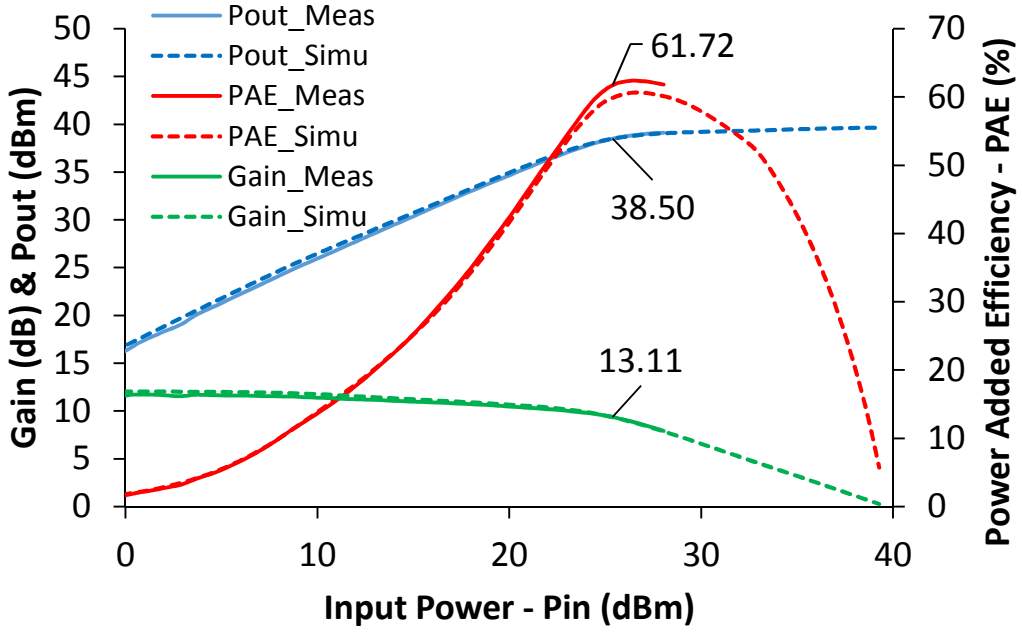

Fig. 7.21 DUT large signal power sweep at 2.4 GHz.

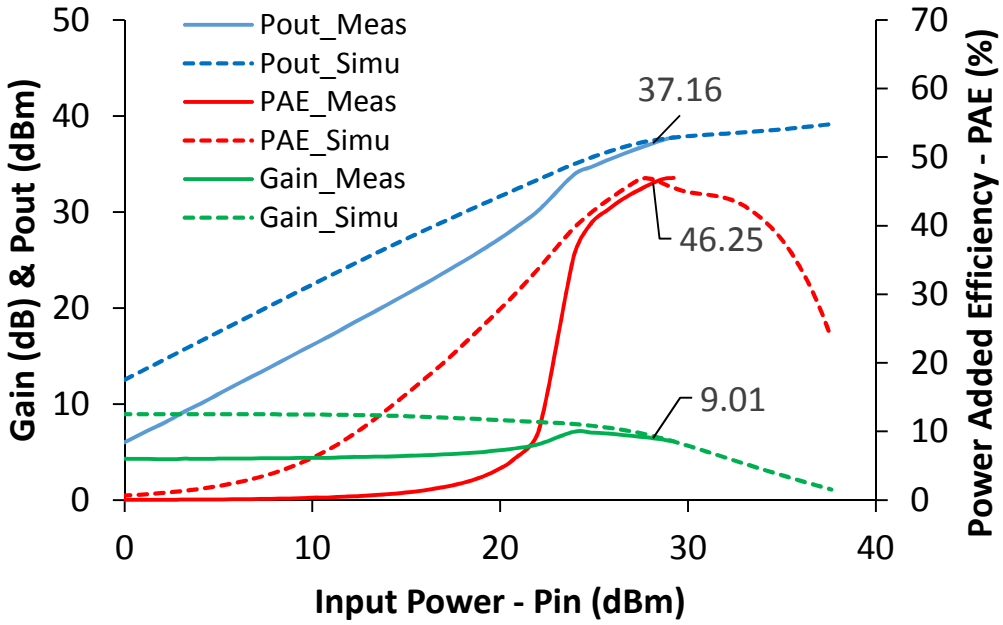

Fig. 7.22 DUT large signal power sweep at 5.8 GHz.

7.5.2 Tunable PA Characterization

Every attempt to bias the assembled microfluidically tunable PA on organics was unexpectedly unsuccessful. The I-V curves would always exhibit a random behavior whenever the device was biased even at very low current levels and very low duty cycles. At the same time, thanks to different troubleshooting tests, we were able

to determine that the origin of the problem was not a thermal issue but rather an instability issue. Though, we have still been unable to figure out exactly what could be causing the instability. The explanation for that could be that the device is sitting on top of a cavity with two metals and a dielectric in between with four ground vias connecting the two metals which could potentially create an instability or excite some undesirable EM modes. To at least demonstrate the feasibility of this study, we have decided to cut the fabricated matching networks and attach them to a micromachined copper carrier with integrated microchannels inside the copper. This is of course far from ideal, as the copper is already an excellent conductor and the overall weight of the system is affected, but this at least shows that the idea of combining tuning and cooling for a GaN-based PA is possible. Once the instability issue is solved, this solution can be easily replicated on organics. Fig. 7.23 shows the copper-based tunable PA and the one on organics ready to be measured.

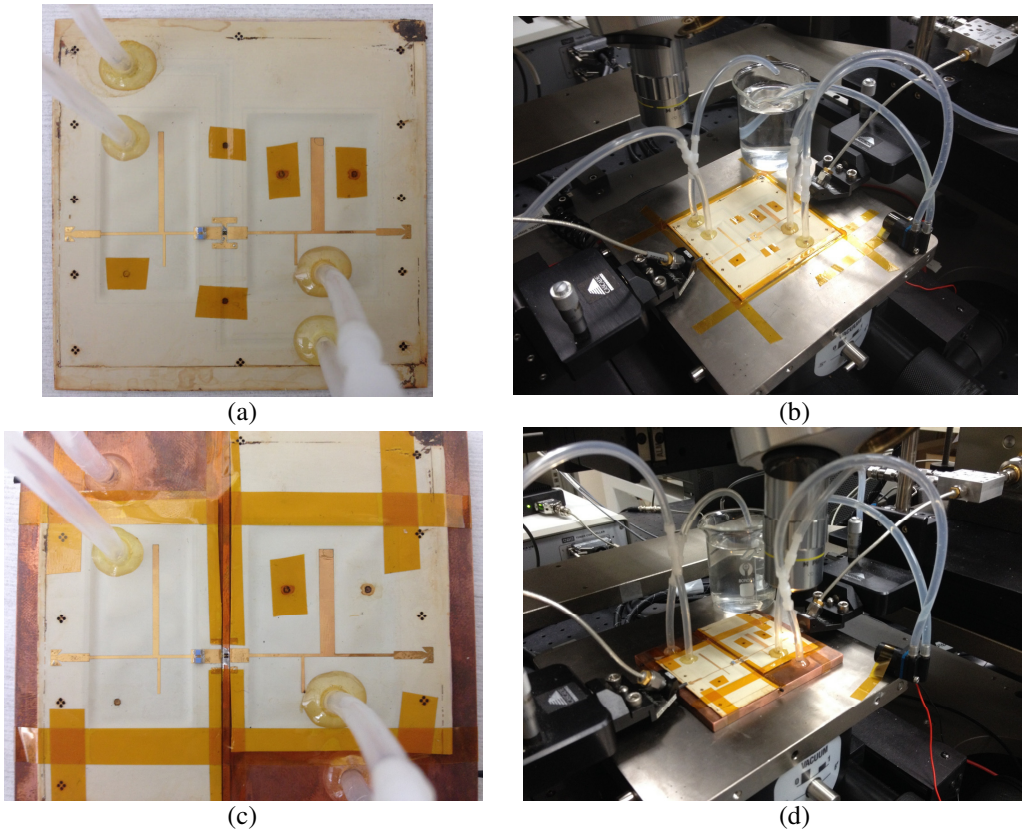

Fig. 7.23 a) Tunable PA on organics b) Organic PA ready to measure c) Tunable PA on micromachined copper d) Copper-based PA ready to measure.

7.5.2.1 I-V Curves and Small Signal S-Parameters

I-V curves were extracted with a duty cycle of 10 % (Fig. 7.24) and 100 % (Fig. 7.25). V_{GS} was swept from -2.6 V to -2.26 V while V_{DS} was swept from 0 V to 40 V. Small signal S-parameters were also extracted for two cases where: 1) acetone is filling the matching networks (Fig. 7.26) and 2) air is filling the matching networks (Fig. 7.27).

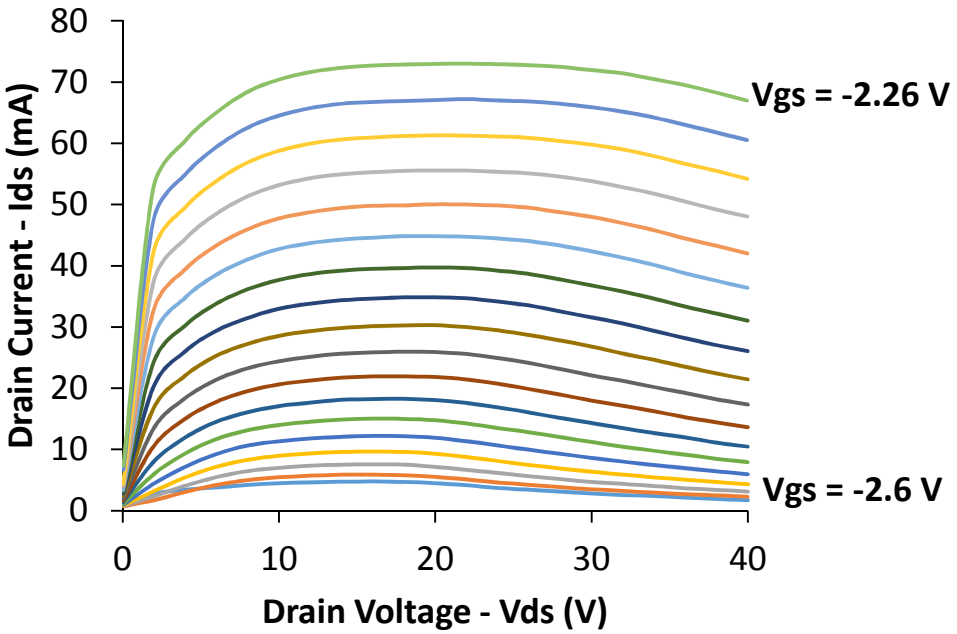

Fig. 7.24 DUT I-V curves, 10 % duty cycle.

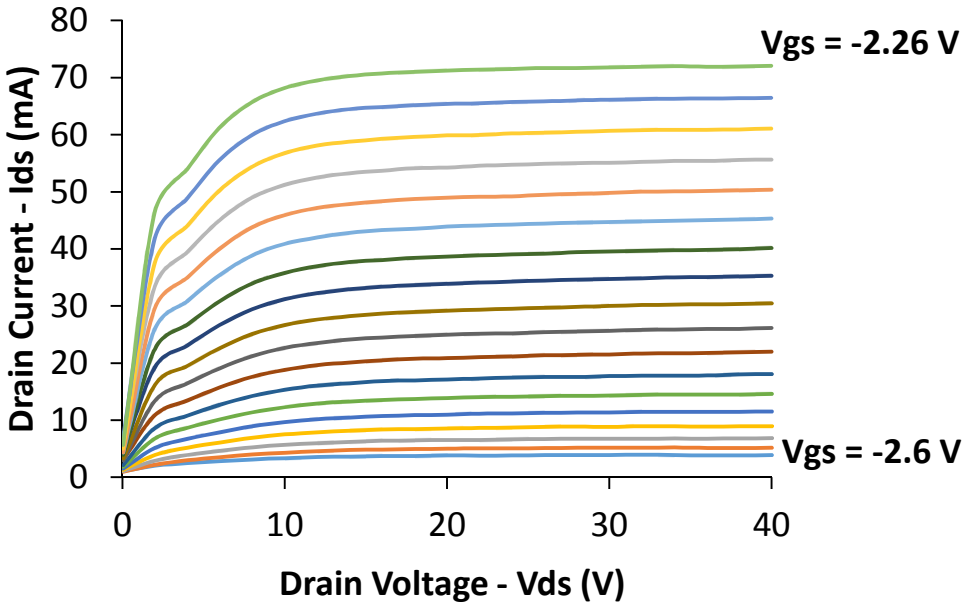

Fig. 7.25 DUT I-V curves, DC.

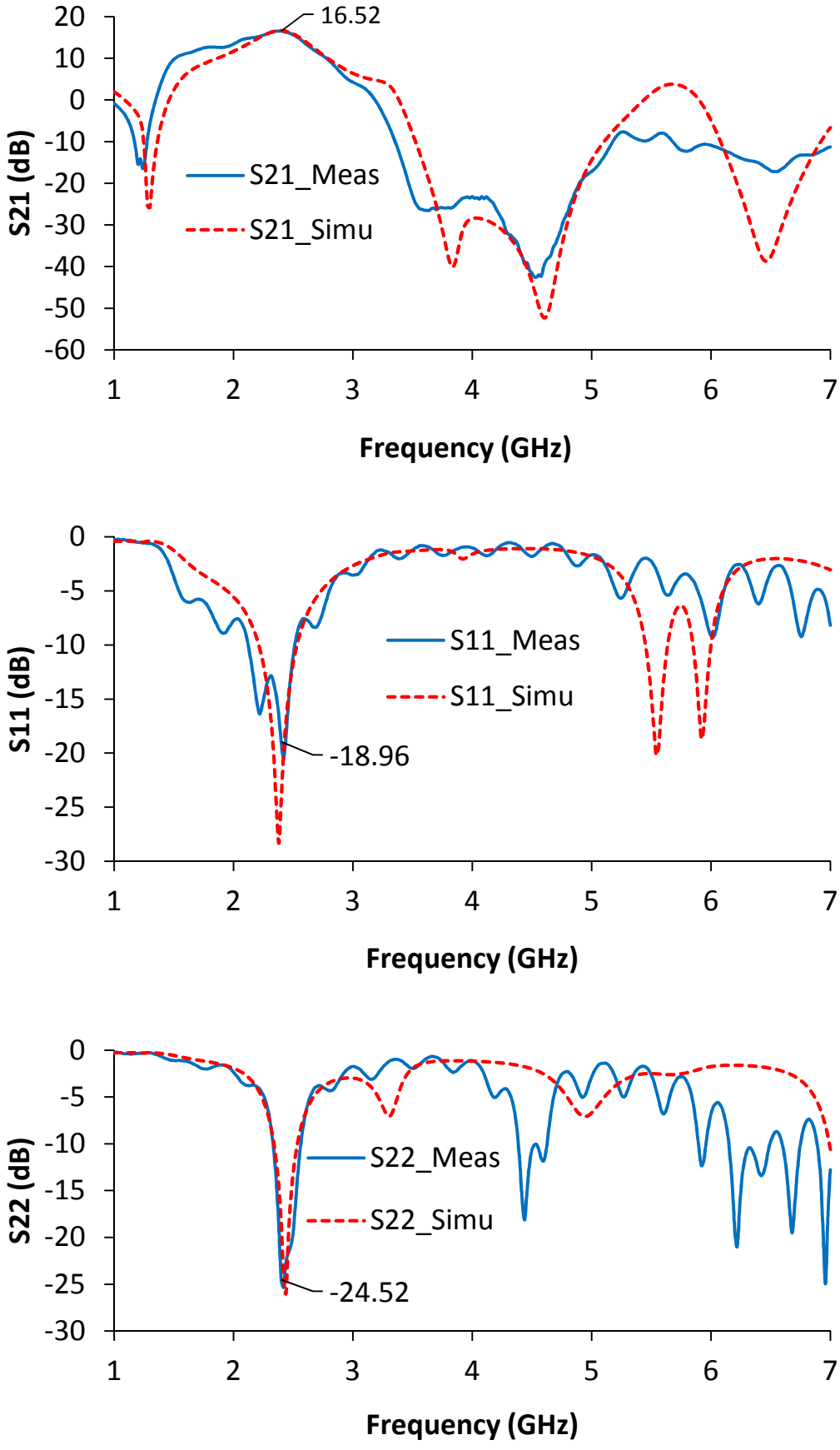

Fig. 7.26 Small signal S-parameters with acetone filling the tuning matching networks.

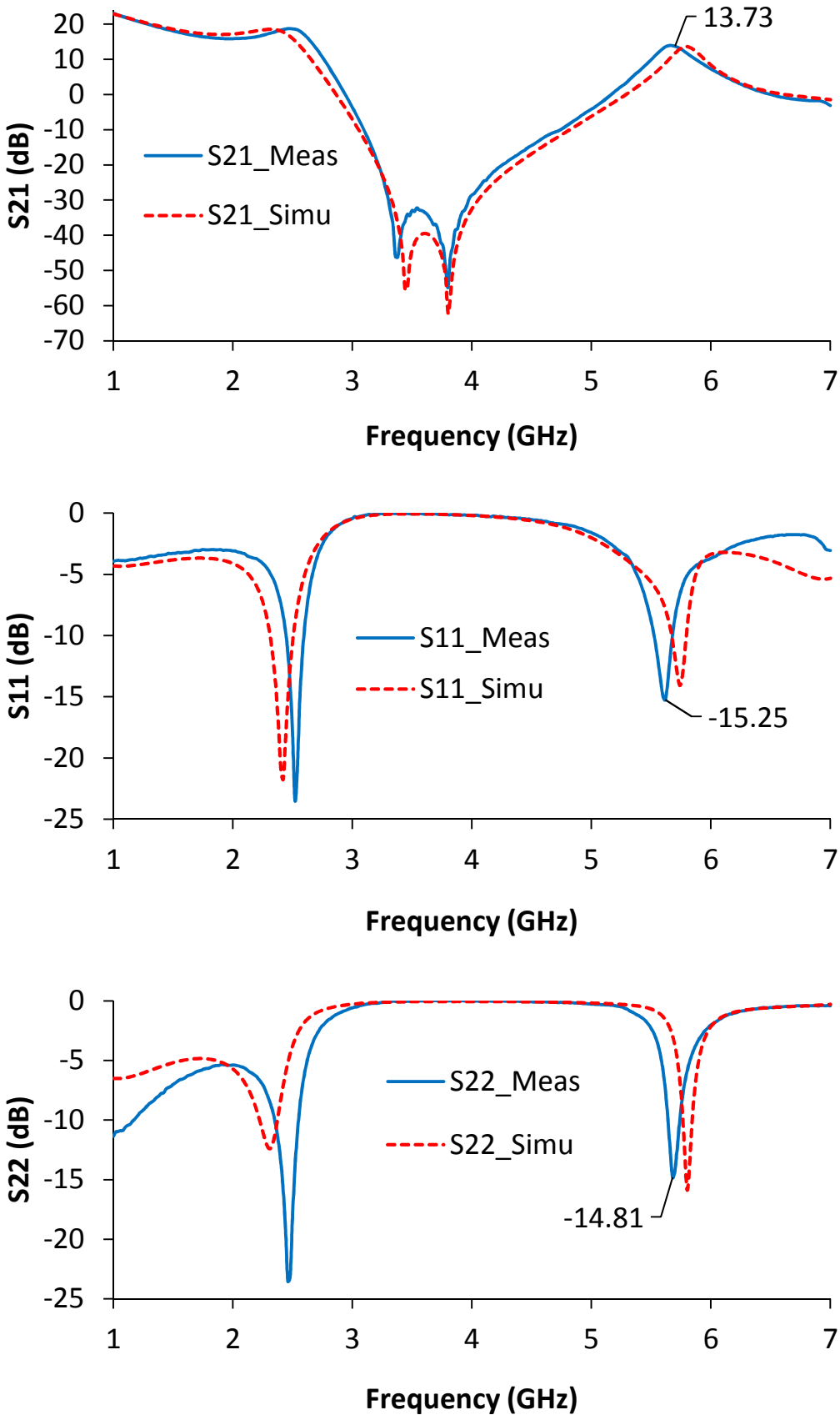

Fig. 7.27 Small signal S-parameters with air filling the tuning matching networks.

7.5.2.2 *Large Signal Power Sweeps*

Power sweeps (Fig. 7.28 and Fig. 7.29) were performed on the copper-based PA while varying the following parameters: 1) the fluid inside the tuning microchannels, 2) the flow inside the cooling microchannel and 3) the duty cycle. In the case where the flow of water inside the cooling microchannel did not bring any improvement to the electrical performance, some plots were omitted or grouped into a single curve. From the results, it seems that the water flow does not affect the performance for the 2.4 GHz measurements. Moreover, it does not affect much the output power, but it starts to have some influence on the PAE for the 5.8 GHz measurements where a 1.5 % increase in PAE is noticed at 28 dBm input power compared to the non-flow case. On the other hand, the effect of reducing the duty cycle improves drastically the PAE in all cases. Finally, the performance obtained at 10 % duty cycle without water flow with 1) acetone at 2.4 GHz is: PAE = 33.88 % and P_{out} = 37.13 dBm = 5.16 W and 2) air at 5.8 GHz is: PAE = 51.10 % and P_{out} = 37.87 dBm = 6.12 W.

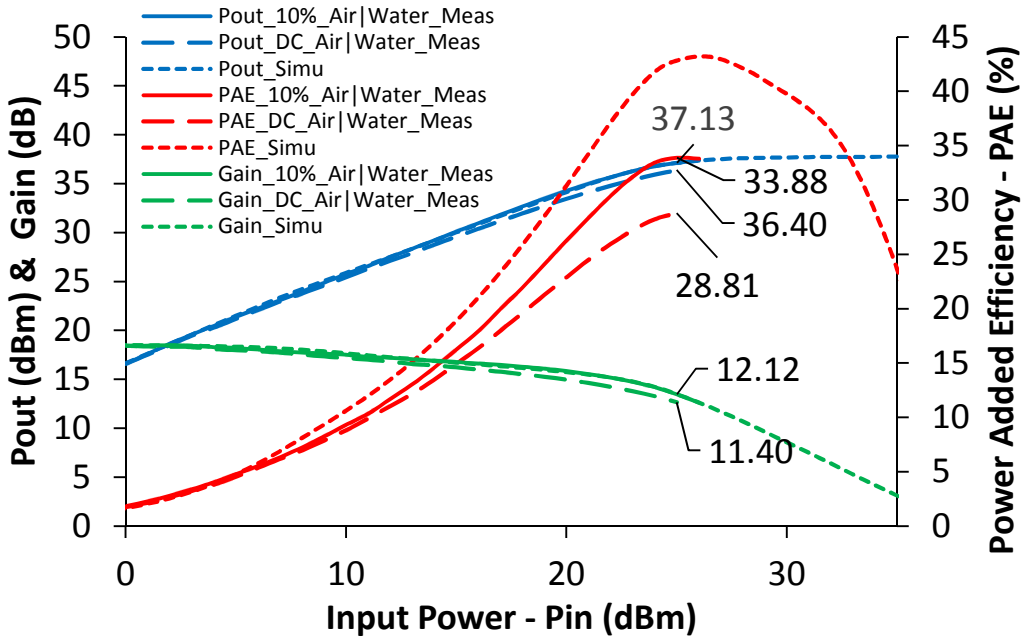

Fig. 7.28 Tunable PA large signal power sweep at 2.4 GHz.

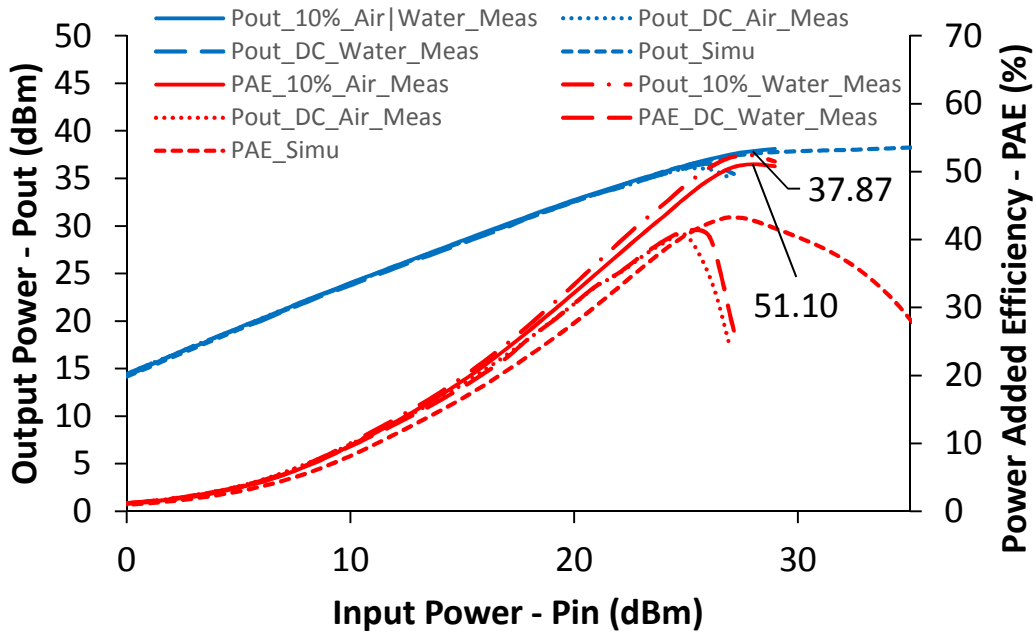

Fig. 7.29 Tunable PA large signal power sweep at 5.8 GHz.

7.6 Summary

In this chapter, multilayer microstrip design techniques have been discussed and new equations have been developed for an accurate extraction of the effective dielectric constant and the characteristic impedance of microstrip lines on multilayer dielectric substrates. Tunability parameters have been introduced for the first time and have served to design the microfluidically tunable matching networks which in turn were used as the building blocks of the microfluidically tunable PA. A detailed fabrication flow of the PA on organics have been described thoroughly. Moreover, measurements and simulations have been provided and compared with each other for small signal S-parameters, for de-embedding, for load/source pull optimizations and for large signal power sweeps. The PA on organics did not work as expected and was replaced by a copper-based PA where cooling microchannels have been integrated into the copper. It was observed that water flow slightly affected the PAE in some cases but did not have an influence on P_{out}. Solving the instabilities of the GaN die on top of the organic package could potentially lead to satisfactory results in the future.

CHAPTER 8

CONCLUSION

This thesis has explored the design and implementation of a low cost integrated microfluidic solution on multilayer organic substrate for cooling and tuning RF circuits. In this chapter, the main contributions are highlighted and recommendations are given with regards to potential further research in this subject. The author's publications are given as a reference at the end.

8.1 Contributions

Below are the contributions presented in this thesis:

1. For the first time, a 1 W GaN HEMT has been attached and characterized electrically and thermally on LCP. Microchannels have been used for the first time to achieve this objective.
2. For the first time, a complete general thermal model of a packaged heat source has been thoroughly described. The analysis of this simple model yielded many important results on how to construct and understand power derating curves, and how to extract important information about the heat sink specifications for efficient cooling at maximum power rating levels.
3. For the first time, high power devices have been tested on multilayer organics with integrated microfluidic channels. Two types of devices have been characterized: passive and active. Passive elements were high power surface mount thin film resistors up to 40 W rated power at 100°C. The active element was a 5 W GaAs pHEMT operated under DC and RF regimes.
4. Thermal modeling of the proposed microfluidic solution has been elaborated by combining different existing thermal models in literature. The thermal model has been used to predict the steady state junction temperature of a heat source

on top of a microchannel where a fluid can either be static or dynamic. This model has been verified by real thermal measurements of high power resistors. The measurements showed that the 40 W rated power resistor could be operated at 23 W with fluid circulation. This is, to the best of the author's knowledge, the best result ever achieved on multilayer organic substrates.

5. For the first time, practical guidelines on how to design microchannels on organic substrates have been presented for cooling purposes. An approximate design equation has also been developed to determine the best suitable thickness for the microchannels for the static and the dynamic cases.
6. For the first time, an L-band RF microstrip bandpass filter has been tuned on LCP using integrated microfluidics. A combination of DI water/acetone was used interchangeably inside the microchannels. 50 % tuning was achieved at 1 GHz. The insertion and return loss were excellent as well.
7. For the first time, microfluidics have been used on organics to tune a GaN-based PA. Fluids used were air and acetone in order to shift the frequency of operation of the PA from 2.4 GHz to 5.8 GHz. Simulations and measurement were in good agreement, the PA averaged a 40 % PAE and 36 dBm output power over the two bands.
8. Design equations on a multilayer dielectric substrate have been gathered and improved. A synthesis algorithm has been given to synthesize the microstrip line dimensions on a multilayer substrate. Based on transmission line theory, equations have been developed to accurately extract the characteristic impedance Z_0 and the effective dielectric constant ε_{reff} of a microstrip line by only using the return loss of a simulated microstrip line under ADS. The motivation behind developing this converging algorithm was to bypass the lack

of microstrip dispersion models in literature in the case of multilayer dielectric substrates.

9. For the first time, the "tunability parameters" (MIR and MER) concept has been developed and explained, all backed-up by theory and equations. A novel design approach has been explained with regards to the design of microfluidically tunable matching networks. A step-by-step guideline and design equations have also been presented.
10. For the first time, microfluidic channels have been combined in a single integrated package to cool and tune an RF PA at the same time.

8.2 Future Work

The results of this doctoral research are paving the way for some exciting new directions that could be investigated in the future. Below are some thoughts:

1. The multilayer thermal model used to characterize the proposed microfluidic solution can be improved to work for smaller heat source sizes. The real measurements could also be improved by sweeping other design parameters such as the thickness of the LCP layer, the overall size of the microchannel, the fluid flow rate… Moreover, the model only gives an idea about the steady state temperature of a heat source under a continuous excitation regime, so future work can potentially look into how to obtain transient thermal information when a heat source is used in a pulsed regime. Frequency dependent heat sources could be used to validate the transient response. Finally, only the size of passive heat sources has been changed, so this idea could be extended to active elements as well.
2. In this work, a single microchannel has been used to cover a single heat source. It could be interesting to investigate the effect of having multiple smaller

microchannels beneath one single heat source and compare the performance in the two scenarios. In addition, an array of heat sources and microchannels could be investigated, the study could include the thermal effects of having closely placed heat sources.

3. The fabrication process could be modified to extend the usage of this microfluidic solution to cooling heat sources while the coolant is in direct contact with the device. This would allow a better heat dissipation in some cases, and would make this solution work for other transmission line technologies such as strip lines.
4. The tunable matching network presented in this work relied on one single microchannel beneath the whole microstrip circuit, further investigations could focus on how to selectively place smaller microchannels behind "key" lines that highly affect the tunability of the circuit.
5. An automatic fluid distribution system can be designed and implemented to show the commercial potential of these tuning microchannels. Replacing the fluids in this work has always been done manually. Moreover, other fluid combinations could be investigated in order to minimize the dielectric loss of the RF circuits especially at higher frequencies, which, in turn, would open up the door for some interesting applications. Furthermore, the design and implementation of a microfluidically tunable transmission module including tunable filters, tunable antennas and tunable PAs could be a very promising idea. Finally, extending the tunability solution to other technologies like CPW and strip lines is something to bear in mind as well.

8.3 Publications to Date

The following is a chronological list of papers that have been submitted and accepted by a peer-reviewed conference or journal for publication:

8.3.1 Journal Papers

1. **O. Lemtiri Chlieh**, W. T. Khan and J. Papapolymerou, "Thermal Modeling of Microfluidic Channels for Cooling High Power Resistors on Multilayer Organic Liquid Crystal Polymer Substrate," *ASME Journal of Electronic Packaging*, Vol. 137, No. 3, p. 031009, September 2015.
2. S. Hu, S. Kousai, J. S. Park, **O. Lemtiri Chlieh** and H. Wang, "Design of A Transformer-Based Reconfigurable Digital Polar Doherty Power Amplifier Fully Integrated in Bulk CMOS," *IEEE Journal of Solid-State Circuits*, Vol. 50, No. 5, pp. 1094-1106, April 2015.

8.3.2 Conference Papers

1. **O. Lemtiri Chlieh**, C. A. Donado Morcillo, S. Pavlidis, W. T. Khan and J. Papapolymerou, "Integrated Microfluidic Cooling for GaN Devices on Multilayer Organic LCP Substrate," *IEEE International Microwave Symposium (IMS)*, Seattle, Washington, USA, June 2013.
2. **O. Lemtiri Chlieh**, W. T. Khan and J. Papapolymerou, "L-Band Tunable Microstrip Bandpass Filter on Multilayer Organic Substrate With Integrated Microfluidic Channel," *IEEE International Microwave Symposium (IMS)*, Tampa, Florida, USA, June 2014.
3. **O. Lemtiri Chlieh**, W. T. Khan and J. Papapolymerou, "Integrated Microfluidic Cooling of High Power Passive and Active Devices on Multilayer Organic Substrate," *IEEE International Microwave Symposium (IMS)*, Tampa, Florida, USA, June 2014.
4. **O. Lemtiri Chlieh**, W. T. Khan and J. Papapolymerou, "Microfluidically Reconfigurable GaN Power Amplifier on Multilayer Organic Substrate for S-Band and C-Band Applications," *IEEE International Microwave Symposium (IMS)*, Phoenix, Arizona, USA, May 2015.

5. G. C. Barisich, S. Pavlidis, C. A. Donado Morcillo, **O. Lemtiri Chlieh** and J. Papapolymerou, "An X-band GaN HEMT Hybrid Power Amplifier with Low-loss Wilkinson Division on AlN Substrate," *The International IEEE Conference on Microwaves, Communications, Antennas and Electronic Systems (COMCAS)*, Tel Aviv, Israel, October 2013.

6. A. L. Vera López, D. B. Giles, W. T. Khan, **O. Lemtiri Chlieh**, G. E. Ponchak and J. Papapolymerou, "Microfluidic Channel on Organic Substrates as Size Reducing Technique for 915 MHz Antenna Designs," *Asia Pacific Microwave Conference (APMC)*, Seoul, South Korea, November 2013.

7. S. Pavlidis, A. C. Ulusoy, W. T. Khan, **O. Lemtiri Chlieh**, E. Gebara and J. Papapolymerou, "A Feasibility Study of Flip-Chip Packaged Gallium Nitride HEMTs on Organic Substrates for Wideband RF Amplifier Applications," *IEEE Electronic Components and Technology Conference (ECTC)*, Lake Buena Vista, Florida, USA, May 2014.

8. S. Hu, S. Kousai, J. S. Park, **O. Lemtiri Chlieh** and H. Wang, "A +27.3dBm Transformer-Based Digital Doherty Polar Power Amplifier Fully Integrated in Bulk CMOS," *IEEE Radio Frequency Integrated Circuits Symposium (RFIC)*, Tampa, Florida, USA, June 2014.

REFERENCES

[1] G. Chien and K. L. Loh, "Past, present and Future of RF Design in Wireless Communication," *International Symposium on VLSI Design, Automation and Test (VLSI-DAT)*, April 2009.

[2] B. Green, *et al.*, "GaN RF Device Technology and Applications, Present and Future," *IEEE Bipolar/BiCMOS Circuits and Technology Meeting (BCTM)*, September 2013.

[3] M. M. Tentzeris, *et al.*, "3-D-Integrated RF and Millimeter-Wave Functions and Modules Using Liquid Crystal Polymer (LCP) System-on-Package Technology," *IEEE Transactions on Advanced Packaging*, Vol. 27, No. 2, pp. 332-340, May 2004.

[4] S. Wenquan and L. Tongyi, "High-Speed Mixed-Signal SoC Design for Basestation Application," *IEEE Asia Pacific Conference on Circuits and Systems (APCCAS)*, December 2008.

[5] R. W. T. Ng, *et al.*, "Ultra Low Power SOC for Portable Health Monitoring Platforms," *IEEE International Symposium on Integrated Circuits (ISIC)*, December 2011.

[6] K. Lyne, "Cellular Handset Integration -- SIP vs. SOC and Best Design Practices for SIP," *IEEE Custom Integrated Circuits Conference*, September 2005.

[7] V. Sundaram*, et al.,* "Recent Advances in Low CTE and High Density System-on-a-Package (SOP) Substrate with Thin Film Component Integration," *IEEE Electronic Components and Technology Conf*erence*,* 2006.

[8] O. Salmela and P. Ikalainen, "Ceramic Packaging Technologies for Microwave Applications," *IEEE Wireless Communications Conference Proceedings*, August 1997.

[9] GarelickSteelCompany, "Melting Points of Common Metals." http://www.garelicksteel.com/pdfs/Melting_Points_of_Common_Metals.pdf

[10] X. Wang and A. Stelzer, "A 79-GHz LTCC RF-Frontend for Short-Range Applications," *IEEE International Microwave Symposium*, June 2011.

[11] Z. Li-Zheng, *et al.*, "Compact LTCC Module for WLAN RF Front-End," *International Conference on Computational Problem-Solving (ICCP)*, October 2011.

[12] B. Y. Siew, *et al.*, "Gain-Enhanced 60-GHz LTCC Antenna Array With Open Air Cavities," *IEEE Transactions on Antennas and Propagation*, Vol. 59, No. 9, pp. 3470-3473, July 2011.

[13] Plextek RF Integration, "LTCC Technology Overview." http://www.plextekrfi.com/images/pdfs/LTCC_technology_overview.pdf

[14] Rogers Corporation, "Understanding When To Use FR-4 Or High Frequency Laminates," 2011. http://www.rogerscorp.com/documents/2122/acm/articles/Understanding-When-To-Use-FR-4-Or-High-Frequency-Laminates.pdf

[15] Rogers Corporation, “High Frequency Materials Product Selector Guide,” 2015. http://www.rogerscorp.com/documents/776/acm/High-Frequency-Laminates---Product-Selector-Guide-and-Standard-Thicknesses-and-Tolerances.pdf

[16] N. H. Al Mamun and P. Dutta, “Patterning of platinum microelectrodes in polymeric microfluidic chips,” *Journal of Micro/Nanolithography, MEMS, and MOEMS*, Vol. 5, No. 3, July 2006.

[17] ELVEFLOW, “PDMS: A REVIEW.” http://www.elveflow.com/microfluidic-tutorials/microfluidic-reviews-and-tutorials/the-poly-di-methyl-siloxane-pdms-and-microfluidics/

[18] Yijun Zhou, Polymer-Ceramic Composites for Conformal Multilayer Antenna and RF Systems, PhD Dissertation Document, Ohio State University, 2009.

[19] G. J. Hayes, *et al.*, “Flexible Liquid Metal Alloy (EGaIn) Microstrip Patch Antenna,” *IEEE Transactions on Antennas and Propagation*, Vol. 60, No. 5, pp. 2151-2156, April 2012.

[20] PermSelect, “Silicone (PDMS) Chemical Compatibility.” https://permselect.com/files/Silicone_Chemical_Compatibility_Chart.pdf

[21] Rogers Corporation, “ULTRALAM® 3000 Liquid Crystalline Polymer Circuit Material,” Datasheet No. RF1.3000 http://www.rogerscorp.com/documents/730/acm/ULTRALAM-3000-LCP-laminate-data-sheet-ULTRALAM-3850.pdf

[22] C. L. Kameni, *et al.*, “Design of a low loss wideband millimeter-wave balun on a multilayer liquid crystal polymer technology,” *IEEE Radio and Wireless Symposium (RWS),* pp. 175-178, January 2012.

[23] C. H. J. Poh, *et al.*, “Packaging Effects of Multiple X-Band SiGe LNAs Embedded in an Organic LCP Substrate,” *IEEE Transactions on Components, Packaging and Manufacturing Technology*, Vol. 2, No. 8, pp. 1351-1360, August 2012.

[24] A. Miller and J. Hong, “Cascaded Coupled Line Filter With Reconfigurable Bandwidths Using LCP Multilayer Circuit Technology,” *IEEE Transactions on Microwave Theory and Techniques*, Vol. 60, No. 6, pp. 1577-1586, June 2012.

[25] D. J. Chung, *et al.*, “Multilayer Integration of Low-Cost 60-GHz Front-End Transceiver on Organic LCP,” *IEEE Antennas Wireless Propagation Letters*, Vol. 10, pp. 1329-1332, November 2011.

[26] H. J. Lu, *et al.*, “Liquid Crystal Polymer (LCP) for Characterization of Millimer-Wave Transmission Lines and Bandpass Filters,” *ASME International Mechanical Engineering Congress and Exposition,* Paper No. IMECE2009-10573, pp. 153-157, November 2009.

[27] Rogers Corporation, “RO3000 Series Circuit Materials.” http://www.rogerscorp.com/documents/722/acm/RO3000-Laminate-Data-Sheet-RO3003-RO3006-RO3010-RO3035.pdf

[28] S. G. Kandlikar, “Review and Projections of Integrated Cooling Systems for Three-Dimensional Integrated Circuits,” ASME J. Electron. Packag., Vol. 136, No. 2, p. 024001, April 2014.

[29] The Engineering ToolBox, "Convective Heat Transfer." http://www.engineeringtoolbox.com/convective-heat-transfer-d_430.html

[30] R. Li, "Optimization of Thermal Via Design Parameters Based on an Analytical Thermal Resistance Model," *Intersociety Conference on Thermal and Thermomechanical Phenomena in Electronic Systems (ITHERM)*, May 1998.

[31] F. Mirza, *et al.*, "Effect of Through-Silicon-Via Joule Heating on Device Performance for Low-Powered Mobile Applications," *ASME J. Electron. Packag.*, Vol. 136, No. 4, p. 041008, September 2014.

[32] EDN Network, "PCB layout tips for thermal vias," September 2013. http://www.edn.com/electronics-blogs/the-workbench/4421218/PCB-layout-tips-for-thermal-vias

[33] Xu Hu, *et al.*, "Analytical Heat Transfer Model for Thermal Through-Silicon Vias," *Design, Automation & Test in Europe Conference & Exhibition (DATE)*, March 2011.

[34] C. Chung-Han, *et al.*, "On the Futility of Thermal Through-Silicon-Vias," *International Symposium on VLSI Design, Automation, and Test (VLSI-DAT)*, April 2013.

[35] E. Savrun, *et al.*, "High Thermal Conductivity Aluminum Nitride Ceramics for High Power Microwave Windows," *5th IEEE International Vacuum Electronics Conference (IVEC),* pp. 45-46, April 2004.

[36] Z. Su, *et al.*, "Dependence of Thermal Conductivities of the AlN Film in the LED Architecture on Surface Roughness and Lattice Mismatch," *ASME Heat Transfer Summer Conference*," Paper No. HT2013-17116, pp. V001T03A004, July 2013.

[37] G. C. Barisich, *et al.*, "An X-band GaN HEMT Hybrid Power Amplifier with Low-loss Wilkinson Division on AlN Substrate," *IEEE International Conference on Microwaves, Communications, Antennas and Electronics Systems (COMCAS)*, October 2013.

[38] J. H. L. Ling, *et al.*, "A New Accurate Closed-Form Analytical Solution for Junction Temperature of High-Powered Devices," *ASME J. Electron. Packag.*, Vol. 136, No. 1, p. 011007, January 2014.

[39] K. Kota, *et al.*, "Hybrid Liquid Immersion and Synthetic Jet Heat Sink for Cooling 3-D Stacked Electronics," *IEEE Transactions on Components, Packaging and Manufacturing Technology*, Vol. 2, No. 5, May 2012.

[40] M. J. Rizvi, *et al.*, "Modelling of Jet-Impingement Cooling for Power Electronics," *International Conference on Thermal, Mechanical and Multi-Physics simulation and Experiments in Microelectronics and Microsystems*, April 2009.

[41] S.-M. Kim, *et al.*, "Optimization of a Hybrid Double-Side Jet Impingement Cooling System for High-Power Light Emitting Diodes," *ASME J. Electron. Packag.*, Vol. 136, No. 1, p. 011010, February 2014.

[42] T. B. Peters, *et al.*, "Design of an Integrated Loop Heat Pipe Air-Cooled Heat Exchanger for High Performance Electronics," *IEEE Transactions on*

Components, Packaging and Manufacturing Technology, Vol. 2, No. 10, pp. 1637-1648, October 2012.

[43] S. S. Chougule, *et al.*, "Thermal Performance of Nanofluid Charged Heat Pipe With Phase Change Material for Electronics Cooling," *ASME J. Electron. Packag.*, Vol. 137, No. 2, p. 021004, June 2015.

[44] K. Seo Young, *et al.*, "Thermal Management of Liquid-Cooled Cold Plates for Multiple Heat Sources in a Humanoid Robot," *International Microsystems, Packaging, Assembly and Circuits Technology Conference (IMPACT)*, October 2009.

[45] Z. Yue and M. S. Bakir, "Independent interlayer microfluidic cooling for heterogeneous 3D IC applications," *Electronics Letters*, Vol. 49, No. 6, pp. 404-406, March 2013.

[46] Y. Xie, *et al.*, "Thermal Performance of a Water-Cooled Microchannel Heat Sink With Grooves and Obstacles," *ASME J. Electron. Packag.*, Vol. 136, No. 2, p. 021001, April 2014.

[47] QATS, "What is Jet Impingement Cooling and How is it applied for Thermal Management of Electronics." http://www.qats.com/cms/2010/09/13/what-is-jet-impingement-cooling-and-how-is-it-applied-for-thermal-management-of-electronics-part-1-of-2/

[48] ZETA Thermal Management, "Liquid cold plates." http://www.thermazeta.com/en/product_show.asp?id=406

[49] Z. Yue, *et al.*, "3-D Stacked Microfluidic Cooling for High Performance 3D-ICs," *IEEE Electronic Components and Technology Conference*, pp. 1644-1650, May 2012.

[50] Hu Du-wei, *et al.*, *Investigation of Cooling Performance of Micro-Channel Structure Embedded in LTCC for 3D Micro-System, IEEE International Conference on Solid-State and Integrated Circuit Technology (ICSICT)*, October-November 2012.

[51] B.-H. Jo, *et al.*, "Three-Dimensional Micro-Channel Fabrication in Polydimethylsiloxane (PDMS) Elastomer," *Journal of Microelectromechanical Systems*, Vol. 9, No. 1, pp. 76-81, March 2000.

[52] S. Metz, *et al.*, "Polyimide microfluidic devices with integrated nanoporous filtration areas manufactured by micromachining and ion track technology," *Journal of Micromechanics and Microengineering*, Vol. 14, No. 3, pp. 324-331, March 2004.

[53] K. C. Lee, *et al.*, "A Novel Compact Quadruple-Mode Microstrip Bandpass Filter with Low Harmonic Response," *IEEE Asia Pacific Microwave Conference*, December 2009.

[54] S. Choi, *et al.*, "Hairpin Tunable Bandpass Filter with Improved Selectivity and Tunability," *IEEE Asia Pacific Microwave Conference*, December 2007.

[55] A. Miller and J. Hong, "Cascaded Coupled Line Filter With Reconfigurable Bandwidths Using LCP Multilayer Circuit Technology," *IEEE Transactions on Microwave Theory and Techniques*, Vol. 60, No. 6, pp. 1577-1586, June 2012.

[56] M. A. El-Tanani and G. M. Rebeiz, "High-Performance 1.5–2.5-GHz RF-MEMS Tunable Filters for Wireless Applications," *IEEE Transactions on Microwave Theory and Techniques*, Vol. 58, No. 6, pp. 1629-1637, June 2010.

[57] D. Mardivirin, *et al.*, "A 2 Pole 9.6-11.7 GHz Band Stop Filter Using Analog Tuning RF MEMS Varactors," *European Microwave Integrated Circuits Conference*, October 2011.

[58] B. Dong, *et al.*, "An Absorptive Filter Using Microfluidic Switchable Metamaterials," *IEEE International Solid-State Sensors, Actuators and Microsystems Conference (TRANSDUCERS)*, June 2011.

[59] S. Pinon, *et al.*, "Development of a microsystem based on a microfluidic network to tune and reconfigure RF circuits," *Journal of Micromechanics and Microengineering*, Vol. 22, No. 7, July 2012.

[60] K. Motoi, *et al.*, "A 72% PAE, 95-W, Single-Chip GaN FET S-Band Inverse Class-F Power Amplifier With a Harmonic Resonant Circuit," *IEEE International Microwave Symposium Digest*, June 2012.

[61] S. Pavlidis, *et al.*, "A Hybrid GaN/Organic X-Band Transmitter Module," *IEEE Radio Wireless Symposium*, January 2013.

[62] Wu Yu-Chen, *et al.*, "A Wideband 0.7-2.2 GHz Tunable Power Amplifier with over 64% Efficiency Based on High-Q Second Harmonic Loading," *IEEE MTT-S International Microwave Symposium Digest*, June 2013.

[63] F. Ali, *et al.*, "Tunable Multiband Power Amplifier using Thin-Film BST Varactors for 4G Handheld Applications," *IEEE Radio and Wireless Symposium*, January 2010.

[64] L. Larcher, *et al.*, "A MEMS Reconfigurable Quad-Band Class-E Power Amplifier for GSM Standard," *IEEE Micro Electro Mechanical Systems*, January 2009.

[65] J. Chen, *et al.*, "Low-Cost 3-D Integration of RF and Micro-Cooling Systems," *IEEE European Microwave Conference*, October 2008.

[66] MEGlobal, "Ethylene Glycol Product Guide," 2008. http://www.meglobal.biz/media/product_guides/MEGlobal_MEG.pdf

[67] AVX Corporation, "AVX High Power Resistive Products." http://www.mouser.com/ds/2/40/Resistive%20Products%20Catalog-187420.pdf

[68] T. F. Lemczyk, *et al.*, "PCB Trace Thermal Analysis and Effective Conductivity," *IEEE Semiconductor Thermal Measurement and Management Symp. Proc.*, pp. 15-22, February 1991.

[69] J. Albers, "An exact recursion relation solution for the steady-state surface temperature of a general multilayer structure," *IEEE Transactions on Components, Packaging, and Manufacturing Technology, Part A,* Vol. 18, No. 1, pp. 31-38, March 1995.

[70] S. Lee, *et al.,* "Constriction/Spreading Resistance Model for Electronics Packaging," *ASME/JSME Thermal Engineering Conference,* Vol. 4, pp. 199-206, 1995.

[71] P. S. Lee, *et al.*, "Investigation of heat transfer in rectangular microchannels," *ScienceDirect Int. J. Heat Mass Trans.*, Vol. 48, No. 9, pp. 1688-1704, April 2005.

[72] M. Thirumaleshwar, "Forced Convection," in *Fundamentals of Heat & Mass Transfer*. New Delhi, Pearson Education, 2009, ch 9, pp. 446.

[73] R. K. Shah and A. L. London, "Laminar flow forced convection in ducts," *Adv. Heat Transfer: Suppl.*, Vol. 1. Academic Press, 1978.

[74] A. N. Smith and H. Nochetto, "Laminar thermally developing flow in rectangular channels and parallel plates: uniform heat flux," *Springer Heat and Mass Transfer Journal*, Vol. 50, No. 11, pp. 1627-1637, May 2014.

[75] M. Corcione, "Natural convection heat transfer above heated horizontal surfaces," *Int. Conf. Heat and Mass Trans.*, January 2008.

[76] R. S. Prasher, "Surface Chemistry and Characteristics Based Model for the Thermal Contact Resistance of Fluidic Interstitial Thermal Interface Materials," *ASME J. Heat Transfer*, Vol. 123, No. 5, pp. 969-975, February 2001.

[77] I. Savija, *et al.*, "Effective Thermophysical Properties of Thermal Interface Materials: Part I - Definitions and Models," *ASME International Electronic Packaging Technical Conference and Exhibition*, pp. 189-200, July 2003.

[78] S. Khalsa and G. Subbarayan, "Squeeze Flow Models for Thermal Interface Materials Contained Between Parallel Plates and Plates With Posts," *ASME Pacific Rim Technical Conference and Exhibition on Packaging and Integration of Electronic and Photonic Systems*, pp. 263-269, July 2011.

[79] V. W. Antonetti, *et al.*, "An Approximate Thermal Contact Conductance Correlation," *ASME J. Electron. Packag.*, Vol. 115, No. 1, pp. 131-134, March 1993.

[80] R. L. Jackson, *et al.*, "A Closed-Form Multiscale Thermal Contact Resistance Model," *IEEE Trans. Compon., Packag., Manuf. Technol.*, Vol. 2, No. 7, pp. 1158-1171, July 2012.

[81] Texas Instruments, E. Darvin, "Semiconductor and IC Package Thermal Metrics," Application Report No. SPRA953B, 2012. http://www.ti.com/lit/an/spra953b/spra953b.pdf

[82] Freescale Semiconductor, "Thermal Analysis of Semiconductor Systems," White Paper No. BASICTHERMALWP/ REV 0, 2008. http://cache.freescale.com/files/analog/doc/white_paper/BasicThermalWP.pdf

[83] S. Pinon, *et al.*, "Development of a microsystem based on a microfluidic network to tune and reconfigure RF circuits," *Journal of Micromechanics and Microengineering*, Vol. 22, No. 7, June 2012.

[84] W. J. Ellison, "Permittivity of Pure Water, at Standard Atmospheric Pressure, over the Frequency Range 0–25 THz and the Temperature Range 0–100 °C," *Journal of Physical and Chemical Reference Data*, Vol. 36, No. 1, 2007.

[85] J. Hong and M. J. Lancaster, "Lowpass and Bandpass Filters," in *Microstrip Filters For RF/Microwave Applications*. New York, NY: Wiley, 2001, ch. 5, sec. 2.7, pp. 151–158.

[86] E. Hammerstad and O. Jensen, "Accurate Models for Microstrip Computer-Aided Design," *IEEE MTT-S International Microwave Symposium Digest*, pp. 407-409, May 1980.

[87] J. Svacina, "A Simple Quasi-Static Determination of Basic Parameters of Mulitlayer Microstrip and Coplanar Waveguide," *IEEE Microwave and Guided Wave Letters*, Vol. 2, No. 10, pp. 385-387, October 1992.

[88] J. Svacina, "Analysis of Multilayer Microstrip Lines by a Conformal Mapping Method," *IEEE Transactions on Microwave Theory and Techniques*, Vol. 40, No. 4, pp. 769-772, April 1992.

[89] Y. J. Yoon and B. Kim, "A New Formula for Effective Dielectric Constant in Multi-Dielectric Layer Microstrip Structure," *IEEE Conference on Electrical Performance of Electronic Packaging*, pp. 163-167, October 2000.

[90] D. F. Rivera, "Approximate Capacitance Formulas for Electrically Small Tubular Monopole Antennas," NUWC-NPT Technical Report 10817. http://www.ittc.ku.edu/~callen/active_antennas/Rivera1995NUWSDpp73.pdf

[91] M. Kirschning and R.H. Jansen, "Accurate Model for Effective Dielectric Constant of Microstrip and Validity up in Millimeter-Wave Frequencies," *Electronics Letters*, Vol. 18, No. 6, pp. 272-273, March 1982.

[92] E. Yamashita, et al., "Microstrip Dispersion in a Wide Frequency Range," *IEEE Transactions on Microwave Theory and Techniques*, Vol. 29, No. 6, June 1981, pp. 610-611, June 1981.

[93] M. Kobayashi, "A Dispersion Formula Satisfying Recent Requirements in Microstrip CAD," *IEEE Transactions on Microwave Theory and Techniques*, Vol. 36, No. 8, pp. 1246-1250, August 1988.

[94] D. M. Pozar, "Transmission Lines and Waveguides," in *Microwave Engineering*, 3rd Edition, Wiley, 2005, ch. 3, sec. 3.8, pp. 144-145.

VITA

OUTMANE LEMTIRI CHLIEH

Mr. Outmane Lemtiri Chlieh received the Engineering Diploma, equivalent to a Master's degree, in electronics and signal processing with a major in integrated circuit design from INP-ENSEEIHT, Toulouse, France, in November 2011. He received a second Master degree in Micro- and Nano- systems from INP (Institut National Polytechnique de Toulouse) during the same year. He has been a graduate student in the Georgia Institute of Technology, Atlanta, GA, USA, since January 2011 and has started working towards the Ph.D. degree when he first joined the Microwave Circuit Technology research group “MiRCTECH” in June 2011. His doctoral research mainly focused on developing novel cooling and tuning techniques for high power devices on organic substrates. A part of his work consisted of characterizing III/V based-power amplifiers using load pull measurements.

Mr. Outmane Lemtiri Chlieh is the recipient of the IEEE MTT-S Fall 2011 BS-MS Scholarship Award for the 0.18um CMOS UWB balun work. He was a co-author in the paper that received the Best Student Paper Award at the 2014 IEEE Radio Frequency Integrated Circuits Symposium, Tampa, FL, USA. He is also an active member in IEEE-Eta Kappa Nu (IEEE-HKN) Honor Society, Georgia Institute of Technology, Atlanta, GA, USA.